# Material Uncertainty in Composite Structures: A Stochastic Finite Element Framework

## Implementation of realistic random fields and efficient sampling for probabilistic progressive failure of laminates

Aerospace Engineering Msc - ASM track

Manuel Barbosa

Delft University of Technology

TU Delft

# Material Uncertainty in Composite Structures: A Stochastic Finite Element Framework

## Implementation of realistic random fields and efficient sampling for probabilistic progressive failure of laminates

by

Manuel Barbosa

for obtaining the degree of Master of Science in Aerospace Engineering at Delft University of Technology, to be defended publicly on November 22, 2024

| | |
|---|---|
| Student number: | 5043417 |
| Supervisor: | Dr. D. Zarouchas |
| Chair of assessment commitee: | Dr. J.J.E. Teuwen |
| External Examiner: | Dr. B. Chen |
| Project Duration: | March, 2024 - November, 2024 |
| Faculty: | Faculty of Aerospace Engineering, Delft |

Cover: A350 with carbon fiber livery by Xinhua/Zuma Press (Modified)

TU Delft

# Acknowledgments

I would like to recognize the significant contributions of many people to not only this project, that started 9 months ago, but also to my academic journey, that started many years back and is completed as I obtain my Master's in Aerospace Engineering.

To my supervisor Dimitrios, thank you for your support and attention throughout these months, and especially for your openness to discussion and easy-going nature that allowed me to make mistakes, find my own path, and ultimately learn a great deal.

To my family, who have supported me and encouraged me to follow whatever I thought was right, I feel very lucky that I got to live and grow through wonderful experiences because of your investment in my future.

At last, I am deeply thankful for all the friendships I have made in and out of my studies, as those connections are the most important and lasting things I leave with.

To my friends back home, it would not have been possible to achieve anything without your love and support, thank you for always believing in me more than myself. To Zé, especially, I owe all my gratitude, for your intelligence and generosity are unrivaled, and a big part of the reason I made it to the end of my Bachelor's.

Finally, I have somehow found myself having a second family in this corner of the Netherlands, something which still makes me as surprised as grateful. To the whole (study?) group, I thank you for the happiness you have brought me these last two years, and assure you I will keep them in my memory forever. To those who I've been with from the start, especially Anna, João, and Sara, thank you for accompanying me through the frustration and difficulties of academics, which were ultimately enjoyable because I shared them with you. Thank you to all others who, during my thesis, listened to my complaints, problems and existential questions, this report would not exist without you.

*Manuel Barbosa*
*Delft, November 2024*

# Summary

Composite materials are increasingly utilized in industries such as aerospace due to their exceptional specific strength and stiffness. However, accurately predicting the structural behavior of composites remains a challenge partly because of their inherent material variability, often arising from manufacturing imperfections such as fiber misalignment, inhomogeneous curing, and resin distribution. These uncertainties lead to significant deviations between experimental data and numerical models, which are typically addressed by applying conservative safety factors. While effective, this approach often results in overly conservative, weight-inefficient designs.

This thesis presents a novel Stochastic Finite Element Method (SFEM) framework aimed at improving the reliability analysis of composite structures by incorporating material uncertainty into the computational model. The method integrates the Karhunen-Loève (KL) expansion to represent spatial variability in material properties and Latin Hypercube Sampling (LHS) to enhance the efficiency of probabilistic simulations. The proposed framework is implemented in a widely-used commercial finite element software, Abaqus, demonstrating a possible robust and user-friendly application of the stochastic methodology.

In the process of generating random fields for material properties, two methods of applying the Karhunen-Loève expansion are developed and compared: the Galerkin method and the Bounding Box method. Both approaches discretize random fields over a finite element mesh, but they differ in terms of computational efficiency and accuracy. The Galerkin method directly solves eigenvalue problems over the mesh, while the Bounding Box method approximates the domain with simplified boundaries, reducing computational cost. The former, despite being the norm in literature, is more complex and less efficient, and is found to not significantly reduce approximation errors. LHS is found to speed up the convergence of both these methods, when compared to Monte Carlo sampling.

The overall stochastic methodology involves multiple stages: random field generation using the KL expansion, probabilistic sampling of the input variables through LHS, and finite element analysis to simulate progressive failure in composite laminates. A continuum damage model (CDM) is employed through a User Defined Material (UMAT) Abaqus subroutine to capture damage initiation and propagation. The methodology is designed to handle complex geometries and load cases, providing flexibility for real-world applications. Obtaining probabilistic failure curves through statistical post-processing, this framework facilitates reliability analysis with minimal intervention in third part codes.

Three case studies from literature, including open hole tension tests, are used to validate the SFEM framework, comparing its probabilistic predictions of failure loads with experimental data. The methodology shows significant improvements in the accuracy of failure predictions, capturing the inherent variability than traditional deterministic methods ignore. The results also reveal that incorporating realistic spatial variability into finite element models helps provide a more accurate assessment of failure probabilities, when compared with simpler reliability methods. This suggests that, with future improvements and further validation, stochastic methods such as the one presented have the potential of leading to better optimization of composite designs, reducing unnecessary conservatism in structural safety factors while ensuring reliable performance.

By offering a more efficient, robust and accurate method for handling material uncertainty, this research advances the state of the art in composite reliability analysis and supports the ongoing transition toward the use of virtual testing in the design and certification of composite components.

# Contents

# List of Figures

# List of Tables

# Nomenclature

## Abbreviations

| Abbreviation | Definition |
|---|---|
| ANN | Artificial Neural Network |
| CDF | Cumulative Distribution Function |
| CDM | Continuum Damage Model |
| CFRP | Carbon Fiber Reinforced Polymer |
| COV | Coefficient of Variation |
| CZM | Cohesive Zone Model |
| DIC | Digital Image Correlation |
| DL | Delamination |
| DOF | Degree of freedom |
| FE | Finite Element |
| FEA | Finite Element Analysis |
| FEM | Finite Element Method |
| FFC | Compressive Fiber Failure |
| FFT | Tensile Fiber Failure |
| FORM | First Order Reliability Method |
| FPF | First-ply-failure |
| FPI | Fast Probability Integration |
| FRP | Fiber Reinforced Polymer |
| KL | Karhunen-Loève |
| LHS | Latin Hypercube Sampling |
| LPF | Last-ply-failure |
| LSF | Limit State Function |
| MCS | Monte Carlo Sampling |
| MDM | Material Degradation Model |
| MFC | Compressive Matrix Failure |
| MFT | Tensile Matrix Failure |
| PDF | Probability Density Function |
| RF | Random Field |
| RSM | Response Surface Method |
| SFE | Stochastic Finite Element |
| SFEM | Stochastic Finite Element Method |
| SORM | Second Order Reliability Method |
| SSFEM | Spectral Stochastic Finite Element Method |
| UMAT | User Defined Material |
| VCCT | Virtual Crack Closing Technique |
| XFEM | Extended Finite Element method |

## Symbols

| Symbol | Definition | Unit |
|---|---|---|
| $b_{cX}$ | Correlation parameter for x axis | [] |
| $b_{cY}$ | Correlation parameter for y axis | [] |
| $d_r$ | Bounding box size ratio | [] |

| Symbol | Definition | Unit |
|---|---|---|
| $E_1$ | Elastic modulus in fibre direction | [Pa] |
| $E_2$ | Elastic modulus in matrix direction | [Pa] |
| $E_3$ | Elastic modulus in out-of-plane direction | [Pa] |
| $G_{12}$ | Shear modulus in in-plane direction | [Pa] |
| $G_{13}$ | Shear modulus in out-of-plane longitudinal direction | [Pa] |
| $G_{23}$ | Shear modulus in out-of-plane transverse direction | [Pa] |
| $J$ | Jacobian determinant | [] |
| $L$ | Shape function | [] |
| $M$ | Number of KL terms | [] |
| $N_\theta$ | Number of random cases | [] |
| $nnod_{RF}$ | Number of nodes per RF element | [] |
| $R$ | Reliability | [] |
| $w$ | Random Field | [] |
| $\alpha_0$ | Angle of fracture plane for pure compression | [Rad] |
| $\beta$ | Shear non-linearity parameter | $[Pa^-3]$ |
| $\epsilon_{M,\sigma_w^2}$ | Local variance error | [] |
| $\bar{\epsilon}_{M,\sigma_w^2}$ | Global variance error | [] |
| $\epsilon_{\sigma_s}$ | Spatial standard deviation error | [] |
| $\eta$ | Vertical isoparametric coordinate | [] |
| $\lambda$ | Eigenvalue of covariance kernel | [] |
| $\mu$ | Mean | [] |
| $\nu_{21}$ | Poisson's ratio in in-plane direction | [] |
| $\nu_{23}$ | Poisson's ratio out-of-plane longitudinal direction | [] |
| $\nu_{13}$ | Poisson's ratio out-of-plane transverse direction | [] |
| $\xi$ | Random Variable of KL expansion | [] |
| $\xi$ | Horizontal isoparametric coordinate | [] |
| $\sigma_n$ | Normal stress on fracture plane | [Pa] |
| $\sigma_w$ | Point-wise standard deviation | [] |
| $\sigma_w$ | Spatial standard deviation | [] |
| $\tau_{12}$ | In-plane shear stress | [Pa] |
| $\tau_{13}$ | In-plane-through-thickness shears tress | [Pa] |
| $\tau_{23}$ | Transverse shear stress | [Pa] |
| $\tau_L$ | Longitudinal shear stress on fracture plane | [Pa] |
| $\tau_T$ | Transverse shear stress on fracture plane | [Pa] |
| $\phi$ | Eigenfunction of covariance kernel | [] |

# 1

# Introduction

In the past few decades, the use of composite materials in the aerospace industry has grown significantly. This can be seen in figure 1.1, where the A350 aircraft has far and ahead the highest percentage of composite structural weight - the value for the A350XWB is around 50% [1]. Growing sustainability concerns, which imply a need for lighter and damage tolerant structures, and an always-present necessity to reduce costs by optimizing aircraft structures, suggest this growth will continue.

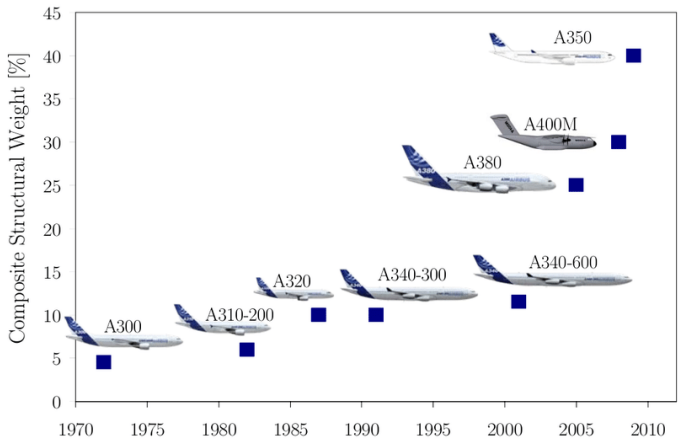


**Figure 1.1:** Evolution of use of composite materials in Airbus aircraft [2].

Composite materials result from combining two or more materials to obtain better properties than their monolithic versions. Usually, a matrix serves as support to a reinforcement material, a fiber or particulate, which provides the strength and stiffness [3]. The most common versions are CFRPs (Carbon Fiber Reinforced Polymers) and GFRPs (Glass Fiber Reinforced Polymers), which are composed of a polymer resin matrix, either thermoset or thermoplastic, and carbon/glass fiber reinforcement. They are very popular for high-performance applications partly because of their high strength to density and stiffness to density ratios, a consequence of the load being transferred from the light matrix to the strong/stiff reinforcement. The material can also be tailored, by changing the fiber orientations to achieve the required properties on the expected load path, so that the weight is optimized.

The analysis of composite structures presents new challenges when compared to the isotropic case, an inherent consequence of having direction-dependent material properties (anisotropy). That is especially true when it comes to predicting their failure, which is ruled by gradual, complex and interacting mechanisms related to the fibers, matrix, and the different lamina that form a composite laminate. Additionally, the variability in the properties of manufactured parts causes an unpredictable scatter in the structural response, and a significant deviation between current numerical analysis methods and exper-

imental measurements. The complex nature of composites and their manufacturing methods make this randomness inherent and unavoidable, whether its related to the precise geometry, fiber orientation, inhomogeneous curing, distribution of the resin, fiber volume ratio, or other sources. It is, however, essential to improve current numerical methods for composite structural analysis: the growing demand for these materials requires that the gap between experiments and computational modelling be bridged, so that virtual testing can reliably replace part of the large amount of costly and time-consuming test campaigns that are required in the design phase.

Currently, material uncertainty is addressed by applying safety factors to the expected loads and material properties, which leads to overly conservative designs. Another option is to take the Finite Element Method (FEM), by far the most popular tool for deterministic analysis, and include uncertainty in the model, making probabilistic predictions in a stochastic approach which is referred to as the Stochastic Finite Element Method (SFEM). This method can then be used for composite reliability analysis, predicting failure probabilities instead of a single failure load. Such a methodology may be used so that a design achieves a target reliability, without exceeding it, which is often the case with safety factors. Additionally, incorporating uncertainty in numerical analysis leads to a better understanding and more realistic representation of the experimental response of a structure.

The present study aims to develop a SFEM framework for reliability analysis of composite structures. This framework should improve current solutions, and be applicable to laminates with complex geometries or load cases. Since Open Hole Tension (OHT) testing is required for the qualification of composite parts that will be joined to other aircraft parts [4], this is chosen as the test case that will be used to validate the proposed methodology.

The literature review of section 2 revealed that few SFEM implementations for composite reliability including progressive failure analysis exist. Furthermore, spatial variation of material properties has not been considered except in an uncorrelated, random way, with inefficient sampling. Therefore, it was decided that the proposed framework should combine a Random Field (RF) discretization method (Karhunen-Loève, or KL, expansion) and an improved sampling method (Latin Hypercube Sampling, or LHS) with generic, commercial FEM software (Abaqus). At the end of the section, the research questions and objective are defined.

In section 3, two methods of applying the Karhunen-Loève expansion, to generate random distributions of properties in a given finite element mesh, are detailed. Those methods are then compared and conclusions are made about their advantages and disadvantages for the current application and test cases.

In section 4, the stochastic methodology is defined. First, the FEM is described, and then an overview of the various steps and inputs is given. Finally, the limitations of the method are discussed.

In section 5, the proposed methodology is validated with three test cases from literature, two of them being OHT. The results for each test case are presented and discussed.

Section 6 summarizes the findings of the study, and conclusions are made regarding the research questions. Finally, recommendations for future research on the topic are given.

# 2

# Literature Review

This research aims to develop a general-purpose SFEM capable of assessing the reliability of composite structures. The following sections review published literature on these topics: section 2.1 succinctly describes the methods that are most commonly used for progressive failure analysis of composite structures, and section 2.2 addresses the state-of-the-art of reliability methods and the Stochastic Finite Element Method, which will be the focus of the research.

The developed method will, in section 5, be used to predict the probabilistic response of open-hole laminates, and these predictions will be compared with experimental results, for validation purposes. Therefore, the reviewed literature will often be related to the research objective and this test case. Finally, in section 2.3, conclusions will be made about the applicability of the reviewed ideas and methods to the goal of the present study, as a gap in literature is found. The research questions and objective are then defined.

## 2.1. Progressive failure analysis of composites

Composite laminates are becoming increasingly popular in industries where high-performance, lightweight materials are sought out for, such as aerospace and automotive. These anisotropic materials add complexity to structural design, but are used for their damage tolerance and high stiffness and strength to weight ratios [5].

Several interacting damage mechanisms have been observed in FRPs, which can occur in different scales and sections of the structure. It is frequently considered in analysis that the specimen fails when all its plies have failed, with several options existing for the failure prediction of a ply. Understanding how to model the initiation and propagation of the different types of damage, resulting in ultimate failure, is what progressive failure analysis entails. As will be detailed in section 2.2, composite laminate analysis and predictions consistently deviate from experimental results, which is due to both the inherent randomness in the properties and the complexity of the analysis process. The latter is consistently being addressed in literature, as new challenges and strategies arise with the growth in popularity of the materials.

This section describes current widespread methods used in progressive failure analysis of composite laminates, reviewing established theory and literature on the topic. As this research project is focused on the implementation of state-of-the-art reliability and uncertainty analysis, this part of the review will not be too extensive, since it is intended that the model that will be developed will use well-known and proven methods. Section 2.1.1 will focus on the failure modes and distinguishing stress-strain based analysis (Continuum Damage Models) from fracture mechanics. Section 2.1.2 details how each of the failure modes can be addressed in a Finite Element Model using strategies based on both CDMs and fracture mechanics.

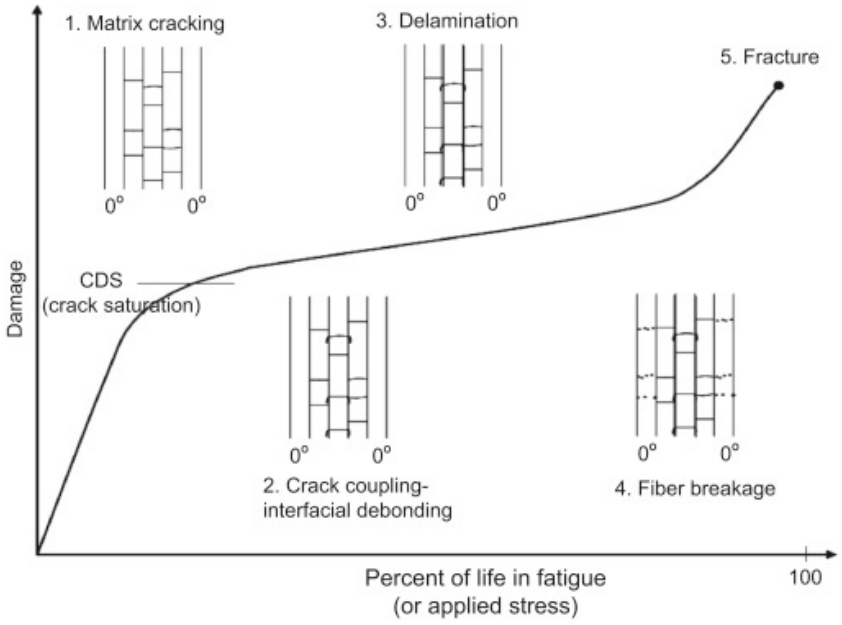


**Figure 2.1:** Evolution of failure in laminates subjected to static or fatigue loading [7].

### 2.1.1. Damage modes and mechanics

Damage or failure modes can generally be divided into the intralaminar and interlaminar types. The first type is observed in individual layers of the laminate, while interlaminar failure, or delaminations, result from the interaction between two lamina, and are observed in the contact area.

The onset of damage in laminates precedes its ultimate failure, and damage is progressively accumulated between the onset load and the failure load. The first damage mode that is normally observed is matrix cracking [6]. Cracks can then accumulate and propagate to the direction of other plies, resulting in separation of two plies, or delaminations. The fiber-matrix interphase may then fail with enough load (debonding) and finally fibre failure will occur. A schematic representation of this progression is shown in figure 2.1.

The most common approach is to simplify these microscopic mechanisms into meso-scale failure modes, where different tests of a single lamina are used to obtain characteristic strength values for each intralaminar mode. This ignores the different processes (such as cracking, debonding) that are microscopically occurring. The following modes are usually defined:

- **Tensile Fiber Failure (FFT)**: tension along the fibre direction, with the fibres, which are the main and intended load-carrying component of the structure, not being able to take more load and, with a transverse fracture, failing catastrophically. Since the fibre reinforcement direction is the strongest one of the material, this is the desired failure mode of composite laminates. Strength symbol is $X_T$.
- **Compressive Fiber Failure (FFC)**: compression along the fibre direction, resulting in fibre collapse from shear kinking and surrounding matrix failure, where a local buckled band forms and a fracture grows at its boundaries. [8]. Strength symbol is $X_C$.
- **Tensile Matrix Failure (MFT)**: tension transverse to fiber direction, with failure governed by matrix cracking along the fibers. Since the matrix is not the main load-carrying component, this mode leads to reduced stiffness losses, but accumulation and propagation of cracks can lead to other failure modes. Strength symbol is $Y_T$.
- **Compressive Matrix Failure (MFC)**: compression transverse to fiber direction, related to shear failure of the matrix, with the cracks growing at a fracture angle [9]. Strength symbol is $Y_C$.
- Pure shear failure: pure shear failure of a ply, with fracture surface along the fiber direction. Strength symbol is $S$.

- Delamination (DL): separation of adjacent plies due to out-of-plane shear or tensile stresses at the interface, commonly originating from saturation of matrix cracks or ply stiffness mismatching [8].

Different strategies exist to predict failure based on different known modes. The **Continuum Damage Model** approach is the most common one in literature and industry, and is based on the stress-strain relationship, which conveniently also governs FEA. This approach relies on failure criteria, which are expressions that are calculated with the stresses on the specimen and the strengths for each failure mode: if the expression leads to a value of 0 or less, damage is initiated. For this reason they are also referred to as damage initiation criteria. When damage is predicted, its propagation must also be modeled, to further increase the load until ultimate failure.

**Damage Initiation**

From the Von-Mises criterion for isotropic materials, criteria for composites have evolved into having a stronger physical basis. Failure criteria can mode-dependent or independent. The former predicts the type of failure that occurs where as the latter ignores the progressive damage accumulation and simply predicts failure of the ply.

The simplest form of criteria are the max-stress and max-strain criteria. These are interchangeable only in the case of on-axis tension/compression, while for other load cases non-linear effects mean that there isn't a direct proportionality term (on-axis young's modulus divided by Poisson's ratio) to calculate stress from strain [6]. In any case, both criteria simply compare the strength of each failure mode with the acting stress/strain, and predict failure in case the latter is higher. Obviously, this ignores interactions between failure modes, and is therefore over-simplistic.

Tsai and Hill first developed a criterion that addressed the anisotropic nature of composites, extending the isotropic Von-Mises criterion. Tsai-Hill has only one expression for failure, so it is mode-independent. It was improved by the Tsai-Wu criterion, which resulted from curve-fitting Tsai-Hill and accounting for different strengths in compression and tension. Although lacking physical basis, Tsai-Hill can show adequate agreement with experimental results, and is still widely used in industry [8].

Hashin (and Hashin-Rotem) criteria were the first to differentiate between matrix and fiber failure, with separate expressions and some physical basis. However, Puck was the first to be sucessful at developing a criterion based on the real mechanics at play in composite failure. Its formulation is not based on yielding laws of ductile materials, but on brittle fractures, which is what actually governs failure in composite laminates [6]. The assumption was made that failure at the critical failure plane is affected only by stresses acting on that plane. Six acting stresses and failure strengths, which result from those defined for each failure mode (plus the shear strength in the 23 plane, with fibres aligned with 1), are included in 4 expressions. Out of these, two correspond to matrix compression failure, one to matrix tension failure and the last to fibre tension/compression failure. Puck shows good agreement with experimental results, including for combined load cases, but requires determining failure surface inclination parameters. Other criteria of note in literature are Cuntze, which is based on curve-fitting (less physical meaning) and LaRC03-5, which are a set of physics-based criteria, following up on Puck's work.

Failure criteria used in continuum mechanics models are chosen based on known accuracy for given failure mode and computational cost. Simpler criteria like Tsai-Wu and Hashin-Rotem are very often used in cases of acceptable agreement for their simpler formulations. Three editions of the Worldwide Failure Exercise (WWFE) have offered some comparative data for the accuracy and quality of each criteria, with Puck and LaRC05 being recommended [10]. Note that criteria that addresses delaminations are scarce, since this failure mode is usually not modelled with the continuum damage strategy.

**Damage Propagation**

Damage propagation in CDMs is controlled by Material Degradation Models (MDMs). These models relate the damage mode to a given decrease of the material stiffness properties. The way the properties are decreased where damage was predicted is what differentiates each MDM. The models can use either sudden or gradual degradation.

Most commonly, sudden degradation models reduce all the material properties of a lamina to 0 when

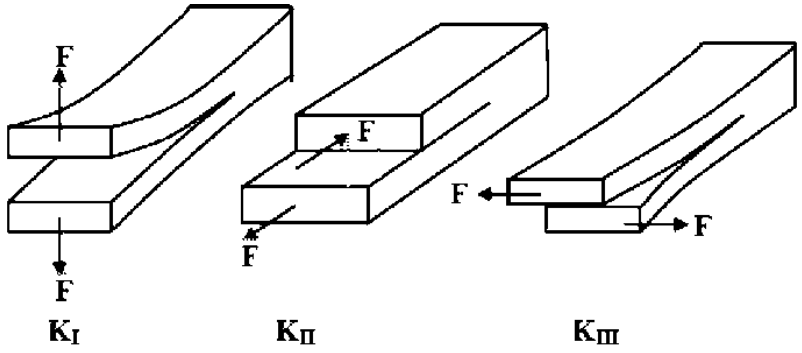


**Figure 2.2:** Fracture modes [16].

fibre failure occurs, which was the approach taken by Lee [11]. This is because, as previously discussed, the fibres are the main load-carrying components, with their failure being catastrophic. Other authors have taken more realistic approaches, although always based on experimental campaigns and not theory. Most notably, McCarthy et al. [12] applied a reduction of 10% to select material properties depending on the nature of the loading (compression/tension), and in [13] Camanho and Matthews used different factors for the longitudinal stiffness, while other properties remained intact.

Regarding matrix failure, most sudden degradation models, including Lee, degrade the transverse stiffness to 0, as well as the shear moduli $G_{12}$ and $G_{13}$. Additionally, it can be considered that some properties to which the fibres contribute may or may not be degraded (Mccarthy et al. degrade also $E_3$), and the differentiation between compressive and tensile failure is done by Camanho and Matthews.

Gradual degradation models are also commonly found in literature, most notably the one suggested by Puck and bilinear sofetning [9]. The former uses a degradation factor that must be calculated for every stress increment or obtained experimentally. Bilinear softening requires determining the fracture toughness for each damage mode, as well as other parameters, so as to calculate the slope of the degradation, for each increment giving a damage parameter that is included in the stiffness matrix.

This type of MDM can be said to be more realistic, since sudden degradation models consider only the material as undamaged or fully damaged, with no states in-between, which can be overly conservative [14]. It does however entail higher computational costs. Furthermore, it can be said that it still partly suffers from the same problem as a lot of criteria/models used in CDMs, which is lack of a physical basis. In general, delaminations are not modelled with the continuum damage strategy, so MDMs that include it are rare.

Other approaches to modelling damage in composite laminates are based in **fracture mechanics**. This methodology is energy-based and was first developed for isotropic materials by Griffith [15], forming linear elastic fracture mechanics, with a plastic zone at the tip being introduced later by Irwin [8]. Three modes of fracture are defined, as shown in figure 2.2: mode I for opening due to tensile stresses, mode II for sliding due to in-plane shear, and mode III tearing due to out-of-plane shear. For each mode, a strain energy release rate (SERR) $G$ (rate of energy transformation during crack propagation) can be defined, as well as a stress intensity factor $K$. The stress intensity factors represent the stress state near the crack tip, where there is a singularity (infinite stress).

Critical SERRs can be obtained experimentally. Then they are compared with the current SERR, obtained through different methods from the stress fields or displacements, and it is considered that crack propagation occurs depending on the values of failure criteria expressions. For load cases corresponding to a single mode, the criteria is simply that $G_i$ be higher than the critical $G_{ic}$ of that mode. For most situations, criteria including all the modes is used, such as the BK [17] and power-law [18] criteria.

Applying fracture mechanics to composite analysis, especially when it comes to modelling DLs, offers additional challenges, but can have the benefit of better representing the real local processes than CDMs. This is because the latter does not consider the specifics of crack growth in anisotropic materials (along the fibers) and MDMs are often heuristic and lack physical basis [8]. Specifically, discretely

modelling cracks can involve complications such as a priori knowledge of crack paths, since fracture mechanics requires pre-existing discontinuities, mesh geometry re-defining, and additional criteria/-models either for this ”crack enriching” or for behaviour between two lamina [19] [20]. Smeared crack models offer an alternative to discrete models, the stiffness being degraded according to the cohesive law of a crack smeared throughout the ply of an element of the mesh. These models, however, show significant mesh dependence [9]. Section 2.1.2 will address in a practical way how these complications are commonly tackled in FEA to model all failure modes, including strategies available in commercial packages, and models found in literature which combine CDMs with those strategies.

### 2.1.2. Finite Element Modelling

Most composite parts cannot be analyzed by simply applying Classical Laminate Theory (CLT) through analytical expressions. This is evidently the case of this research, where specimen with arbitrary geometries will be modelled. FEA is by far the most popular tool for structural analysis, and is based on the relationship

$$F = Ku \tag{2.1}$$

in the linear static case, with K being the stiffness matrix and F and u being the load and displacement vectors, respectively. For each element of the mesh, a constitutive equation is written, with the nodal degrees of freedom (DOFs) displacements/loads as variables, and then built into the global matrices and equation. Depending on the type of elements and assumptions used, the constitutive model will change. The most general lamina constitutive model is the three-dimensional one for an orthotropic material, where its properties are defined in three directions and there are 6 DOFs. Often, this model is simplified to a 2D one, with 3 DOFs. Both models are detailed in appendix A, and that formulation will be used throughout this report.

The most commonly applied plate laminate theories are the aforementioned CLT (very thin plates) and the first-order shear deformation theory. While both use 2D constitutive formulations, the latter adds an additional linear shear deformation term [21]. In commercial FEA software, specifically Abaqus, formulations and nomenclature may slightly differ from literature, but an important distinction is that of shell elements, which are 2D elements with 5/6 DOFs per node, and brick elements, which are 3D elements, with 3 degrees of freedom per node. Shell elements are usually used for plates, where two of the dimensions are much larger than the other. It is also relevant that, typically, when calculating the stiffness matrix, the Gauss-Legendre rule is used for the integral, where the values of any variables being integrated must be known at the gaussian points. These are points defined geometrically in the isoparametric representation of each element, and their number and weight parameter changes based on the type of interpolation and number of nodes of the chosen element type.

A review is now presented of different methods found in current literature to model the damage modes in composite laminates with FEA. There is a focus on open-hole plate models developed in Abaqus, since that is of special interest for this thesis (will be the case study used for validation).

- **Fiber Failure**: These failure modes are almost exclusively modelled with the CDM approach. Currently, common criteria for damage initiation are Hashin [22] [23], Puck [5] and LaRC05 [8], along with the maximum stress criterion [24]. Regarding MDMs, gradual degradation models are now quite common, like Puck and exponential evolution laws [23], while sudden degradation remains popular due to its simplicity [22] [25]. The latter’s factors change a lot depending on the chosen reference. Finally, in [26], a Critical Failure Volume method is used to predict fibre failure, an averaging strategy which already encompasses stochastic effects and is used to predict failure probabilities [27].
- **Matrix failure**: most authors have either taken the CDM approach [22], with similar criteria to those of fibre failure, or the fracture mechanics approach through the Extended Finite Element Method (XFEM) [8] [23].

  This method is based on locally enriching elements so that a crack can propagate through them, with additional functions used for the discontinuity. It avoids re-meshing and pre-defining a crack path, with the crack being able to propagate in multiple directions. In Abaqus, an initial crack can

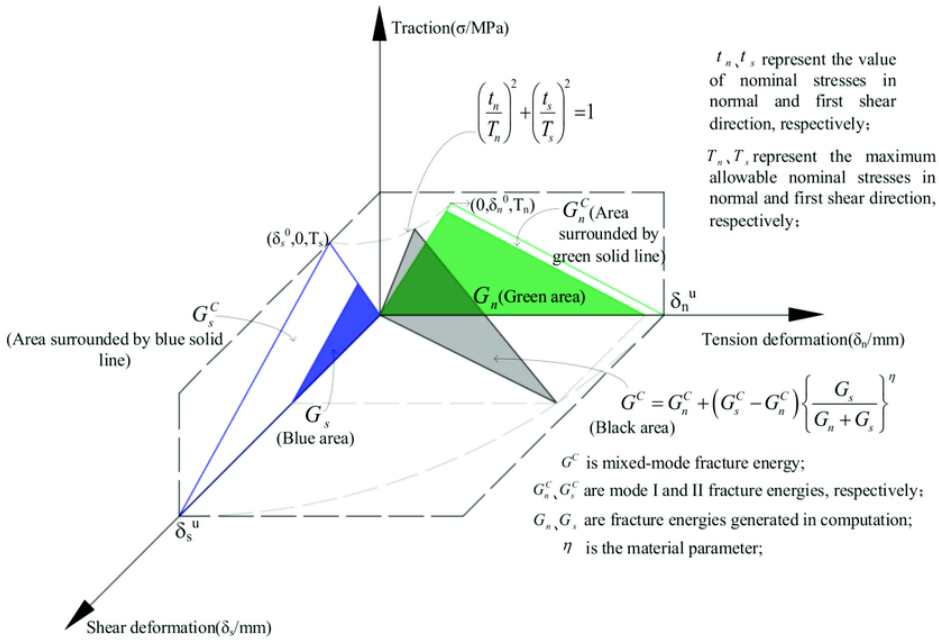


**Figure 2.3:** Bi-linear traction separation law for Modes I and II, with quadratic nominal stress and BK criteria [29].

be specified, or crack initiation criteria defined, with choices from maximum stress to the quadratic nominal stress criterion, the latter relating different modes [28] and being widely used in literature [20]. After initiation, criteria such as BK is used to predict final mixed-mode fracture. Figure 2.3 shows a typical bilinear traction-separation law for an element, with the separate laws for modes I and II and mixed-mode [29]. Note that in these laws, the total work per unit area at full damage is always equal to the corresponding fracture toughness $G_c$ [20], and the current SERR can be calculated from the traction-separation law as shown in the figure.

Some authors have blended the CDM and fracture mechanics approaches by enriching elements only when stress-strain criteria is met. Multiple criteria have been used, such as Puck's Matrix failure criteria [8] or Hashin [23]. The latter example utilized the Phantom Node modification of the method, in which the crack splits damaged elements into two elements with separate displacement fields. After the CDM predicts damage onset, the softening part of the traction-separation law, with propagation criteria such as BK, governs the behaviour of the element, instead of the MDMs.

- **Delaminations**: the two most common ways of modelling DLs in FEM are cohesive elements [8] [22] [23] [26] and the virtual crack closing technique (VCCT) [30], both fracture mechanics based. Some authors have taken the simplistic approach of adding a very thin interlaminar isotropic layer of matrix material [25] [24].

  Cohesive elements are used in Cohesive Zone Models (CZMs). These models differ from XFEM in the sense that crack paths have to be defined in pre-processing, and the elements inserted into this path. This is the reason they are used to model inter-facial DLs, where potential crack paths are known. The elements form a cohesive zone between two lamina, with 0 or very small thickness. Cohesive elements are, similarly to XFEM, governed by a constitutive traction-separation law, often with the same initiation and damage evolution laws. Several parameters have to be defined to properly define the constitutive relation, which can go from more well-known and experimentally obtainable, such as the fracture toughness for each mode, to artificial or heuristic ones such as viscosity and penalty stiffness [31]. Furthermore, CZMs often lead to convergence issues and require more computational power due to the additional elements and fine mesh required. They are, nevertheless, the most popular way to model DLs and have shown good correspondence to experiments [32].

  The VCCT technique was first proposed by Rybicki and Kanninen [33],. They developed a tech-

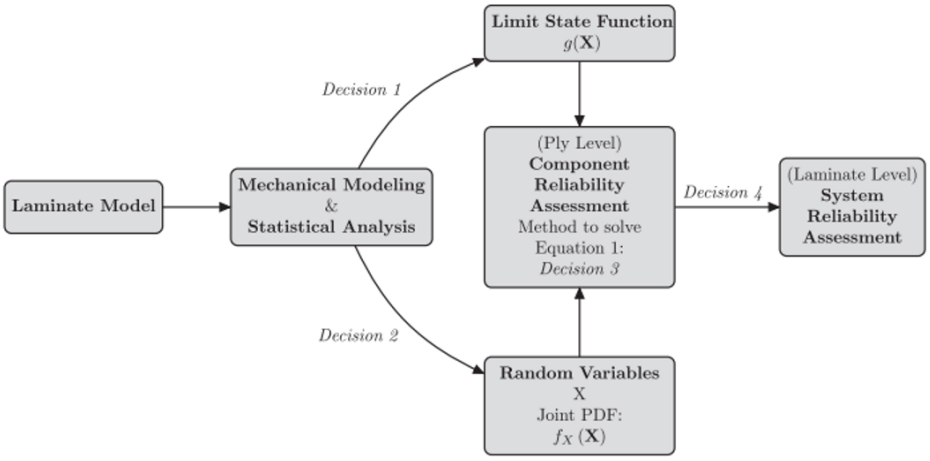


**Figure 2.4:** Flow chart of different steps of reliability analysis of composite structures[38].

nique of calculating the stress intensity factors in the context of FEA, assuming that the energy required to close a crack will be the same as the one needed to create it [34]. For composite analysis, the VCCT technique is used to obtain the SERR, based on the well established Paris relation [35]. Doubled interlaminar nodes are initially bonded (same coordinates) [36] and open, or are released, when the crack propagates along the interface plane, which it is usually constrained to [37]. The VVCT is also quite popular, and has less parameters to be defined than CZM, but is usually used to model brittle crack propagation when there is an initial flaw [30]. Additionally, VCCT models can experience oscillatory behaviour and numerical instability [8].

## 2.2. Composite reliability analysis and the Stochastic Finite Element Method

The present study mainly aims to improve the incorporation of uncertainty in existing models for structural analysis of composites. It is therefore necessary to introduce and contextualize the idea of reliability and uncertainty analysis, especially with respect to composite structures.

The different steps, or choices, involved in stochastic modelling, are represented in figure 2.4, as defined in [38]. Four main decisions are highlighted. In numerical order, they are: which limit state function to use (mostly related to section 2.1, when choosing which failure criteria to use), what random variables are defined and how is this uncertainty modelled, which method to use to assess the reliability on ply level, and how to relate it to laminate level reliability.

This section will first justify the necessity of stochastic analysis in composite structural response predictions, and then focus on decisions 2 and 3, presenting different ways to model uncertainties and reliability methods found in literature. Finally, a more detailed explanation of random field discretization methods, especially of the Karhunen-Loève method, is given.

### 2.2.1. The need for reliability analysis of composites

Deterministic predictions of the structural behaviour of structures are far and ahead the most common type of analysis found in industry and literature. Based on expected average material properties and loads, unique values of quantities like stresses, displacements and failure loads are predicted. The most robust and well-established method of obtaining these values is of course the Finite Element Method (FEM), which spatially discretizes complex geometries into a mesh of simpler elements, the behaviour of which can be described by known sets of equations [39].

The deterministic quality of these predictions is very limiting, since experimental results will always differ

from them, no matter how well the structure and load case are modelled. The main reason for this is the uncertainty in the model, which can come from many sources (further detailed in section 2.2.2). To account for the scatter in responses, the usual practice is to apply safety factors to the expected loads and allowable values to the material strengths. For experimental certification, structures must be predicted to be structurally reliable up to loads significantly higher than those expected in practice [39]. Safety factors are defined based on an intended reliability, defined as the likelihood of a structure surviving a given load case.

Probabilistic (or stochastic) predictions offer an alternative to the deterministic approach. Instead of a single value as output, or failure being a binary variable, the uncertainties are incorporated into the model, and predictions are made in terms of probabilistic distributions or single values of reliability, calculated from a probability of failure.

The main disadvantage of stochastic analysis is the added complexity of incorporating uncertainties and calculating their propagation to the response. However, in recent years, computational advancements have lead to a growing interest in this type of more demanding models, since the required computational power may now be achievable [5] [40]. The question remains though of why we should apply probabilistic methods, specifically to composite structural analysis.

First, composites are inherently stochastic. The experimental response of this type of structures always shows significant scatter and deviation from numerical analysis [5] [38]. The complexity of the material and of the manufacturing processes makes it so that, even with the most rigorous checks, the material properties and geometry will differ both from specimen to specimen and throughout a given specimen, corresponding to random imperfections and defects from manufacturing [41]. For example, Liu and Zheng [42] studied the effect of the uncertainty of layer thickness and radius of polar axis in the burst pressure of aluminium-carbon fiber/epoxy composite vessels, assuming uniform and gaussian distributions for each of those random variables, the variability of which is a consequence of the filament winding process. It is then clear that modelling this inherent stochasticity is the only realistic way to analyse composites, for which the average values are hardly representative of the structure.

Secondly, safety factors are more often than not overly conservative, and lead to over-designed structures [5] [38] [42]. Probabilistic design methodologies, though currently limited by certification requirements, have the potential of further optimizing designs and reducing weights, which is fundamental in the aerospace industry. In this design approach, a reliability requirement is set, and the uncertainty is incorporated into the model so that this value is calculated and achieved, whereas deterministic design usually results in structures that are far more reliable than intended. Similarly, reliability analysis may also be used to calibrate the safety factors themselves.

Finally, reliability analysis is in general a more complete and accurate representation of structural responses. The propagation of, for example, significant uncertainty in the material properties of a structure, may lead to unexpected results and possibly catastrophic failures if ignored. Lekou and Philippidis [43] studied the stochastic behaviour of a Glass/Polyester composite, predicting failure with variability in strength, stiffness and thermal expansion coefficients. They found that, for a given reliability level, safety factors significantly overestimated the failure loads of the structure, when compared to three different reliability estimation methods. This does not contradict the idea that safety factors generally lead to overly conservative designs: it serves instead as an example of how ignoring uncertainties is not an efficient or accurate method of modelling composites. Furthermore, reliability-based designs or safety factor calculation are also common strategies that require probabilistic analysis.

### 2.2.2. Uncertainty Modelling

The issue of modelling the uncertainties in composite structures resides in two different parts: what uncertainties are affecting the response, and what probabilistic distributions can represent this variability.

**Types and origins of uncertainties**

Two types of uncertainty can be distinguished [9]. There is always epistemic uncertainty, which comes from the model itself, since it is never 100% trustworthy. This is because the settings and parameters are not ideal and data is imperfect and finite - in other words, it is caused by our knowledge of a given domain being limited. This uncertainty is systematic, and its estimation depends on the origin. In [44],

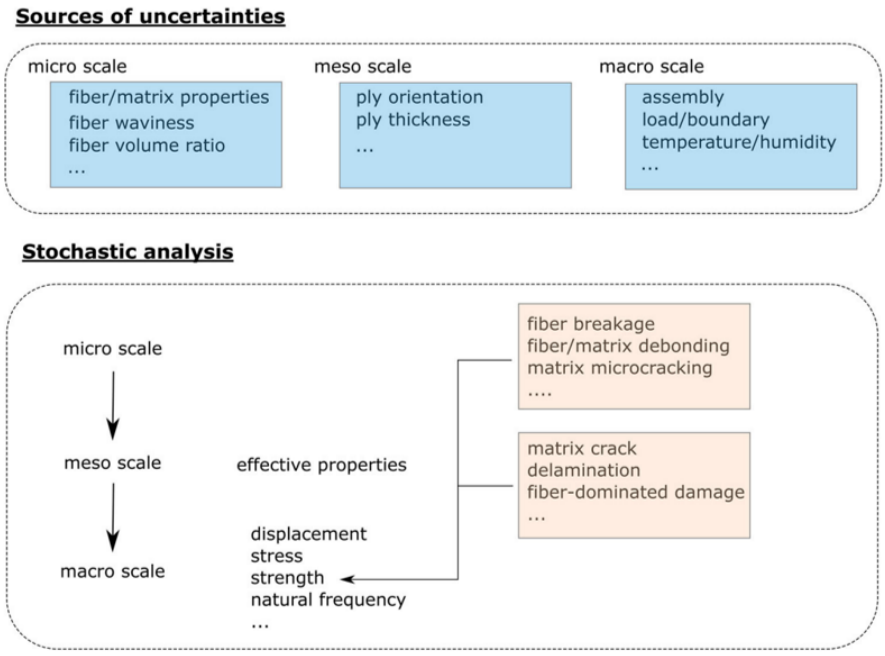


**Figure 2.5:** Scales at which uncertainties can be considered and relation to stochastic analysis [46].

epistemic uncertainty originating from the difference between the training and testing sets of a Neural Network was included in the predictions, since the ANN was trained with FEA results and tested with experimental ones. Another common case of epistemic uncertainty being considered is for information that is extrapolated from a dataset, e.g. assuming a probabilistic distribution, the strength of a part is defined as the average of the experimental measurements, with a given percentage of uncertainty, where the higher the number of measurements the smaller the uncertainty.

There is also the aleatory uncertainty, which comes from inherent stochasticity, rather than systematic error. This is the uncertainty that is found to be much higher in composites than in other structures, and will be the focus of this thesis. Aleatory uncertainty includes any events that we can only consider as decided by randomness, such as a coin-flip, sorting of a deck of cards, etc.

Specifically for composite structures, randomness originates from the manufacturing methods, and their complex constituent processes [45]. However, we can consider the uncertainty at different scales. The smaller the scale, the harder it is to model and propagate uncertainties, but depending on the objective of the research this may be necessary. Figure 2.5 [46] summarizes the different scales at which composite uncertainties can be studied, in terms of sources and analysis variables.

The micro-scale refers to the fiber/matrix level, meso-scale to ply level, and macro-scale to coupon/specimen level. In [45], similar uncertainty origin types to 2.5 are considered, with some detailed additions being voids and porosity of the matrix and appropriate curing. It is also mentioned that processes like ”thermal treatment, filament winding, [and] braiding” are directly connected to variations in fibre curvature and orientation. All these sources, related to the micro and meso scales, have an impact on the material properties such as strength and stiffness. It should also be mentioned that there is an evident spatial variation aspect to most of these uncertainties, which implies variability of material properties throughout one specimen.

Then different joining and cutting techniques (assembly in figure 2.5), and their interactions with the laminates, confer macro-scale geometrical variability, while imperfections in boundary conditions and loads can propagate to generate significant uncertainty in the results.

Micro-scale analysis is the least common in literature, which speaks to its higher complexity. Work on this scale usually has the objective of quantifying the macro-scale material properties from uncertainties in micro-mechanical models. In [47], Stochastic Finite Element Method (SFEM) with Monte Carlo (MC)

is applied to determine the mechanical properties of polymer nanocomposites, which are reinforced with single-walled carbon nanotubes. The young's modulus and poisson's ratio are calculated for each finite element within a multiscale homogenization approach which considered a non-uniform distribution of the nanotubes. There is abundant literature on applying stochastic homogenization techniques through constitutive modelling to derive macro-properties. Examples range from other composite applications, such as determining elastic constants of non-crimp fabric composites [48] and the effect of non-periodic micro-variations in honeycomb structures in global properties (and response) [49], to using the perturbation method to study the impact of microscopical geometrical variation of pores in periodic porous materials[50] [51].

Macro-scale analysis has the objective of calculating the probabilistic response in quantities of interest such as stresses, strains and failure loads. It usually involves attributing probabilistic distributions to random variables or fields (in case spatial variation is considered), like the coupon stiffness, and assessing the response to that variation. In SFEM literature, this is the most common type of stochastic analysis [52] [53], and many more examples are given in section 2.2.3. Some authors have considered randomness in each ply of a laminate, which could be considered a meso-scale approach [5].

Multi-scale approaches are also found in literature, which attempt to combine both aforementioned types of analysis. Recently, in [46], uncertainties at micro-scale (fibre alignment and fiber/matrix parameters) are propagated to macro-scale to derive probability distributions of effective properties of composite laminates, and then probabilistic failure analysis of the specimen is done from these distributions. More direct approaches, where from parameters the response distributions are calculated, are developed in [54], for open-hole composite plates, and [55], for foam-filled honeycomb structures.

For the purpose of stochastic progressive failure analysis of complex FRP specimen, macro-scale analysis is the focus of this thesis, since developing a micro-mechanics model for a multi-scale approach would be out of the scope of the project. Nevertheless, variations from ply to ply in one specimen are a common consideration in literature that, as found in [5], matches experimental results well and improves the reliability of the model.

**Random distributions**

In macro-scale stochastic analysis, random variables are associated with probability distributions, which can be informed from experimental results or assumed.

Evidently, assumed distributions are less faithful to reality, and therefore may affect the accuracy of the results. However, this is often done for convenience. The most common assumption is that random variables have Gaussian distributions.

Gaussian (or normal) distributions are defined by a mean $\mu$ and standard deviation $\sigma$. Often methods used to estimate reliability assume these distributions, as using other types may require additional steps, which may not be trivial. Some authors have also assumed values for the standard deviation parameter [56] [57]. Others, assuming the distribution, obtained $\mu$ and $\sigma$ from experimental data. In [5], the normal distribution parameters and additional stochastic inputs were obtained with Digital Image Correlation and different relevant ASTM test standards, which were then used to generate random fields (an example is shown in figure 2.10). Test standards used are those developed to characterize the mechanical properties, typically a set of tensile/compressive tests on coupons with different fiber angles. It should be noted that assuming a normal distribution does not necessarily make the results diverge from experiments. Philippidis and Lekou [43] tested how several distributions matched experimental results, first using the method of maximum likelihood to choose parameters to fit the data, and then comparing the probability of the fitted distributions using the Kolmogorov–Smirnov method. It was found that normal distributions closely followed empirical data for several of the random variables.

The Kolmogorv-Smirnov method, similarly to others such as chi-square [58] and Anderson-Darling [59] tests, evaluates the likelihood of a given collection of samples corresponding to a reference PDF. These methods can be combined with experimental testing to choose an ideal distribution for each random variable. Common distributions are Normal, Weibull, lognormal, Gamma and extreme type 1 largest/smallest. Some of these are shown in figure 2.6 [43]. In that paper, all the aforementioned distributions were considered, regarding a unidirectional Glass/Polyester composite manufactured by hand lay-up, and Weibull was found to be very likely for the in-plane shear strength and poisson's ratio,

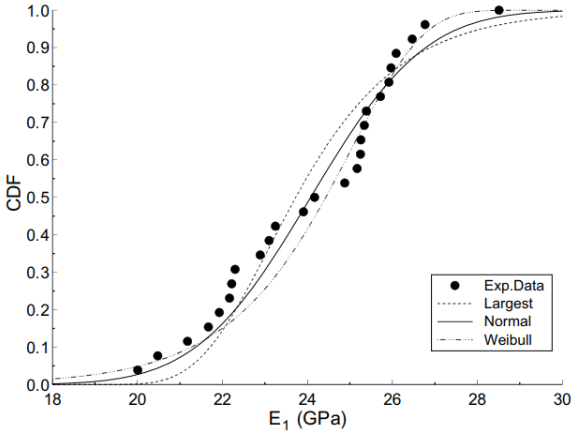


Fig. 3. Cumulative distribution for $E_1$.

**Figure 2.6:** Experimental CDF of longitudinal stiffness in unidirectional Glass/Polyester composite compared with fitted normal, weibull and extreme type 1 largest distributions [43].

while for example a lognormal distribution best matched the transverse modulus of elasticity $E_2$. It should be noted that the direct results of these methods are not the only consideration to be had when doing this type of analysis: it is highlighted in the Philippidis and Lekou paper that it may be of interest to choose the distribution that best models the low probability region, since that is often the area of interest in structural design (where failure occurs).

Recently, in [26], a sensitivity study was performed to obtain the ideal distributions for random field distributions in open-hole composite laminates of 8552-1/IM7 unitape (CFRP), which could be helpful to inform the model used in this thesis. In this case, mostly normal distributions were found to be representative. However, as is mentioned in [45], distributions and parameters chosen in different papers, for the same variables and type of composite, show a lot of variation; it is therefore important that comparisons with experiments use as input distributions fitted from empirical data of very similar specimen. Nevertheless, a table is presented in this work with values and distributions used by several authors, which may be helpful to inform the model developed in this thesis.

Finally, there is the issue of correlation between random variables: they are usually not truly independent random variables. This is an aspect that is often ignored, due to its inclusion in reliability methods being non-trivial, but may be of significance. In [59], values obtained for correlation between most variables in GRFPs (Glass Fiber Reinforced Polymers) passed the threshold of significance, using Pearson's correlation coefficient.

### 2.2.3. Reliability Methods

The reliability problem centers around the probability integral

$$P_f = \int_{X|g(X)\leq 0} f_X(X)\, d(X), \tag{2.2}$$

where $P_f$ is the probability of failure, X is a set of random variables that are considered as an uncertain part of the failure evaluation, $f_x(X)$ is the probability density function (PDF) of the vector X, and g(x) is the limit state function [38]. The latter is the expression that is used to evaluate failure, typically failure criteria, for which a value of 0 or less means failure is predicted, and value higher than 0 corresponds to a safe region. In essence, the expression represents the idea that the failure probability is given by the probability that the set of random variables is in a zone of values for which failure occurs (failure region).

Two additional things should also be defined based on equation 2.2. First is that reliability is given by

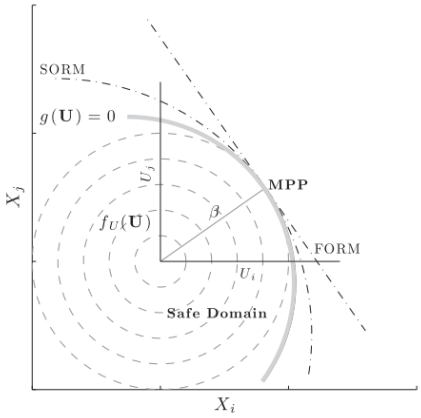


**Figure 2.7:** Geometrical interpretation of FORM and SORM [38]. $\beta$ is the euclidian distance between origin and failure function in U space (space of the transformed random variables).

$$R = 1 - P_f. \tag{2.3}$$

Second is that obtaining PDFs or statistics for any quantity of interest that depends on the random variables, such as failure probability curves, is linked to the same reliability probability integral. The limit state function (LSF) can be defined based on that quantity of interest, and a given variable can be changed systemically to successively solve the integral and generate PDFs.

In a review of reliability analysis of composites, Chiachio et al. [38] defined four types of methods used to solve equation 2.2: Fast Probability Integration (FPI) methods, Monte Carlo methods, Analytical methods and Numerical Methods. In this report, the numerical type is limited to the Stochastic Finite Element Method.

## FPI

FPI methods include the commonly used First and Second Order Reliability Methods (FORM and SORM, respectively). They work by transforming the random variables (vector $X$) into standard uncorrelated normal variables, and approximating the LSF taylor series expansion around their means. [38]

In FORM, this approximation uses only the linear terms. Because of the transformation done to the variables, the LSF is given by the distribution N($\mu_g$,$\sigma_g$). Then

$$P_f = P(g \leq 0) = \phi[\frac{\mu_g}{\sigma_g}] = \phi[\beta], \tag{2.4}$$

where $\phi$ is the standard cumulative distribution function and $\beta$ is commonly referred to as the Reliability Index[60]. By replacing the means of the random variables into the simplified LSF expression, its mean and variance can be obtained, and replaced in equation 2.4 to obtain the probability of failure. A geometrical interpretation of the method is shown in figure 2.7. The SORM is similar but includes the second derivatives of the LSF in the taylor series approximation.

FPI methods are very commonly used, oftein being found in commercial software packages, and their popularity is due to their simplicity and significant computational efficiency. FORM has recently been used, for example, to study the deflection reliability of a bridge, for comparison with an improved Monte Carlo method and the target reliability index [61]. Kamiński and Strąkowski [62] also recently proposed a FORM like method for reliability analyis in civil engineering of steel structures under fire temperatures.

However, they are mostly applicable to simple problems with few random variables[61]. This is partly due to complications in the SORM calculations but mainly because for complex problems the average

and variance of the variables included in the LSF is not known. This is because they are not the random variables that describe input uncertainties (e.g. the stiffness is an input random variable, and not the stress, the latter appearing in the LSF).

## Monte Carlo methods

Monte Carlo (MC) methods are perhaps the simplest way to assess the reliability of structures, and are commonly used as a reference for comparison of other methods [38] [63] [64]. MC works by simulating the structural response with different values for the random variables and inferring from the results of the whole pool of samples.

In terms of the integral of equation 2.2, it can be written as

$$P_f = \int_X I[g(X)] f_X(X)\, d(X), \tag{2.5}$$

where $I[g(x)]$ is 1 when $g(x) \leq 0$, which identifies failure, and 0 for g(x) higher than 0. Then random, independent samples of X can be taken, even if out of the failure region, and the probability of failure becomes the average of function I over all the samples,

$$P_f = n_f / n_s, \tag{2.6}$$

where $n_f$ is the number of samples for which failure occurred.

Reliability analysis using MC is often found combined with other more complex methods, but its accuracy and robustness makes it of general widespread use in literature. Noori and Abbas [65] recently studied the probabilistic response of portal frame structures subjected to earthquake ground motions, accounting for variability in geometry and material properties, using MC simulations and FEA.

The disadvantage of MC methods is that they are extremely computationally expensive when the real probabilities of failure are low, meaning that a lot of samples are needed for convergence. A lot of work has been done to find alternative sampling methods, for which the sampling is not so simple/direct. Some of these alternatives are Importance-Sampling [61][66], Latin-Hypercube Sampling [67] [5] [56] [68] and the Quasi-Monte Carlo method [23].

Importance-Sampling works by adapting equation 2.5 to

$$P_f = \int_X \frac{I[g(X)] f_X(X)}{h(X)} h(X)\, d(X) = \int_X H(X) h(X)\, d(X), \tag{2.7}$$

where h(X) is a new space from which X samples are taken and H(X) is the function being averaged. The h function can be picked to generate more samples in the failure region, therefore accelerating convergence.

Latin-Hypercube Sampling (LHS) works by sampling in a semi-random way from an unchanged probability density function [67]. The function $f_X(X)$ is divided into N intervals, where N is the number of samples that will be given as output. Then, for each interval, X is sampled randomly. Unlike standard MC, in LHS each sample is not taken independently of other samples, since memory of the previously chosen intervals must be kept to make sure there is no repetition.

As an example, in figure 2.8, a graphical representation of Latin Hypercube Sampling of N=8 samples from the standard normal distribution is shown. The CDF is divided into N=8 equally probable intervals, and each interval is randomly sampled from once, by locally inverting the CDF. Random MC is equivalent to this process if only one interval was used, and sampled from 8 times.

This concept works for any number of variables that is being sampled. Figure 2.9 shows a representation of LHS of N=10 samples of an X vector of 2 random variables, compared with MC sampling for the same scenario. In the LHS case, no row or column is sampled from twice.

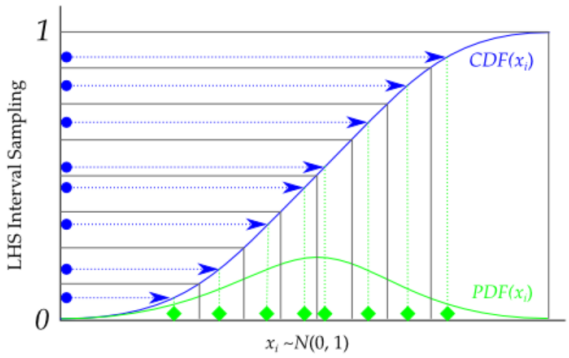


**Figure 2.8:** LHS of 8 samples from the standard normal distribution[1].

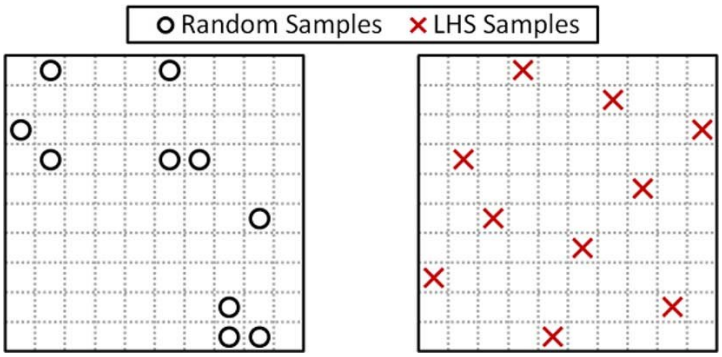


**Figure 2.9:** MC sampling vs LHS of 10 samples of 2 random variables [69].

Because the probability functions of each variable are always sampled from at every interval, LHS has been found to be significantly more efficient than Monte Carlo sampling for the purpose of simulations [67] [5]. In section 3.1, an explanation of LHS application in the context of this thesis is given.

## Analytical Methods

Some analytical solutions have been developed for the probability integral. These generally consist of expressions for the LSF cumulative distribution function (CDF), that are derived for particular case studies [38]. When the expression for the CDF is known, the probability of failure is easily calculated by integrating it in the failure domain.

The Edgeworth Expansion Method was developed in [70] for the case of uniaxial tension in off-axis composite coupons. It has also been applied for the general plane-stress case of a composite layer in [71], and further developed to include thermal and elastic material properties, as well as stochastic strengths, in [43]. Alternatively to this method, which calculates the CDF expression from the statistical moments of the LSF, themselves obtained from those of the random variables, Pearson's Empirical Distribution method obtains the CDF by curve fitting empirical distributions.

Analytical methods are by far the least computationally expensive, and are therefore ideal for simple cases with few random variables. They are not generally applicable, however, as LSF expressions have to be developed and changed depending on the case study. Additionally, much like with FORM, they require knowledge of the distributions of the random variables that appear in the failure function.

## Stochastic Finite Element

The Stochastic Finite Element Method (SFEM) works generally by applying the standard FEA, but with each element having different values of the random properties. Each random variable becomes a

[1] https://pythonhosted.org/pyDOE/randomized.html

random field (RF) over the finite elements. This type of simulation may take into account the spatial correlation of material parameters, or, in simpler applications, they may be attributed to each element randomly. The use of RFs has the advantage of considering the relationship between local and global mechanical properties for the different points of the model [72], as well as more realistically representing the stochastic failure mechanisms in composites. An example of this is identified in [24] and [25]: fiber failure happens progressively with an initial failure of weaker fibers that leads to increased stress concentrations in neighbouring intact fibers and their ultimate failure - therefore, if deterministic values for fiber strengths are used, the real (stochastic) nature of fiber failure is not captured. As previously mentioned, FRP materials show considerable variance of their material properties throughout any given specimen, and SFEM is usually the only method that includes this type of variability.

Evidently, another one of the main advantages of the SFEM is that it incorporates the most powerful and widely used structural analysis tool, adding a probabilistic nature to it. This makes it the best method to apply to complex and realistic problems and geometries [40]. It is therefore on these numerical methods that the growing attention on stochastic mechanics has centered.

Depending on the formulation and type, it may be intrusive and non-intrusive. Intrusive methods require altering the FEA calculations and matrices, while non-intrusive methods have a ”black-box” formulation, meaning they can be coupled with any FEA software without effort. The latter have the advantage of more easily accessing already established and efficient solvers, allowing for robust implementations of stochastic analysis with complex and state-of-the-art methods (e.g. XFEM or degradation models). Examples for both of these types of solutions are given below.

The two main SFEMs found in literature are the Perturbation Method and the Spectral Stochastic Finite Element Method.

**Perturbation Method**

The perturbation method works by expanding the system matrices about the means of the random variables through the Taylor series expansion [39]. The equilibrium equation for static problems is

$$K(\alpha_i)u(\alpha_i) = F(\alpha_i), \tag{2.8}$$

where K, u and F are the stiffness matrix, displacement and force vectors respectively, and $\alpha_i$ are the N random variables. Assuming zero-mean and $\alpha_i << 1$, representing deviations from the mean of the random properties, the stiffness matrix can be written as

$$K = K^0 + \sum_{i=1}^{N} K_i^I \alpha_i + \frac{1}{2}\sum_{i=1}^{N}\sum_{j=1}^{N} K_{ij}^{II}\alpha_i\alpha_j, \tag{2.9}$$

where $K^0$ is the stiffness matrix with the mean values ($\alpha_i = 0$) and $K_i^I$ and $K_{ij}^{II}$ are the first and second partial derivatives of K with respect to the random variables (i and ij), at $\alpha_i = 0$, respectively [57]. Here the expansion was limited to the second moment because calculation of higher moments is scarce in literature, due to its computational cost.

The same can be done for the force and displacement vectors, where the displacement partial derivatives can be calculated from the known vectors' derivatives. Then, from the resulting truncated Taylor series, one can calculate the mean and covariance matrices of the displacement.

This method is frequently found in literature, since despite requiring calculation of several partial derivatives, the computational cost of which is significant, it is less computationally expensive than other SFEMs. From simpler applications [73], it has been applied to non-linear structural dynamics [74], combined with the Extended Finite Element Method (XFEM) [57] to solve fracture mechanics problems, and adapted for meshless FEA of static linear structural problems [75].

Kamiński and Strąkowski [62] recently used an iterative generalized perturbation approach for obtaining the probabilistic response of steel when subjected to fire temperatures. A perturbation-based approach

has also been applied to stochastic homogenization analysis of porous materials considering the randomness of the micro-structure [50], the latter determining the influence on the homogenized elastic property.

Despite its wide applicability and development, the perturbation method is usually limited to low coefficients of variation (10 to 15%) [39] and to obtaining the first statistical moments of the response to Gaussian random variables. Some authors have, nevertheless, worked to surpass these limitations, notably in [76], for high variance of random variables, and recently in [77] to allow for triangular and uniform probabilistic distributions.

The limitation in variance of the random properties is particularly disadvantageous for FRP materials, for which spatial variation can be significantly higher than those values. In [5], Digital Image correlation was used to measure displacements and strains in tensile testing of CFRP coupons, and therefore calculate the spatial distribution of mechanical properties. Figure 2.10 shows results for the transverse stiffness, for which the obtained standard deviation is 22% of the mean. This shows the importance of using a method that is accurate for high coefficients of variation in composite SFEM.

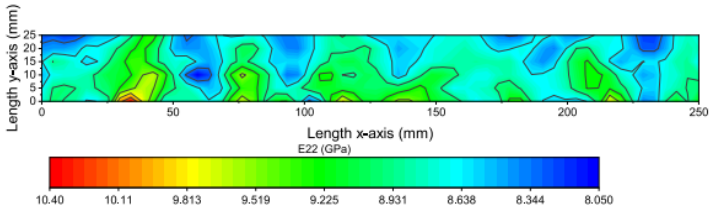


**Figure 2.10:** Spatial distribution of transverse stiffness in CFRP coupon [5].

### Spectral Stochastic Finite Element Method

The Spectral Stochastic Finite Element Method (SSFEM) [78] typically works by representing a spatially varying random property $w$ with the Karhunen-Loève (KL) expansion, which discretizes continuous random fields into

$$w(x,\theta) = \mu_w(x) + \sum_{i=1}^{\infty} \sqrt{\lambda_i}\phi_i(x)\xi_i(\theta), \tag{2.10}$$

where $\mu_w(x)$ is the average of the property at that node, $\lambda_i$ and $\phi_i$ are the eigenvalues and orthonormal eigenfunctions, respectively, of the covariance kernel, and $\xi_i$ are gaussian random variables of 0 mean and unit standard deviation, which confer the stochasticity to the expression. By truncating the sum in equation 2.10, a random field can be represented with a limited number of variables. More details on how to use the KL expansion are given in section 2.2.4.

The covariance kernel in this case describes the relationship between the random field values of points in space, so it depends on the coordinates of two points, $(x_1, y_1)$ and $(x_2, y_2)$. The fact that there is correlation between the values in different points of the structure makes distributions more realistic and results converge faster. The values being generated with few random variables makes the KL more computationally efficient than random MC sampling of values at every necessary point in space.

The covariance kernel, and therefore the eigenvalues and eigenvectors, are usually not known for the response variable. As defined by Ghanem and Spanos in their textbook [63], there are two different approaches to this problem. The first one is the homogeneous chaos, or polynomial chaos expansion, which expands the solution with a Fourier-type series that depends on the KL random variables $\xi_i(\theta)$. The second one is sampling, through MC methods, to obtain response statistics. The latter is often combined with the galerkin method.

In the polynomial chaos method, the displacement vector is written as

$$U(\theta) = \sum_{j=0}^{\infty} U_j \Psi_j(\theta), \tag{2.11}$$

where $U_j$ is a set of deterministic coefficients and $Psi_j$ is an orthogonal basis of polynomials in $\xi_j$ [53] [64].

The orthogonal basis is usually obtained from rewriting

$$U(\theta) = a_o\Gamma_0 + \sum_{i_1=0}^{\infty} a_{i_1}\Gamma_1(\xi_{i_1}(\theta)) + \sum_{i_1=0}^{\infty}\sum_{i_2=0}^{\infty} a_{i_1 i_2}\Gamma_2(\xi_{i_1}(\theta), \xi_{i_2}(\theta)) + ..., \tag{2.12}$$

where

$$\Gamma_n(\xi_{i_1}, ..., \xi_{i_n}) = e^{\frac{1}{2}\xi^T\xi}(-1)^n \frac{\partial^n}{\partial\xi_{i_1}, ..., \xi_{i_n}}. \tag{2.13}$$

The coefficients of equation 2.11 can be used to calculate the probabilistic moments of the response. Some authors have used the so called galerkin projection to solve FEA systems of the type

$$\sum_{j=0}^{N_p}\sum_{m=0}^{N_{KL}} \xi_m\Psi_j(\xi)[K_m]U_j = \sum_{m_0}^{N_{KL}} \xi_m f_m, \tag{2.14}$$

where the stiffness matrix and force vector are given by a KL expansion with $N_{KL}$ terms and the response by a polynomial chaos expansion with $N_p$ terms [79][64]. In [79], this method is used for response prediction of unidirectional FRP plates with variable material properties under tension, and was found to be more efficient than Monte Carlo and more accurate than the perturbation method for high standard deviation values. In [64], this approach is extended to account for the multi-layer effect and variability.

The galerkin projection method shows promising computational efficiency, but has the limitation of being intrusive, meaning that the system matrices are changed from those of the deterministic analysis, making it impractical to combine with commercial FEA software.

Another way of calculating the coefficients in 2.11 is by using the collocation points method [80] [81]. In this approach, sampling is used to generate collocation points in the random space, and the deterministic response is calculated for those samples. Then coefficients are calculated to vanish the error in the FE system equation.

In [80], the fiber orientation of FRPs is considered a random variable for vibration analysis of rectangular composite plates through the SSFEM, the orientation leading to stochasticity in the stiffness and mass matrices. The effect of this uncertainty on the mode shapes and frequencies was determined. The same author, in [80], studied the impact of uncertainty in elastic and damping parameters on the acoustic transmission loss of FRP plates, for different frequencies. The random properties themselves were modelled with the polynomial chaos expansion. Both of these studies used commercial deterministic FEM software to generate the collocation points, and found this method to be much more computationally efficient than standard Monte Carlo.

The major advantage of collocation point methods, whether through the polynomial chaos expansion or alternative algorithms [82], is that a metamodel (e.g. polynomial expression) is created to describe the relation between the output and input. This metamodel is much simpler than the full model that is sampled from in Monte Carlo methods, and can be created using established FEA software through a black-box SFEM formulation.

However, the Polynomial Chaos methods are difficult to generalize, as even with the non-intrusive approach knowledge of the system for which the error must be minimized must be had. Furthermore, usually just the first statistical moments are obtained, for few random variables. Applications where any properties of a composite structure are given known probability distributions and progressive failure analysis is performed are not found in literature, as this method may not be indicated for it.

The KL expansion is often combined with Monte Carlo sampling to obtain probabilistic responses. It is a simple process, where the random properties in different points are calculated through equation 2.10,

and those values are given to a FEA solver, for any given sample of random variables $\xi$. In [56], the KL expansion is combined with LHS to obtain response PDFs of general structures and load cases using Finite Element solves Abaqus. Most notably, in this paper the Random Field (RF) and FE meshes are completely separate, which is useful to maximize computational efficiency by optimizing each mesh. In [5], progressive failure analysis of FRP rectangular plates is done by combining KL and LHS and using the Puck failure criterion, which gives the probability for any given load of a specific failure mode happening, as well as final failure PDFs.

By obtaining the response statistics with LHS, there is evidently the limitation of the computational cost being higher than for non-sampling methods. However, considering the goal of analyzing FRP laminates with generic geometries, the MC+KL method shows great promise.

KL allows consideration of spatial variation of properties, which is key for realistic probabilistic modelling. It also creates realistic distributions which are relatively fast to generate. Most importantly, the non-intrusive nature of the process allows the use of commercial FE software. Because the model to be developed in this thesis should work for case studies considerably more complex than the rectangular plates of [5], using an external solver seems like a good choice, in order to also have a faithful modelling of all the failure modes mentioned in section 2.1. Finally, the MC+KL can be generally useful for future applications in composite analysis, since its formulation hardly changes with different geometries, and any result statistics can be obtained, independently of the input.

**Application to case study**

In the descriptions of each reliability method, several examples from literature of probabilistic analysis of composites were given. Most work that is found, though, centers around rectangular laminated FRP plates, and random fields or the SFEM are not so commonly applied. Modelling of structures with geometric details and spatial variation is significantly more complex: calculations with CLT must be replaced by FEA for arbitrary geometries, as no analytical expression for the solution can be exploited for the reliability analysis, meaning non-SFEM methods are not applicable; several failure modes can be relevant and complex modelling strategies may be required; with regards to considering spatially varying properties, again SFEM is the only available option, and generating fields of these properties throughout the composite specimen is a non-trivial matter. Additionally, although extensive work has been done in probabilistic failure predictions of composite specimen, only in a few cases were failure-dependent criteria used, or damage accumulation considered.

In this research, the model will be used to assess the reliability of open-hole laminates in tension, as an example of a geometric detail to be accounted for. In fact, some examples exist in literature of stochastic analysis of open-hole composite plates. In [41], MCS is used to generate random properties for a whole specimen, which is then analyzed through the deterministic FEM. In [22], the SFEM is used for progressive damage analysis of PEEK laminates. Four failure modes were considered (fiber and matrix tension and compression, shear, and delamination), and several criteria for damage initiation and propagation are compared. All of this was modelled in Abaqus, and the stiffness and strength properties of each element are sampled individually from gaussian distributions. Failure statistics are obtained through running multiple samples.

More recently, Pitz and Pochiraju [23] studied the influence of spatial variation of strengths in the damage propagation in open-hole composites, specifically the effect under tension on the mean crack length. Similar modelling techniques to [22] were used, and a Quasi-MC sampling method was used to generate the random fields. Finally, in [25] and [24], Monte-Carlo based probabilistic fatigue damage analysis methods for FRPs were developed, the latter considering random fields of fiber strengths and modelling the specimen on Abaqus, while the more recent one extended the previous approach to predict the ultimate failure caused by accumulation of damage.

This overview shows that extensive work has been done to accurately model accumulation of damage in FRPs, and some authors have combined these models with probabilistic approaches. However, the SFEM used for structures with geometric details is usually Monte Carlo based, which is very inefficient and limiting in the computational sense, since properties have to be generated for each element and no correlation is taken into account. There is, to the best of the author's knowledge, a gap in the literature corresponding to applying the SFEM with the properties and strengths as correlated random fields,

generated through an expansion such as KL, to progressive damage analysis of composite structures with generic geometries.

The SFEM, specifically using the KL expansion combined with MCS of deterministic FEA software, has been identified as a promising process for this type of analysis. Several authors, some already mentioned, have applied SFEM in commercial FEM software. Depending on the intrusive nature of the method, a few papers have used element-defining subroutines (UEL in Abaqus) to construct stochastic stiffness matrices [56][83][46]. Abaqus subroutines are used for applications that aren't built in the software, such as defining custom material behaviour. In [56], the KL random fields are the input of custom-made stiffness matrices in a UEL subroutine. However, material property and strength definition at different spatial points has recently been done by other authors by simply defining the material as a user defined field dependent on the coordinates of the calculation (integration) points, through the USDFLD Abaqus subroutine [82]. Other approaches include defining different materials at different elements in the input file [84]. These applications have generally shown acceptable computational efficiency, and have allowed for some complex SFEM applications.

## Surrogate Models

It is common to use surrogate models to replace the evaluation of the LSF, which in the case of SFEM means replacing the FE solver with a simpler system derived from results. The two most common surrogate model types are polynomial-based Response Surface Methods (RSMs) and Artificial Neural Networks (ANNs)[38].

The RSMs (here refering only to the polynomial-based ones) work similarly to what was referred to earlier as the collocation points method, which uses the polynomial chaos expansion for the solution. The LSF is replaced by a polynomial expression, which is obtained by first sampling the FE solver and then accomplishing some type of regression analysis to calculate the coefficients of the explicit expression. In [42], the RSM was combined with MCS for reliability analysis of aluminium–carbon fiber/epoxy composite laminates for pressure vessels. In [26], a systemic probabilistic analysis approach was developed for the open-hole tension case for FRP laminates, again by combining MCS with the RSM, and varying all material and strength properties. Note that in neither of these examples was spatial variation of the properties considered.

Another method found in literature is sampling an ANN instead of an FEA solver to obtain response statistics. ANNs are machine learning computational models, inspired by biological neural networks and organization, that can be trained from datasets to have predictive abilities. This has been found to work better than RSM for more complex problems with several random variables [38]. Of the two, it is the one more usable for the SFEM, where random fields are considered.

In [66], an ANN is sampled instead of an FEA solver using different Monte Carlo methods, to obtain the probabilistic response to uncertainty in the material properties of composite laminates (without variation within the specimen). Compared to sampling of the FE solver, this method of obtaining the reliability values was found to be much faster. In [44], the KL+MC SFEM developed in [5] was used to train a special type of ANNs, which are two-dimensional Convolutional Neural Networks, that are advantageous when there are spatial relations in the data. The ANN was trained to predict the failure of rectangular FRP plates under tension, from the values of the strains at 20% of the ultimate load, and the predictions matched well with the experimental results.

Surrogate models, especially ANNs, for the aforementioned advantages, could serve as an advantage to the SFEM used for specimen with complex geometries. Case studies may include many failure modes and variables, so a simplified replacement model could be necessary to overcome computational effort problems. Additionally, an ANN has already been used with the KL+MC method for another case study, so precedent for this exists in literature.

### 2.2.4. Random Fields and Karhunen-Loève expansion

When considering spatial variation of a given variable, it can be referred to as a random field (RF). Random fields exist on a continuous domain, and therefore contain infinite random variables [85]. To

make calculations and model these fields computationally, only a limited amount of points in space can be considered, so the discretization is necessary.

**KL expansion**

The most common method of RF discretization is the already mentioned KL method [78]. The method uses a covariance kernel, which expresses the correlation of the random variable between two points in space, to expand at each point in a truncated series around the mean. In the end, the random value is given by equation 2.10, truncated at M iterations of the sum. The equation includes the eigenvalues $\lambda_i$ and eigenfunctions $\phi_i$ of the covariance function (or autocovariance, since the variable is the same). Those are obtained through the Fredholm integral

$$\int_{\Omega_{2e}} C(\boldsymbol{x}_1, \boldsymbol{x}_2)\phi_k(\boldsymbol{x}_2)\, dA_{2e} = \lambda_k \phi_k(\boldsymbol{x}_1), \tag{2.15}$$

where $\boldsymbol{x}_1$ and $\boldsymbol{x}_2$ represent the x and y coordinates in RF elements 1 and 2, respectively, and $A_{2e}$ is the element 2 domain $\Omega_{2e}$ in terms of $\boldsymbol{x}_2$ ($x_2$,$y_2$) [56]. This integral can usually only be solved numerically. The most common approach is to use Galerkin methods, specifically finite element discretization and Galerkin when working in a 2D space. However, other Galerkin approaches exist, such as spectral and meshless, and, besides Galerkin, the Nystrom and collocation methods can be found in literature [85]. An additional option, explored in [86], and suggested in [87], is to enclose the general geometry in a bounding 2D or 3D rectangular geometry, for which the analytical solution of the integral is known. From that solution, the one for the intended geometry can be "cut out". As mentioned in [87], this option, despite being suggested originally, has not received due attention in literature: although re-calculating some parameters of the covariance function may be necessary, the computational advantage may be significant, and obtaining the solution itself becomes much simpler.

In this research, the Galerkin FE discretization, as well as the bounding box formulation, will both be used to generate RFs, and the specifics of these methods are given, respectively, in sections 3.1 and 3.2.

**Alternatives**

Although the KL expansion is far and ahead the most common random field discretization method found in literature, some authors have developed alternative approaches. Two recent works [72][84] have used a Cholesky decomposition of the covariance matrix, combined with ordinary Kriging, to produce realizations of sampled random fields. Additionally, the Optimal Linear Estimation (OEL) Expansion, developed in [88], has been used to discretize non-gaussian 1-D random fields of elastic properties in sandwich beam structures [89]. That approach was combined with Monte Carlo to quantify the effect of the uncertainties on the dynamic response of the structure. A note should be made, however, that the OEL expansion has been shown to constitue a special case of the Nystrom method of solving the KL Fredholm integral [85].

The alternatives found in literature are often less computationally expensive than KL, but because for 2D random fields this is by far the most common approach, it seems that for the case study of this thesis the KL expansion is the more promising option.

## 2.3. Research Questions and Objective

The literature study that was conducted revealed a gap in existing work which will be addressed in this thesis. Section 2.1 summarized extensive theory and research that has been done in relation to deterministic progressive failure analysis of composites. The section, starting from the general context of composite structures, highlighted the relevance of that type of analysis, and how current methods are insufficient and always in development.

Then section 2.2 focused on reviewing literature relative to reliability analysis of composites. Again, the relevance of adding a probabilistic nature to progressive failure analysis of composites was explained. Then different methods of reliability analysis found in published work were addressed, and evaluated in terms of their applicability to the intended research objective. It was found that developing previous

SFEM work that used the Karhunen-Loève method and Monte Carlo Simulations would be the best starting point. Additionally, combinations with commercial FEA software and/or surrogate models were commonly found options that revealed a lot of promise. When reviewing this part of literature, it became clear that few authors have applied stochastic methods to progressive failure analysis of composites - even in the limited work that exists where strengths and material properties are considered random variables usually only First-Ply-Failure is considered.

As previously discussed, recent work that is being developed already made the progress of using mode-dependent criteria with a KL+LHS SFEM, applying it to rectangular laminates. Extending the analysis to structures with complex geometries, such as the open-hole case, was chosen as a novelty for this type of work, presenting new modelling challenges. The review of papers that performed stochastic analysis of such specimen showed that the methods that have been applied use inefficient Monte Carlo methods, or don't consider spatial variation at all.

To conclude, this thesis aims to improve current applications of reliability methods in progressive failure analysis of composites, since to the best of the author's knowledge no work exists that has applied the Karhunen-Loève method, or another Random Field discretization strategy, combined with sampling for the progressive failure analysis of composite laminates with complex geometries. This reliability method will be integrated with the Abaqus FEA solver.

The **main question** to be answered with this research is: **To what extent can the SFEM be used to predict the reliability and probabilistic damage evolution of composite laminates with geometric details and spatially varying properties?**

The following **sub-questions** should be answered in relation to the main question:

- What strategies for generating random fields and obtaining the response can be used to make a general-purpose SFEM as computationally efficient and reliable as possible?
- What failure criteria give the most accurate results with the SFEM?
- How do the experimental results compare with the SFEM predictions?

# 3

# Generating Random Fields

This section details the methods used to generate 2D random fields of the material properties of interest to composite failure analysis. Specifically, the Karhunen-Loève discretization method is used, in a way that is applicable to any arbitrary 2D geometry. In sections 3.1 and 3.2, two different algorithms developed in MATLAB are detailed, which use the method differently. The first uses a galerkin finite element approach, which is the most common in literature, while the second follows recent work [86] where the analytical solution over a bounding box is used. These approaches will be compared and one will be chosen for the case study.

## 3.1. Applying the Karhunen-Loève - Galerkin discretization

Since in this research we will work with 2D discretization, the widespread approach of discretizing in a finite element mesh with the galerkin method, to solve the integral in equation 2.15, is first used. Because throughout this report there will be mention of two distinct Finite Element meshes, the mesh used for the galerkin method will be refered to as the RF mesh, while the one used for FEA will be the FE mesh.

In this method, the orthonormal eigenfunctions are approximated over each element with

$$\phi_i(\boldsymbol{x}) = \sum_{j=1}^{nnod_{RF}} L_j(\boldsymbol{x}) d_{ij} =< L(\boldsymbol{x}) > [d], \tag{3.1}$$

where from the created RF mesh comes a group of $nnod_{RF}$ shape functions for each element and $nnod_{RF}$ is the number of nodes per RF element. Finally, $d_{ij}$ is the ith covariance eigenfunction value at node j. This discretization tactic is in fact analogous to the finite element method used in structural analysis, since the solution at the nodes of each element is calculated and interpolated at other coordinates with the shape functions. These shape functions $L_j(\boldsymbol{x})$ are usually the same as those used in FEA. For the formulation and examples of this report, the RF mesh will be composed of linear quadrilateral (Q4) elements, represented in figure 3.1. The elements and their shape functions are defined in isoparametric element coordinates $\xi$ and $\eta$, with the shape functions for each node being

$$\begin{aligned} L_1 &= \frac{1}{4}(1-\xi)(1-\eta) \\ L_2 &= \frac{1}{4}(1+\xi)(1-\eta) \\ L_3 &= \frac{1}{4}(1-\xi)(1+\eta) \\ L_4 &= \frac{1}{4}(1+\xi)(1+\eta). \end{aligned} \tag{3.2}$$

The isoparametric formulation is used to map from the possibly irregular shape of the elements to a regular one in the ($\xi$,$\eta$) space. The x and y coordinates of any point in the element can be obtained with

$$x_p = \sum_{m=1}^{4} L_m(\xi_p, \eta_p) X_m, \tag{3.3}$$

with $X_m$ being the x or y coordinates of the mth node, $x_p$ the x or y coordinate at the point of interest and $\xi_p/\eta_p$ the coordinates of the point in the isoparametric space.

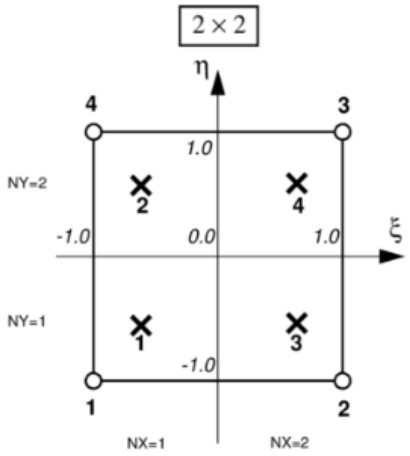


**Figure 3.1:** Q4 element [90].

Substituting equation 3.1 into equation 2.15 results in

$$\int_{\Omega_{2e}} C(\boldsymbol{x}_1, \boldsymbol{x}_2) < L(\boldsymbol{x}_2) > |J_e| \, dA_{2e}[d]_e = \lambda_k < L(\boldsymbol{x}_1) > [d]_e, \tag{3.4}$$

where $|J_e|$ is the jacobian determinant that relates the isoparametric coordinates, in which the integral will be solved, to the global ones (x and y). The determinant is given by

$$\frac{dx}{d\xi}\frac{dy}{d\eta} - \frac{dx}{d\eta}\frac{dy}{d\xi}, \tag{3.5}$$

where each derivative can be calculated by differentiating the expression in equation 3.3.

The expression in equation 3.4 is actually not equivalent to the original one, because we approximate the eigenfunctions by truncating the sum at $nnod_{RF}$. There is a residual error in this approximation, which is minimized with the Galerkin weighted residual method. Assuming the error is orthogonal to the approximating space, it is equivalent to write, with the same set of shape functions on both sides, and integrating to minimize the residual [63]:

$$\begin{aligned} &\int_{\Omega_{1e}} \int_{\Omega_{2e}} C(\boldsymbol{x}_1, \boldsymbol{x}_2) < L(\boldsymbol{x}_1) >^T < L(\boldsymbol{x}_2) > |J_{e1}||J_{e2}| \, dA_{2e} dA_{1e}[d]_e \\ &= \lambda_i \int_{\Omega_{1e}} < L(\boldsymbol{x}_1) >^T < L(\boldsymbol{x}_1) > \, dA_{1e}[d]_e. \end{aligned} \tag{3.6}$$

The rest of the process is similar to the FEM, where the problem is generalized in matrix form with all elements of the mesh assembled, by adding elemental matrices in succession. Elemental matrix $C_e$,

with dimensions $nnod_{RF}$ by $nnod_{RF}$, for each combination of elements 1 and 2, corresponds to the left part of equation 3.6:

$$\boldsymbol{C}_e = \int_{\Omega_{1_e}} \int_{\Omega_{2_e}} C(\boldsymbol{x}_1, \boldsymbol{x}_2) < L(\boldsymbol{x}_1) >^T < L(\boldsymbol{x}_2) > |J_{e1}||J_{e2}|\, dA_{2e} dA_{1e}. \tag{3.7}$$

Elemental $\boldsymbol{B}_e$ matrix, with the same dimensions, corresponds to the right part:

$$\boldsymbol{B}_e = \int_{\Omega_{1_e}} < L(\boldsymbol{x}_1) >^T < L(\boldsymbol{x}_1) > |J_{e1}|\, dA_{1e}. \tag{3.8}$$

Global matrices *C* and *B* have dimensions $N_{RF}$ by $N_{RF}$, $N_{RF}$ being the total number of nodes of the RF mesh. Matrix C is built by adding elemental matrices $\boldsymbol{C}_e$ to the lines corresponding to element 2 nodes and columns corresponding to element 1 nodes. Matrix B is built by adding elemental matrices $\boldsymbol{B}_e$ to the lines and columns corresponding to the element nodes [91]. Note that these global matrices will be symmetric as long as the covariance function is symmetric.

A second error will originate from truncating the sum in 2.10 at M terms. This error exists for any solution with the KL expansion, since this truncation is necessary for discretizing the field. In the case of Galerkin, the number of terms used in the expansion (M) is limited by the number of nodes $N_{RF}$.

Once matrices *B* and *C* are assembled, a diagonal matrix $\Lambda$ with the first M eigenvalues is then assembled:

$$\Lambda_{ij} = \delta_{ij}\lambda_i, \tag{3.9}$$

where $\delta_{ij}$ is the kronecker delta. Then the full mesh version of equation 3.6 has the generalized eigenvalue formulation:

$$CD = BD\Lambda. \tag{3.10}$$

The equation is solved for eigenvectors D and eigenvalues $\Lambda$, D containing the autocovariance function eigenfunction values at all RF nodes (lines correspond to the nodes and columns to different eigenfunctions), with the columns ordered in the same way as the eigenvalues. The first M eigenvalues (in descending order) and corresponding eigenvectors are then used in the solution. Values of the D matrix can be replaced in 3.1 to obtain the eigenfunction values at any point in RF space, and the random fields can be calculated with equation 2.10, by generating random variables $\xi$. These random variables are gaussian, with mean 0 and standard deviation 1.

Some extra steps must be described that are required for our application. The RF mesh should be able to have any arbitrary 2D geometry. It is also decided that the FE mesh should be decoupled from the RF mesh. The reasoning for this is that these meshes have separate requirements: the FE mesh will often need to be more fine, specifically in regions where the stress/displacement results may be of most interest, while the RF mesh's only requirement is to be fine enough to represent the spatial variation of properties, depending on how correlated the field is. The method will then be more robust if it is able to generate FE Random Fields from any RF mesh (in the same geometrical domain, evidently).

**Covariance Function**

The covariance function is chosen to be

$$C(\boldsymbol{x}_1, \boldsymbol{x}_2) = \sigma_w^2 \exp(-\frac{|x_1 - x_2|}{b_{cX} L_{D1}} - \frac{|y_1 - y_2|}{b_{cY} L_{D2}}), \boldsymbol{x}_1, \boldsymbol{x}_2 \in \Omega, \tag{3.11}$$

which has received plenty of attention in literature and often been used to model spatially varying material properties [63] [5] [56].

The parameters $b_{cX}$ and $b_{cY}$ will be referred to as correlation parameters, as they define how correlated the field is. The values in the denominator $b_{cX} L_{D1}$ and $b_{cY} L_{D2}$ are often replaced by a single parameter $L_C$, which is the correlation length, but this way allows us to define the correlation length in relation to the real field dimensions $L_{D1}$ and $L_{D2}$. For an arbitrary RF mesh, $L_{D1}$ is given by

$$L_{D1} = x_{maxRF} - x_{minRF}, \tag{3.12}$$

with $x_{maxRF}$ and $x_{minRF}$ being the maximum and minimum x coordinates of RF nodes. $L_{D2}$ is obtained in the same way for the y direction. Finally, $\sigma_w$ is the point-wise standard deviation, since it is the value of the covariance function when $x_1 = x_2$. Note that this standard deviation is the one for a single point, in many RF cases, and not the spatial standard deviation within one RF. The latter can be adjusted with $b_{cX}$ and $b_{cY}$, without affecting the point-wise one.

Considering the chosen covariance function, it can be observed that the $\sigma_w^2$ element will affect only the eigenvalues, in a linear way, thus it is equivalent to write

$$C(\mathbf{x}_1, \mathbf{x}_2) = \exp(-\frac{|x_1 - x_2|}{b_{cX} L_{D1}} - \frac{|y_1 - y_2|}{b_{cY} L_{D2}}), \mathbf{x}_1, \mathbf{x}_2 \in \Omega \tag{3.13}$$

and change equation 2.10 to

$$w(x, \theta) = \mu_w(x) + \sigma_w \sum_{i=1}^{\infty} \sqrt{\lambda_i} \phi_i(x) \xi_i(\theta). \tag{3.14}$$

**Computing the integrals**

This change is useful because it means the eigenvalue problem does not have to be solved multiple times (e.g. for every material property) as long as the mesh stays the same. The integrals in equations 3.7 and 3.8 will not be computed analytically, but rather with the Gauss-Legendre quadrature rule. In figure 3.1, the gaussian, or integration points, of the RF elements are highlighted. Their coordinates in the isoparametric space are $\xi = \pm\frac{1}{\sqrt{3}}$ and $\eta = \pm\frac{1}{\sqrt{3}}$. The matrix calculations then become

$$\mathbf{C}_e = \sum_{GP_1=1}^{4} \sum_{GP_2=1}^{4} C(\mathbf{x}_{GP_1}, \mathbf{x}_{GP_2}) < L(\mathbf{x}_{GP_1}) >^T < L(\mathbf{x}_{GP_2}) > |J_{e1}||J_{e2}| \, dA_{2e} dA_{1e} \tag{3.15}$$

and

$$\mathbf{B}_e = \sum_{GP_1=1}^{4} L(\mathbf{x}_{GP_1}) >^T < L(\mathbf{x}_{GP_1}) > |J_{e1}| \, dA_{1e}, \tag{3.16}$$

where the x and y coordinates of the gaussian points are calculated with equation 3.3. Depending on the covariance function and shape functions used, the number of integration points required for a good approximation of the integrals may be higher than 4, specially in the $\mathbf{C}_e$ calculation [91]. However, linear elements with 4 gaussian points were found to give good approximations, as will be shown.

**Normalization of eigenvectors**

Once all matrices have been calculated, the eigenvectors and eigenvalues are obtained with MATLAB's *eig()* function, and transformed from any resulting complex form to a real form with the *cdf2rdf* function, according to what is recommended in [92]. This results in eigenvectors that have been normalized to 1. Like has been mentioned before, the eigenfunctions of the covariance kernel must be orthonormal in the RF domain. Although the eigenvectors from 3.10, which contain sampled values of these eigenfunctions, have norm 1, that doesn't make the eigenfunctions orthonormal in the RF domain, and so an additional normalization process is necessary.

If $\phi_i(\mathbf{x})$ is normal in a domain $\Omega$, then

$$\int_{\Omega} \phi_i^2 = 1. \tag{3.17}$$

Therefore, by calculating this integral for every eigenfunction, we can then divide the eigenfunctions by the square root of the result, such that

$$\int_{\Omega} (\frac{\phi_i}{\sqrt{\int_{\Omega} \phi_i^2}})^2 = 1. \tag{3.18}$$

To solve the integral in 3.17, it is calculated separately for every RF element, such that the process works for any geometry. Over each element, the integral is approximated as the volume of the solid formed by the nodal values of $\phi_i^2$ and the xy plane. The resulting eigenfunctions after normalization are approximately orthonormal.

**Mapping from RF mesh to FE mesh**

Once the generalized eigenvalue problem has been solved, the eigenfunction values at the RF nodes are known. The objective of the process is to generate RFs of values for FEA. In FEA, the material property values are taken at the integration, or gaussian points, since, similarly to the galerkin procedure, the integral that must be calculated to obtain the stiffness matrix is solved with the gauss-legendre quadrature rule. Many strategies can be used to discretize from the RF mesh to a FE model, like averaging over an element or interpolation at different points of interest such as element centroids or nodes [40].

The chosen option was to interpolate at the gaussian points of the FE mesh. The advantages of this option are the excellent resolution of the Random Field and the direct transfer of values from MATLAB to the stiffness matrices computed in the FE software, with no interpolation being required of the latter. The main disadvantage is the higher computational cost.

Equation 3.1 can be used to calculate the eigenfunction values at the FE nodes, using the RF nodal values of the RF element in which they are inserted. The first step is to go through every RF element and, using MATLAB's *inpolygon* function, find which FE nodes are inside or in the border of that element. Because of FE nodes that are borders, a second process must exist to retract them from all but of the RF elements (choice is arbitrary).

Then, to use equation 3.1, the coordinates of the FE nodes in the isoparametric space must be known. From equation 3.3, the following equations can be written, where $X_m^j$ and $Y_m^j$ are the coordinates of the nodes of RF element j, to which the FE node is assigned to:

$$x_{FE} = \sum_{m=1}^{4} L_m(\xi_{FE}, \eta_{FE}) X_m^j \tag{3.19}$$

$$y_{FE} = \sum_{m=1}^{4} L_m(\xi_{FE}, \eta_{FE}) Y_m^j. \tag{3.20}$$

Equations 3.19 and 3.20 form a nonlinear system of equations that can be numerically solved for $\xi_{FE}$ and $\eta_{FE}$, using MATLAB's *fsolve()* function. With the eigenfunction values at FE nodes, equation 3.14 can be used to generate $\theta$ Random Fields at FE nodes, by sampling values of $\xi_i(\theta)$ from the standard normal distribution (bell curve with mean 0 and standard deviation 1). More details on the sampling process are given at the end of this section.

To obtain the RF values at FE gaussian points, an equivalent shape function interpolation is used, shown in equation 3.21, where $w_m^j$ represents the RF values at node m of FE element j and $nnod_{FE}$ is the number of nodes per FE element.

$$w_G(\xi, \eta) = \sum_{m=1}^{nnod_{FE}} L_m(\xi_G, \eta_G) w_m^j \tag{3.21}$$

Besides the RF values, the coordinates of the FE integration points can be obtained with equation 3.3. In summary, the RF to FE mapping procedure has the following steps:

- Using function *inpolygon*, go through every RF element and find the FE nodes inside or at its border.
- Remove multiple instances of the same FE nodes.
- Solve system of equations 3.19 and 3.20 for each FE node coordinate in the isoparametric space of their corresponding RF element.
- Using equation 3.1, find eigenfunction values at FE nodes.
- Using equation 3.21, calculate RF values at integration points.

An example of the separate RF and FE meshes, as well as of the FE gaussian points, where the RF values must be obtained, is shown in figure 3.2.

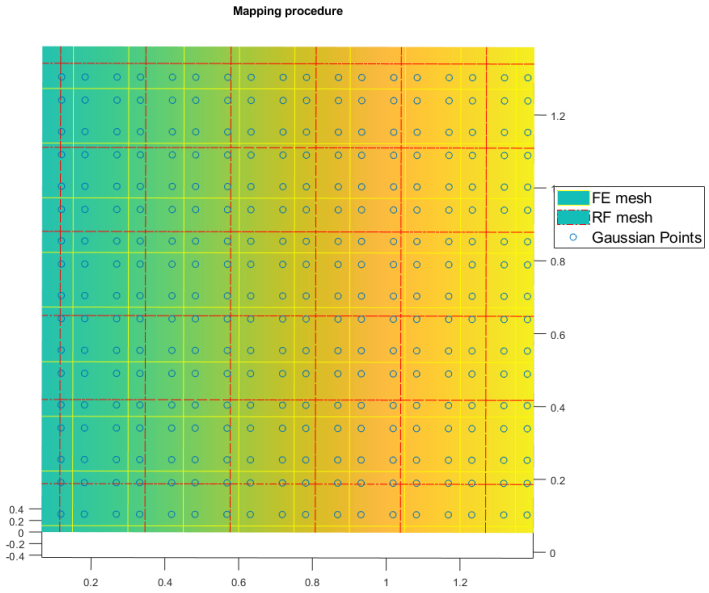


**Figure 3.2:** Mapping procedure - separate RF and FE meshes and final (gaussian) interpolation points.

### Meshing

One of the disadvantages of the galerkin procedure is the need to create an RF mesh, which can be difficult for non-trivial geometries. Another option is to use the same mesh for both RF discretization and FEA, which though simple can be unnecessarily expensive on the computational side, since the FE mesh often requires more elements.

In the developed code, a mesh created on abaqus can be read through a .inp file and be used for the RF/FE. As mentioned before, the RF mesh was limited to linear quadrilateral elements, since this was found to give satisfactory results. The FE mesh is limited to linear full integration 4-node elements or quadratic 8-node elements (on abaqus, S4 and CPS8, for example). However, especially for the FE mesh, little adaptation is required to allow the possibility of other types of elements, with different numbers of nodes or reduced integration.

The Abaqus option is the simplest, but makes iterating on the number of elements to find convergence much more tedious. The other option is to develop a mesh creating process that can be easily iterated on, adapted to the specific geometry. For example, regarding the open-hole case, a mesh can be created that discretizes around a hole in the radial and tangential directions[1]. Then, the number of elements can be iterated on by increasing the number of elements in each of those directions. An example of the use of such a mesh in the galerkin procedure is given in figure 3.3.

[1]KSSV (2024). Mesh a plate with hole (https://www.mathworks.com/matlabcentral/fileexchange/44670-mesh-a-plate-with-hole), MATLAB Central File Exchange. Retrieved May 24, 2024.

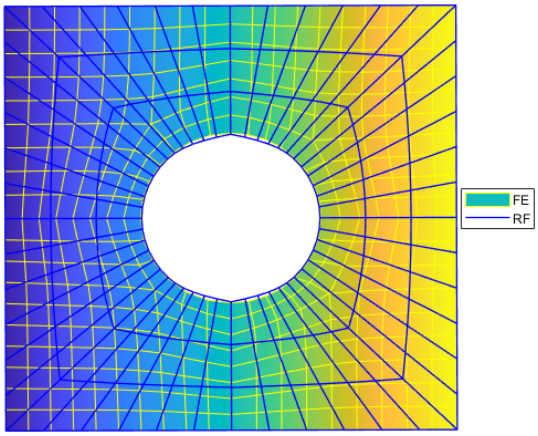


**Figure 3.3:** Mesh for 1 by 1 open-hole plate with hole diameter of 0.4.

For any geometry, any RF meshing procedure can be used, as long as it defined by its nodal coordinates and a connectivity matrix, similarly to what is done in FE software.

**Sampling**

For the same material property, a Random Field is generated for each simulation and ply of the laminate being analyzed, so that response statistics can be gathered. The randomness of each random field comes from the variables $\xi_i(\theta)$ in equation 3.14.

To obtain standard normal variables $\xi_i(\theta)$, Latin Hypercube Sampling is used. In section 2.2.3, the difference between LHS and random MC was explained, and exemplified in figure 2.9. The cumulative distribution function of the standard normal variables is divided in $N_\theta$ intervals, $N_\theta$ being the number of simulations to be run, or number of RFs generated of the same material property, for the same ply. Similarly to what was exemplified for the 2D case (figure 2.9), the samples of each variable are shuffled to satisfy the latin hypercube requirements (no column or line is sampled from twice), except the problem now has M dimensions (number of random variables $\xi_i(\theta)$).

This sampling procedure both preserves the marginal probability distributions [56], and is more efficient than random MCS. This is shown in figure 3.4, which shows the convergence of the standard deviation and mean of a set of samples of the standard normal variable. For the MC, each sample is random, while for each number of samples (x axis) the LHS calculates a new evenly distributed set of samples. The convergence can be observed to be much faster in the LHS case, for both statistical moments.

## 3.2. Applying the Karhunen-Loève - Bounding Box

A simpler method, recently suggested in [86], is to find a rectangular domain that bounds the 2D FE mesh where the Random Fields are to be generated. For this rectangular domain, the analytical solution of the Fredholm integral 2.15, with the covariance function introduced in 3.13, is known. Then the eigenfunction values at the integration points can be directly calculated and a Random Field in the FE mesh is ”cut-out” from the bounding domain.

The first step in this approach is to find the ”bounding box”. Similarly to how the RF ones were defined in 3.12, but adding an extra term d, the dimensions of the bounding box are given by

$$L_{D1} = (x_{maxFE} + d) - (x_{minFE} - d) \tag{3.22}$$

and

$$L_{D2} = (y_{maxFE} + d) - (y_{minFE} - d), \tag{3.23}$$

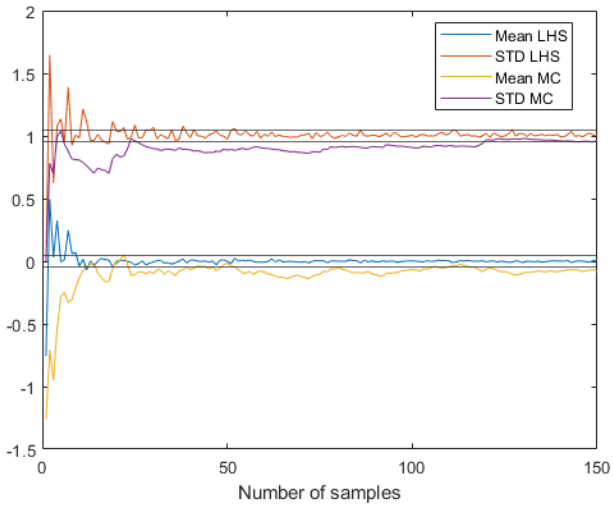


**Figure 3.4:** Convergence of mean and standard deviation of samples of the standard normal variable, for LHS and random MCS. Lines represent means of -0.05 and 0.05, as well as standard deviations of 0.95 and 1.05.

where the x and y terms represent the minimum and maximum coordinates of FE nodes in both directions and d is the distance between the box edges and the FE mesh edges. This distance is given as a ratio $d_r$ to the biggest mesh dimension, such that

$$d = d_r * L_{D1}. \tag{3.24}$$

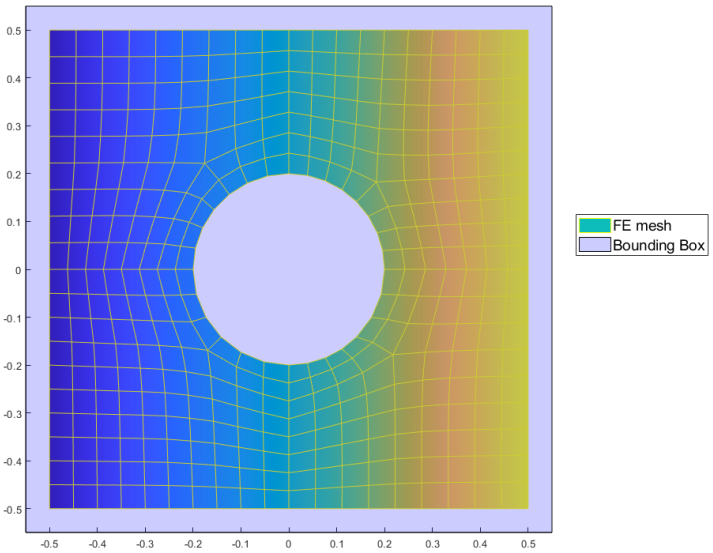


**Figure 3.5:** Bounding box with $d_r$=0.05 around a 1 by 1 FE mesh with a 0.4 diameter hole.

An example of a bounding box around a 1 by 1 FE mesh with a 0.4 diameter hole is shown in figure 3.5. The analytical solution over the rectangular domain is obtained from the separate 1D solutions for each direction x ad y. If the 2D eigenvalues and functions are assumed to be

$$\phi_n(\boldsymbol{x}) = \phi_i^{(1)}(x)\phi_j^{(1)}(y) \tag{3.25}$$

and

$$\lambda_n = \lambda_i^{(1)} \lambda_j^{(1)}, \tag{3.26}$$

the Fredholm integral separates into two separate ones:

$$\int_{x_{minFE}-d}^{x_{maxFE}+d} \exp(-\frac{|x_1 - x_2|}{b_{cX} L_{D1}}) \phi_i^{(1)}(x_2)\, dx_2 = \lambda_i^{(1)} \phi_i^{(1)}(x_1) \tag{3.27}$$

and

$$\int_{y_{minFE}-d}^{y_{maxFE}+d} \exp(-\frac{|y_1 - y_2|}{b_{cY} L_{D2}}) \phi_j^{(2)}(y_2)\, dy_2 = \lambda_j^{(2)} \phi_j^{(2)}(y_1). \tag{3.28}$$

For the first equation, the following solution can be derived [63]:

$$\lambda_i^{(1)} = \frac{2L_{c1}}{(w_i^{(1)})^2 L_{c1}^2 + 1} \tag{3.29}$$

$$\phi_i^{(1)}(x) = \frac{\cos(w_i^{(1)}(x - c^{(1)}))}{\sqrt{a^{(1)} + \frac{\sin(2w_i^{(1)} a^{(1)})}{2w_i^{(1)}}}} \tag{3.30}$$

for i odd;

$$\phi_i^{(1)}(x) = \frac{\sin(w_i^{(1)}(x - c^{(1)}))}{\sqrt{a^{(1)} - \frac{\sin(2w_i^{(1)} a^{(1)})}{2w_i^{(1)}}}} \tag{3.31}$$

for i even, where

$$c^{(1)} = (x_{minFE} + x_{maxFE})/2, \tag{3.32}$$

$$a^{(1)} = L_{D1}/2, \tag{3.33}$$

and

$$L_{c1} = b_{cX} L_{D1}. \tag{3.34}$$

The value of $w_i^{(1)}$ is calculated by solving the transcendental equation

$$(\frac{1}{L_{c1}} - w_i^{(1)} tan(w_i^{(1)} a^{(1)}))(w_i^{(1)} + \frac{1}{L_{c1}} tan(w_i^{(1)} a^{(1)})), \tag{3.35}$$

for $\frac{(i-1)\pi}{2a} \leq w_i^{(1)} \leq \frac{i\pi}{2a}$, using MATLAB's *fzero()* function. The second equation has an analogous solution with the y coordinates. If T eigenfunctions and values are calculated for each axis, then $T \times T$ terms of the KL expansion can be obtained. To truncate the expansion at M terms, similarly to the galerkin procedure, at least $M \times M$ eigenvalues/functions are always calculated, and then organized in descending order. Finally, the $\xi_i(\theta)$ sampling procedure is equal to the one described in section 3.1, for the galerkin method, and the FE meshes can also be read can be read in the same way, from an Abaqus .inp file.

## 3.3. Comparing the methods

Eigenfunctions 1, 2, 3 and 6 of the covariance function, obtained with the galerkin and bounding box methods, are shown in figures 3.6 to 3.13, for a 1 by 1 square domain with $b_{cX} = b_{cY} = 1$, $d_r$=0 and a RF mesh with 100 elements. For such a case, the galerkin solution should converge to the bounding box one, since the analytical solution domain and FE domain are the same.

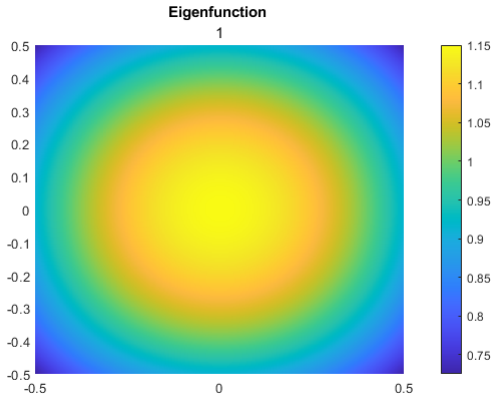


**Figure 3.6:** 1st analytical eigenfunction.

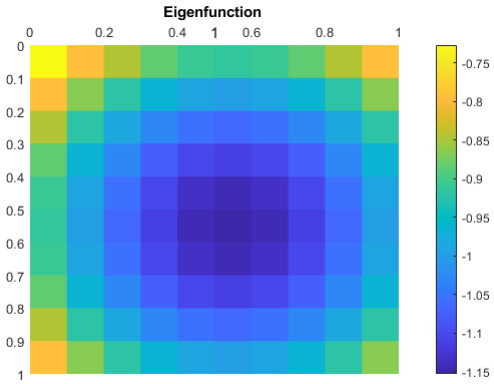


**Figure 3.7:** 1st galerkin eigenfunction.

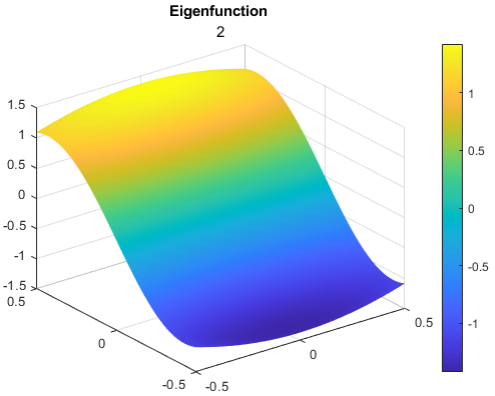


**Figure 3.8:** 2nd analytical eigenfunction.

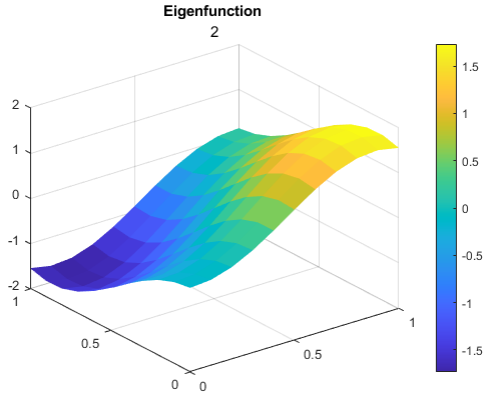


**Figure 3.9:** 2nd galerkin eigenfunction.

Eigenfunctions 1 and 6 are in fact very similar for both methods, while 2 and 3 are quite different. However the latter 2 are an eigenpair, meaning they correspond to the same eigenvalue. Note now that it can be written that the covariance of the truncated KL random field is given by

$$Cov[w(\mathbf{x}_1,\theta), w(\mathbf{x}_2,\theta)] = \sigma_w^2 C(\mathbf{x}_1,\mathbf{x}_2) = \sigma_w^2 \sum_{i=1}^{M} \lambda_i \phi_i(\mathbf{x}_1)\phi_i(\mathbf{x}_2), \tag{3.36}$$

the expression on the right being the truncated spectral decomposition of the covariance function (multiplied by the prescribed variance) [91]. Because eigenpairs have the same eigenvalue, the point-wise variance is not affected if the squared sum of the 2 eigenfunctions remains the same. If that calculations is done for eigenfunctions 2 and 3, for example, the result is the same in the analytical and galerkin case - this difference only slightly affects the covariance between different points, which can easily be adjusted with the correlation length.

Figure 3.14 shows the first 10 eigenvalues for this same case with a 25 element RF mesh and two different correlation parameters ($b_{cX}$ = $b_{cX}$ = 1 and $b_{cX}$ = $b_{cX}$ = 2). Two observations can be made of these results: again, the galerkin method matches the analytical one; for lower correlation parameters,

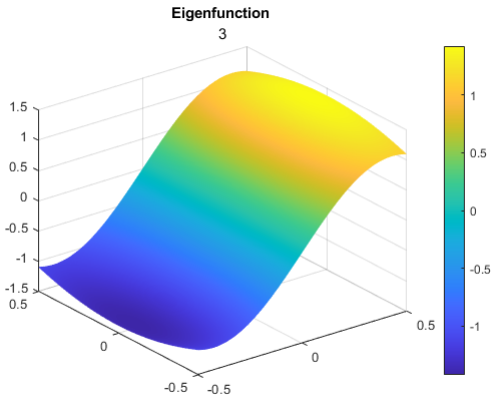


**Figure 3.10:** 3rd analytical eigenfunction.

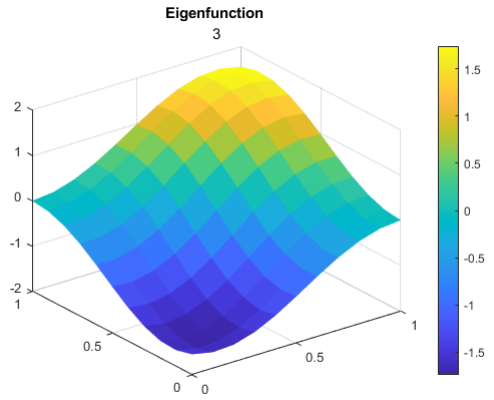


**Figure 3.11:** 3rd galerkin eigenfunction.

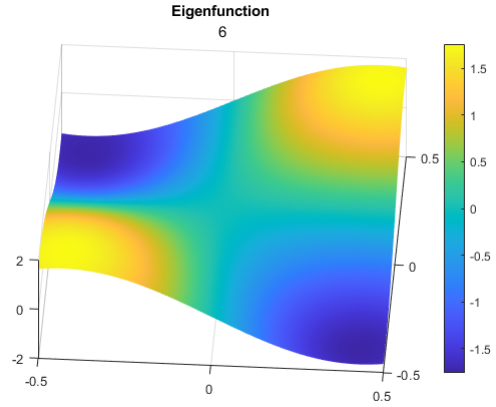


**Figure 3.12:** 6th analytical eigenfunction.

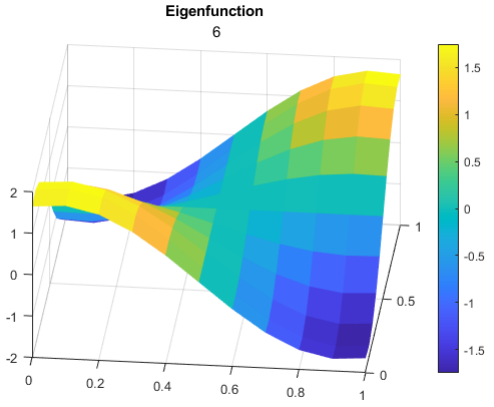


**Figure 3.13:** 6th galerkin eigenfunction.

the eigenvalues decrease slower, which means a higher truncation term will be necessary to achieve convergence.

The eigenfunctions help understand the KL expansion, as the RFs result from a linear combination of the product of them with the eigenvalue term. In the case of our covariance function, that we are prescribing to the fields, the correlation between two points decreases exponentially with the distance between them, with the speed of this decrease being adjusted to a ratio of the dimensions of the field. The eigenfunctions are then affected by the correlation parameters, maintaining their pattern but changing the ”amplitude” and ”frequency”. The eigenvalues in turn grow linearly with the domain, and are slightly affected by the correlation parameters.

While the galerkin mesh implies an approximation that is smaller for a finer RF mesh, both methods will have an error in representing the prescribed covariance function, which comes from truncating the KL expression - the generated RF variance will always be underestimated. The point-wise variance error is given by

$$\epsilon_{M,\sigma_w^2}(\boldsymbol{x}) = \frac{\sigma_w^2 - Var[w(\boldsymbol{x},\theta)]}{\sigma_w^2}, \tag{3.37}$$

which using equation 3.36 can be rewritten as

$$\epsilon_{M,\sigma_w^2}(\boldsymbol{x}) = 1 - \frac{\sum_{i=1}^{M} \sigma_i \phi_i^2(\boldsymbol{x})}{\sigma_w^2}. \tag{3.38}$$

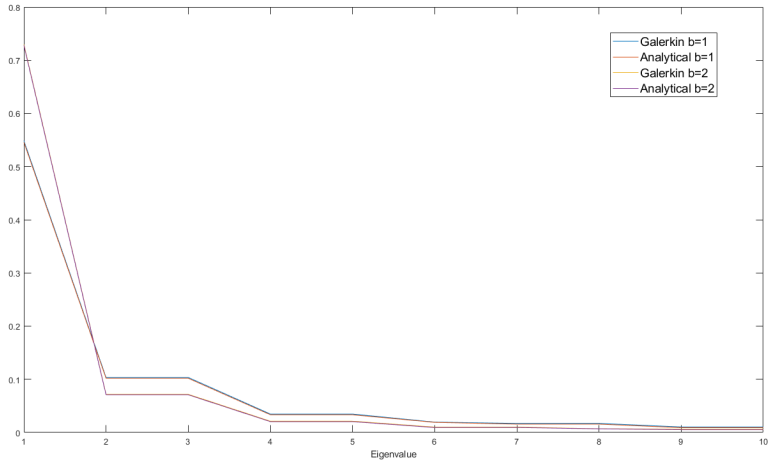


**Figure 3.14:** Eigenvalues for 1 by 1 domain obtained with the analytical solution and the galerkin (25 element RF mesh) solution, for $b_{cX}$ = $b_{cX}$ = 1 and $b_{cX}$ = $b_{cX}$ = 2.

This relative error estimator will be referred to as the local variance error, as it is different at different points of the domain. In [91], a global estimator is also introduced, with the form

$$\bar{\epsilon}_{M,\sigma_w^2} = \frac{1}{A_D}\int_D \epsilon_{M,\sigma_w^2}(x)dx, \tag{3.39}$$

which using equation 3.17 becomes

$$\bar{\epsilon}_{M,\sigma_w^2} = 1 - \frac{\sum_{i=1}^{M}\lambda_i}{A_D\sigma_w^2}. \tag{3.40}$$

This global error estimator is useful for a general accuracy assessment, since the local one might change significantly from one point of the domain to another. However, equation 3.17 can be used only if the condition of orthonormality is fulfilled. That doesn't happen with the bounding box method in any case where the solution domain is different than the bounding box. Therefore, the global error estimator for the bounding box method is

$$\bar{\epsilon}_{M,\sigma_w^2} = \frac{1}{n}\sum_{i=1}^{n}\epsilon_{M,\sigma_w^2}(x), \tag{3.41}$$

which is more tedious to compute and results from spatially averaging the local error (using the FE node values).

To compare the accuracy and efficiency of the methods described in sections 3.1 and 3.2, the example of a 1 by 1 square mesh, with a 0.4 diameter hole, of linear Q4 elements will be taken. Considering a constant (throughout the field) point-wise variance $\sigma_w^2$ of 1 and 0 mean, and an intended spatial standard deviation $\sigma_s$ of 0.5, both methods will be compared in terms of the error corresponding to these values, as well as in their efficiency. The FE mesh that will be used can be seen in figures 3.3 and 3.5, with 355 elements, along with the 144 element RF mesh that will be used. The bounding box for the comparison will have $d_r$=0.

A study of the effect of the correlation parameters on both methods was first done, and the values of $b_{cX} = b_{cY}$ were set to the ones that minimized the relative error of the spatial standard deviation $\sigma_s$, for which the target is 0.5. It is important to mention here that this relation between $\sigma_s$ and the correlation parameters can only be maintained if the integration points, for which the standard deviation

is calculated, are evenly distributed throughout the domain. If the mesh density is higher in one area in some cases, the standard deviation will no longer refer to the same domain as the target one. The relative error is calculated with

$$\epsilon_{\sigma_s} = 1 - \frac{\frac{1}{n}\sum_{i=1}^{n}\sigma_s(\theta)}{\sigma_s}, \tag{3.42}$$

which is the average of the standard deviations of each RF after n random cases were generated. Values of b were considered in steps of 0.05, with a number of KL expansion terms that guaranteed a global point-wise error smaller than 5%. Consequently, the correlation parameter is 1.7 for the galerkin method, and 1.95 for the bounding box method. The evolution of $\sigma_s$ with n for these correlation values and corresponding methods is shown in figures 3.15 and 3.16, up until n=30000.

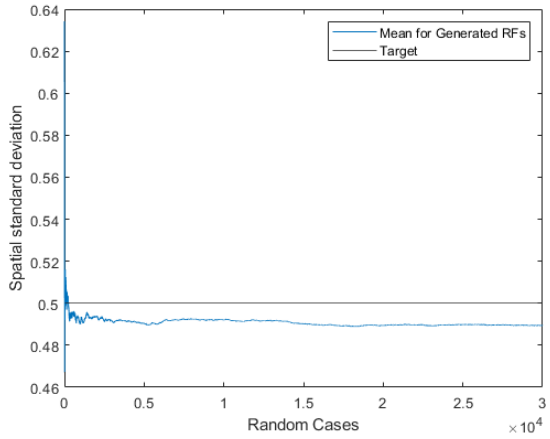


**Figure 3.15:** Standard deviation (average of values at each RF) obtained with galerkin method (b=1.7, 40KL terms) vs 0.5 target.

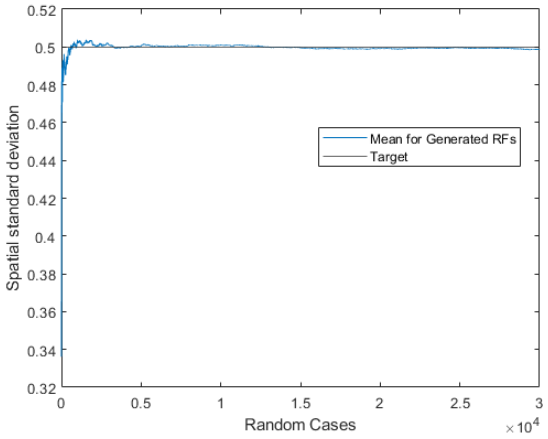


**Figure 3.16:** Standard deviation (average of values at each RF) obtained with bounding box method (b=1.95, 40KL terms) vs 0.5 target.

The figures show how the spatial standard deviation quickly converges for both methods, to values close to the target ($\epsilon_{\sigma_s}$ is 2% for galerkin and 0.2% for bounding box). Better approximations can be obtained with smaller changes of $b$ in the convergence study, around the chosen values. Therefore, the main conclusion is that with both methods very good approximations of a chosen standard deviation can be obtained, after a few hundred random cases. However, this convergence study is facilitated in the bounding box method, because it runs each iteration considerably (up to 10x times) faster than the galerkin method.

Figure 3.17 shows the global error with the first 40 KL terms for each of the solutions, where the error parameter is calculated for galerkin and bounding box with expressions 3.40 and 3.41, respectively. For both solutions, the error becomes smaller than 5% for around 14 KL terms, and they both converge to about 2%.

Figures 3.18 and 3.19 show the local variance error throughout the domain for the galerkin and bounding box solutions, respectively, using 40 KL expansion terms.

While the galerkin solution has peaks at edges of the domain, which include the outer box and the circle that limits the hole, the bounding box has similar peaks just at the outer box, since this is where the analytical solution was obtained. Additionally, the bounding box has the advantage of using the $d$ parameter, which so far has been set to 0. If it is increased, those peaks at the limits will be outside the solution domain, and the local error peaks can be avoided. Figure 3.20 shows the local error with $d = 0.04$. Increasing it by a small value like this does not change the global error significantly, but allows the local peaks to be much smaller - increasing d by very high values, though, will cause slower decay of eigenvalues (and slower variance convergence) [86].

The local error was studied in more detail at an arbitrary gaussian point (x=-0.045 y=-0.328), to confirm the accuracy suggested by the error parameter, with 40 KL expansion terms and d=0. Figures 3.21 to

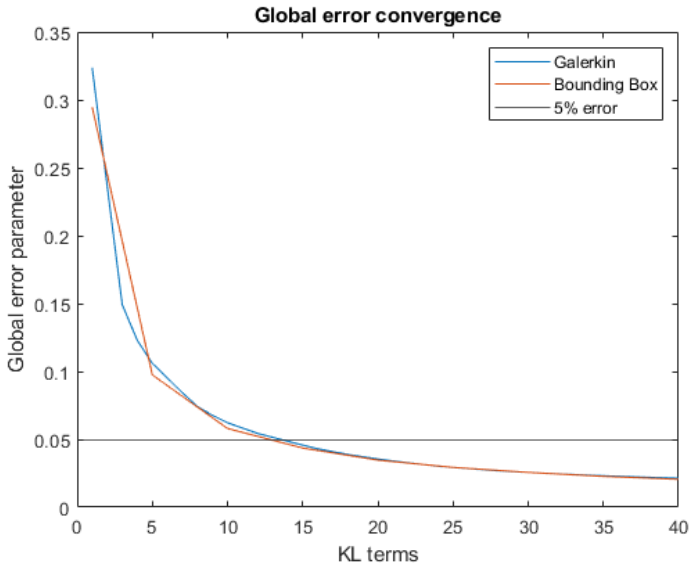


**Figure 3.17:** Global error evolution with increase of KL terms, for Galerkin and Bounding Box solutions

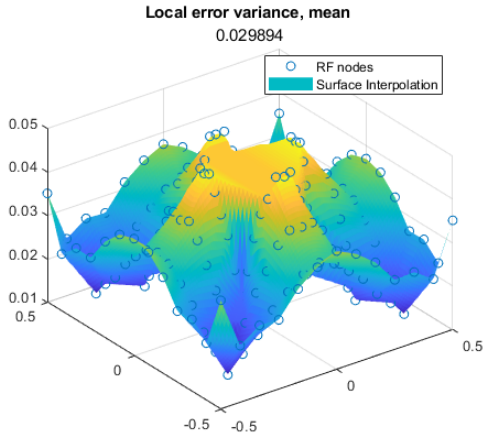


**Figure 3.18:** Local variance error with galerkin method.

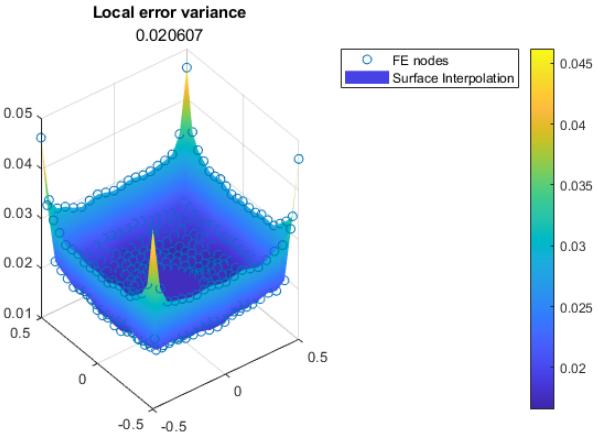


**Figure 3.19:** Local variance error with bounding box method.

3.24 show the histograms and fitted normal distributions (*fitdist* in MATLAB) for the values at this point in 30000 generated Random Fields $w((x = -0.045, y = -0,328), \theta)$, with the galerkin and bounding box methods. The CDFs are compared to the target normal distribution, which is the standard one (mean 0 and variance 1).

It is apparent that the intended distribution is very well approximated at each point, while the RFs globally are changed to achieve different spatial standard deviations. The plots agree with the very low ($\approx 3\%$) error in the representation of the prescribed covariance function, and no significant advantage exists for either method in this aspect.

Figures 3.25 and 3.26 repeat the analysis of figure 3.4 for the convergence of the prescribed point-wise standard deviation and mean. The standard deviation and mean of sampled values at point x=-0.045 y=-0.328 are plotted. The targets are the values to which they are expected to converge, considering the truncation error in the case of the standard deviation.

Again, it was observed that the LHS leads to a faster convergence of the mean to the target 0. Here the standard deviation does not seem to have such a difference. Nevertheless, there is an advantage in using the LHS when compared to MCS. Furthermore, this study is useful to know that the prescribed

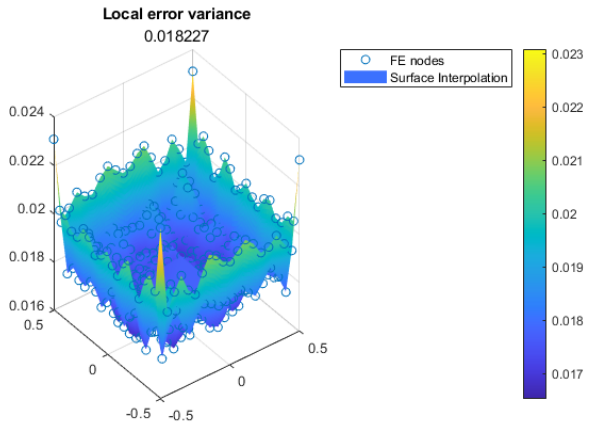


**Figure 3.20:** Local error with bounding box method and d=0.04.

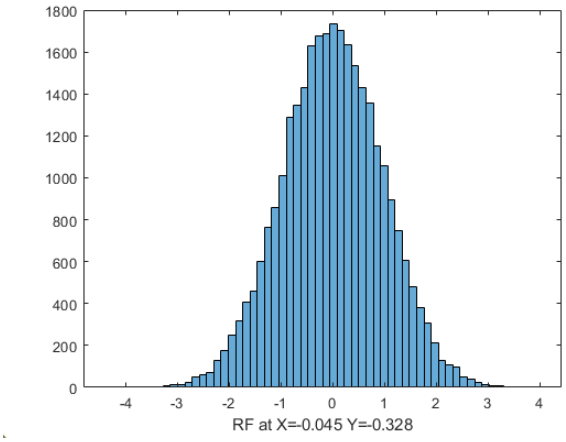


**Figure 3.21:** Histogram of 30000 samples at x=-0.045 y=-0.328, obtained with the Galerkin method.

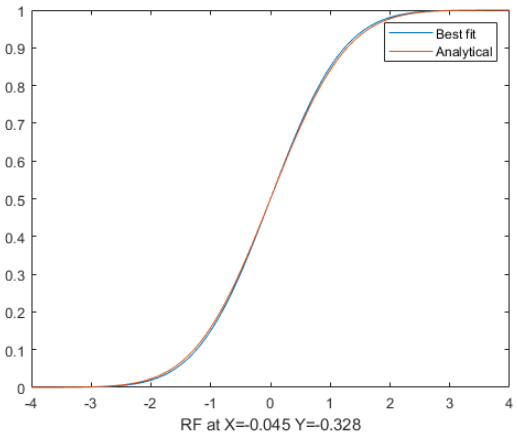


**Figure 3.22:** Fitted normal CDF of 30000 samples at x=-0.045 y=-0.328, obtained with the Galerkin method vs standard normal distribution CDF.

covariance is already well approximated at each point for about 200 samples, for either method.

To finalize the comparison of the Galerkin and the bounding box methods, 1000 Random Fields were generated with each method, for 14 properties (representative of the 14 properties that will be random in the analysis) of every ply of a 16-ply laminate. The number of KL terms was 40 and all other inputs remained the same as throughout the present section. Figures 3.27 and 3.28 show an example of an RF generated with each method.

Generating all random fields was about 8 times faster for the bounding box. In this case, however, the advantage is not very significant since both methods were fast, especially when compared to the computational time that the rest of the SFEM process will demand. When looking for convergence though, where the more computationally expensive parts of the galerkin method must be repeated, like solving the non-linear equations, the speed of the analytical solution can be a relevant. This is also true for models with a very large number of plies or integration points.

## 3.4. Using non-Gaussian probability distributions

The KL expansion as represented in equation 2.10 is based on generating random fields of normal variables, with the randomness in the expression coming from the standard gaussian variables $\xi_i$. The formulation of the expansion that has been presented is the simplest and more common one, and is used to discretize gaussian processes [93].

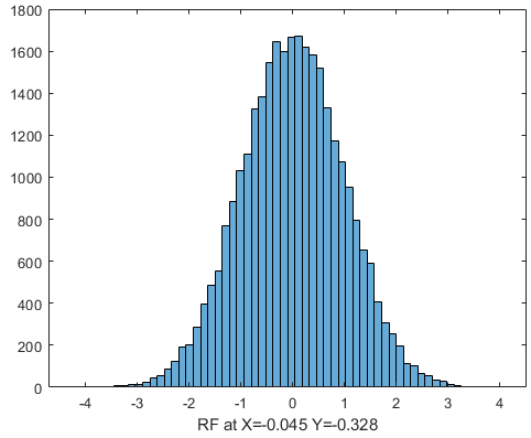


**Figure 3.23:** Histogram of 30000 samples at x=-0.045 y=-0.328, obtained with the Bounding Box method.

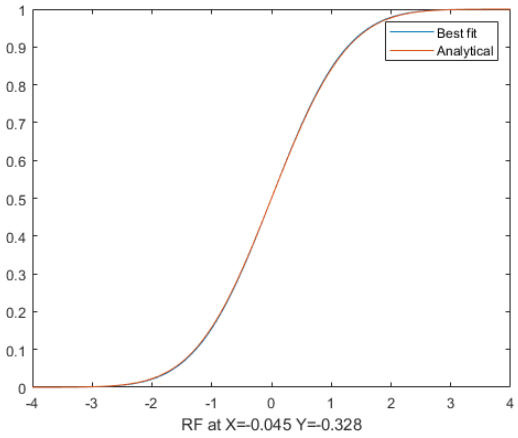


**Figure 3.24:** Fitted normal CDF of 30000 samples at x=-0.045 y=-0.328, obtained with the Bounding Box method vs standard normal distribution CDF.

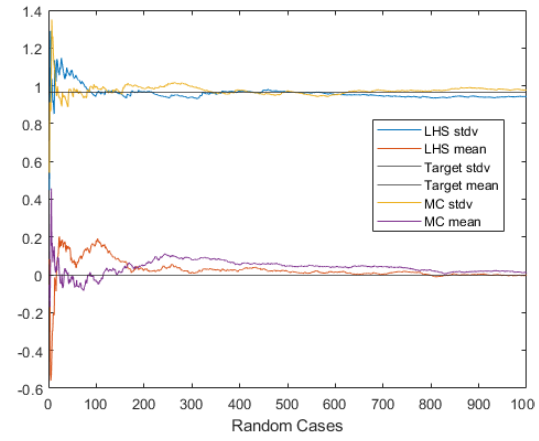


**Figure 3.25:** Convergence with galerkin method of standard deviation and mean of values at x=-0.045 y=-0.328 obtained with MC sampling and Latin Hypercube sampling vs targets.

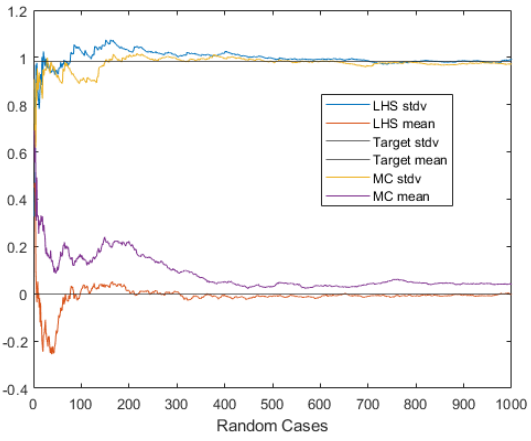


**Figure 3.26:** Convergence with bounding box method of standard deviation and mean of values at x=-0.045 y=-0.328 obtained with MC sampling and Latin Hypercube sampling vs targets.

However, it is often much more convenient to use non-gaussian probability distributions to represent random processes of interest. One such case is when working with physical parameters that are always positive - the gaussian CDF always includes a ”negative tail”. That problem must be addressed in this project, since material properties such as Young’s Modulus and tensile or compressive strength are defined as positive, and finite elements cannot be correctly modelled with negative values for those variables. Additionally, some material properties may be better represented by non-gaussian distributions, such as weibull or log-normal.

In [93], a method is explained that can be used to, with small adjustments, use the same KL formulation with different original distributions. It works by utilizing the Nataf transform to calculate an equivalent gaussian covariance function, and then reverting back to the original distribution after the discretization. A table from that paper summarizing the adjustments for different processes is shown in figure 3.29. The expressions used for the final variable transformation, which include $\bar{y}$ and $\sigma_y$, can be found in [93].

The eigenvalues and functions of equation 2.10 can be calculated in the same way for the galerkin solution, with equation 3.7 changing so that the covariance function is the KL Kernel $\rho_g$ of figure 3.29. The mean $\bar{y}$ is only added when the change of variable is reversed (and not when the normal RF is calculated with equation 2.10). For the bounding box solution, this approach is not possible, since that

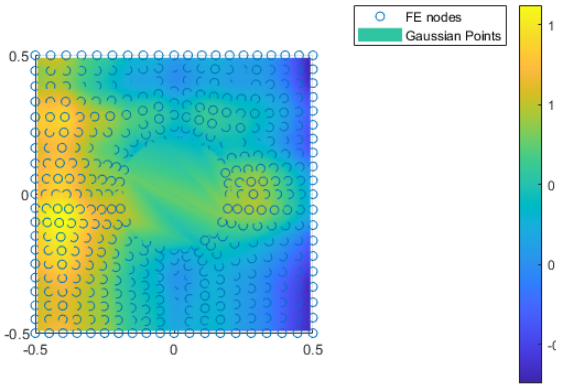


**Figure 3.27:** Random Field generated with the galerkin method (40 KL terms, b=1.7)

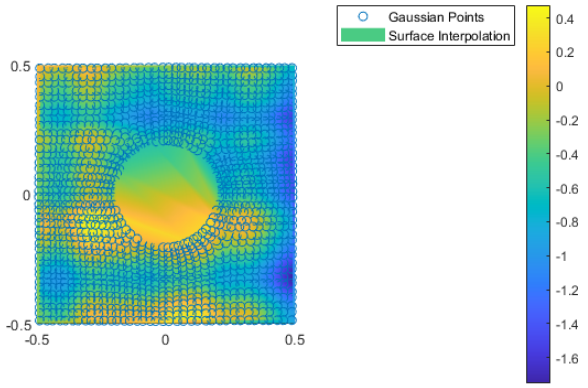


**Figure 3.28:** Random Field generated with the bounding box method (40 KL terms, b=1.95)

| Type | Mean $\bar{y}$ | Variance $\sigma_y^2$ | K–L kernel $\rho_G$ |
|---|---|---|---|
| Uniform | $(a+b)/2$ | $(b-a)^2/12$ | $2\sin(\pi\rho_y/6)$ |
| Step | 0 | 1 | $\sin(\pi\rho_y/2)$ |
| Triangular | $b/2$ | $b^2/24$ | $\rho_y = \sum_{n=1}^{N} \widetilde{K}_{T,n}^2 \rho_G^n$ |
| Rayleigh | $b\sqrt{\pi/2}$ | $(4-\pi)b^2/2$ | $\rho_y = \frac{2}{4-\pi} \sum_{n=1}^{N} \widetilde{K}_{R,n}^2 \rho_G^n$ |
| Exponential | $1/\lambda$ | $1/\lambda^2$ | $\rho_y = \sum_{n=1}^{N} K_{E,n}^2 \rho_G^n$ |
| Log-normal | $y_0 e^{\widehat{\sigma}^2/2}$ | $\bar{y}^2(e^{\widehat{\sigma}^2}-1)$ | $\rho_y(e^{\widehat{\sigma}^2}-1) = e^{\widehat{\sigma}^2 \rho_G} - 1$ |
| Log-uniform | $\frac{\beta-\alpha}{\ln(\beta/\alpha)}$ | $\frac{\beta^2-\alpha^2}{2\ln(\beta/\alpha)} - \bar{y}^2$ | $\rho_y = \sum_{n=1}^{N} \widetilde{K}_{LU,n}^2 \rho_G^n$ |

**Figure 3.29:** Summary of expressions to be used for parameters and the covariance function when using the Nataf transform approach [93].

formulation uses the analytical solution of the covariance function shown in equation 3.11. Figures 3.30 and 3.31 show the histogram and best fit of 30000 generated random field values at an aforementioned random mesh point already used in figures 3.21 and 3.23, with the original variable modeled as a Rayleigh function with $b = \sqrt{2}/(4-\pi)$. Note that, after generating the random field values, they are transformed back from the gaussian generated ones with the expression

$$w(\mathbf{x},\theta) = \bar{y} + (\sqrt{2\ln\frac{2}{1-erf(\sigma_y w_N(\mathbf{x},\theta)/\sqrt{2})}} - \sqrt{\pi/2})b, \tag{3.43}$$

where $\sigma_y$ and $\bar{y}$ are calculated as shown in the table of figure 3.29. The KL kernel was calculated by finding the root of the equation in the last column of the table, with 5 terms of the sum. The obtained distribution matches the analytical one, very closely. This could be further improved by utilizing more terms in the covariance calculation, although at some computational cost.

The log-normal distribution is particularly useful to avoid negative values of material properties in structural analysis, and that correction is used in [56]. Such a distribution is given by

$$X = e^{\mu+\sigma Z}. \tag{3.44}$$

with Z being the standard normal variable. In the approach used in that paper, the input log-normal distributions are given by their actual mean and variance, $\mu_L$ and $\sigma_L$, and then the log-normal parameters $\sigma$ and $\mu$, which coincide with those of the normal distribution given by $\ln(X)$, are calculated with

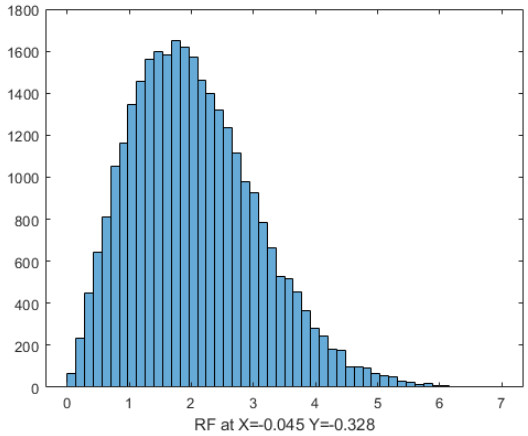


**Figure 3.30:** Histogram of 30000 samples at x=-0.045, y-0.328, obtained with the galerkin method and a rayleigh input variable ($b = \sqrt{2}/(4-\pi)$).

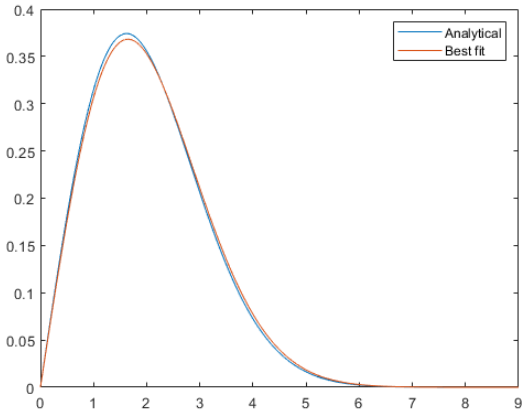


**Figure 3.31:** Fitted rayleigh PDF of 30000 samples at x=0.045, y=-0.328, obtained with the galerkin method vs analytical PDF with $b = \sqrt{2}/(4-\pi)$.

$$\sigma = \sqrt{\ln(\frac{{\sigma_L}^2}{\mu_L} + 1)} \tag{3.45}$$

and

$$\mu = \ln \mu_L - \frac{1}{2}\sigma^2. \tag{3.46}$$

After the values of the RF are calculated in the standard way, the change of variable is reversed with

$$w(\boldsymbol{x}, \theta) = exp(w_N(\boldsymbol{x}, \theta)). \tag{3.47}$$

In this almost equivalent approach, the covariance function is not adjusted, which means it can be implemented with the bounding box solution. In [56], the reasoning for this was that the coefficients of variations used were small, and so the lack of correction was found to not significantly distort the correlation structure.

Figures 3.32 and 3.33 show the histogram and fitted distribution of 30000 generated samples with the bounding box method, at a random point already chosen for figures 3.21 and 3.23, with the original distribution being log-normal with mean 2 and standard deviation 1. The fitted distribution matches the analytical one exactly, which shows the simplified adjustment works as intended.

## 3.5. Conclusions and Limitations

In sections 3.1 and 3.2, two methods of applying the Karhunen-Loève expansion to discretize random fields of values at the integration points of a generic FE mesh were presented. In section 3.4, this methodology was expanded to include the possibility of non-gaussian Random Fields.

In section 3.3, the Galerkin solution, which is the norm in literature, and bounding box solution were compared based on error parameters and computational efficiency. It was found that the latter has three main advantages: it is much simpler and doesn't require generating an RF mesh, for which a convergence study would be necessary; it can be adapted to limit peaks in local error, by extending the bounding box; it is much faster. In terms of global errors in the mean, point-wise variance and spatial standard deviation of the fields, both methods can generally achieve equally adequate results.

The analytical method disadvantages are that it is limited to the chosen covariance function, for which an analytical solution exists, and that for geometries that occupy a small portion of the bounding box

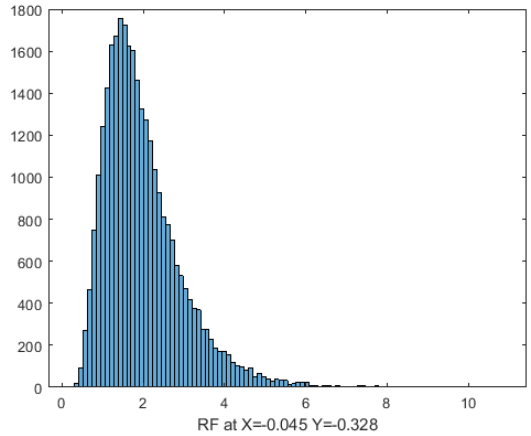


**Figure 3.32:** Histogram of 30000 samples at x=-0.045 y=-0.328, obtained with bounding box method and log-normal input variable (mean 2 and standard deviation 1).

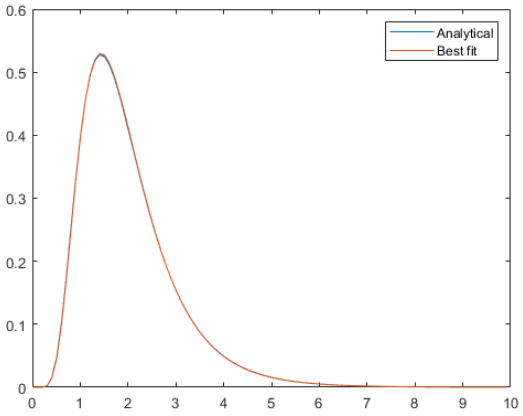


**Figure 3.33:** Fitted log-normal PDF of 30000 samples at x=0.045, y=-0.328, obtained with the bounding box method vs analytical PDF with mean 2 and standard deviation 1.

it may be difficult to control the spatial standard deviation with the $b$ parameters. Additionally, it is also limited to the use of lognormal or normal distributions, since this covariance function cannot be altered.

Nevertheless, for most cases in composite laminate applications, where the presented covariance function is applicable and the geometry occupies a big portion of its bounding box, which includes the case studies of this thesis, the bounding box solution's advantages seem to outweigh the cons. Therefore, this is the chosen method for the validation examples that will be presented.

To allow maintaining physical, strictly positive values of variables, and avoid adjustments to the kernel or covariance function, the same "low coefficients of variation" assumption from [56] is made for this project, since although the variance may sometimes be higher than that $10\%$ of the mean threshold defined in that study, the log-normal correction is not expected to require the covariance function adjustment.

Only the log-normal distribution will be used to represent the random variables in the stochastic analysis performed in the following sections. Other distributions would require more complex adjustments, and limit the use of the bounding box solution, which has shown otherwise to be the preferable option. It is recognized that this is a limitation of this work, but with log-normal distributions having shown great results in modelling random material properties [5], the effect is not expected to be significant.

Finally, the LHS and MC sampling methods were compared in 3.3, in the context of the KL expansion, and it was shown that the mean of the discretized variable converges significantly faster with LHS.

# 4

# Stochastic Finite Element Method

This section details the proposed SFEM methodology of the present study. In section 2.1.2, the deterministic FEM, which is a CDM, is described. Then, in section 4.2, the inputs of the SFEM are listed, and possible ways to obtain them are addressed. In section 4.3, a workflow diagram (figure 4.2) representing the developed framework is presented, and each step of the methodology is outlined and discussed. Finally, section 4.4 covers the main conclusions and points of the present chapter.

## 4.1. Continuum Damage Model

This section outlines the finite element model developed in FE software Abaqus, that will be used for validation of this project's proposed stochastic method in section 5. The model uses a UMAT (User Defined Material) subroutine based on a model developed in [8], referred to as DM1 in that work. Out of the three presented by van Dongen et al., DM1, as a continuum damage model, was the simplest one, and its failure predictions were as accurate or more than the other ones presented in their report; those had the added complexity of using cohesive zones for delamination modelling (DM2) and XFEM in the matrix damage propagation phase (DM3).

The reason this model was chosen as a base is then that it is a good compromise between simplicity, computational efficiency and accuracy. First of all, the CDM approach is chosen because, for case studies where delaminations are not predominant, it should be able to give good predictions of failure and, with state-of-the-art criteria, of the initation and propagation of the different types of damage.

More complex techniques, mainly for delamination modelling, such as cohesive zones, and fracture mechanics based matrix cracking (like XFEM), were also considered. Cohesive Zone modelling does not, as was mentioned, necessarily improve failure predictions when compared with CDM, and that is especially true in cases where delaminations are not the predominant failure mode. However, applying the XFEM would likely allow even for these cases a more accurate prediction of damage patterns.

Nevertheless, with the amount of simulations involved in SFEM, this would come at too high of a computational cost, as analysis with XFEM is significantly slower. Additionally, convergence issues are much more problematic in that type of modelling, which would also pose an issue when running the same model recurrently (with different properties) for statistical purposes.

Considering then only CDMs, the Larc05 criterion [94] is chosen for damage initiation, and a bilinear softening constitutive model, as per the work of Lapczyk et al. [95], is chosen to regulate its propagation. The main reason for the choice is that this combination was the best performing overall out of three CDM models in [96]. Furthermore, Larc05 is considered the state-of-the-art of composite failure criterion, and bilinear degradation, as a gradual MDM, is expected to give more realistic predictions that sudden degradation methods, where material properties are deteriorated almost fully as soon as failure is predicted.

The CDM is implemented in a UMAT subroutine. This type of subroutine defines the whole material

behaviour, calculating the stress at each increment instead of the abaqus solver. The general advantage of using a subroutine, when compared to the options directly available in the Abaqus software, is that any failure-dependent criteria and MDM formulations can easily be implemented, whereas the latter offers very limited options. There are two criteria available in Abaqus: Hashin, which can only be selected for shell elements, and Larc05, for which element degradation can only be used when XFEM is also activated. With a subroutine, state-of-the-art criterion can be used without these constraints. Additionally, factors such as shear non-linearity and in-situ strengths are more easily controlled.

In this section, the Continuum Damage Model is detailed, in terms of its damage initiation criterion (section 4.1.1) and MDM (section 4.1.2), as well as additional numerical considerations (section 4.1.3). The UMAT subroutine, adapted from the one developed for [8], is detailed in appendix C, in terms of its working steps.

### 4.1.1. Initiation Criteria

The Larc05 criterion, proposed in [94], is considered by many the state-of-the-art when it comes to failure criteria for FRPs. With the same Abaqus subroutine that will be used for this project, it was combined by van Dongen [8] with a bilinear degradation MDM, and that CDM led to the best results in modelling of open-hole specimen. Also, as was mentioned in section 2.1, that family of criteria has received plenty of attention in current literature and obtained excellent results in the Worldwide Failure Exercise editions.

The criterion differentiates between 4 different failure modes: matrix cracking, fiber kinking, fiber splitting, and fiber tension.

1. Matrix Cracking

   This mode is given by the expression

$$FI_M = (\frac{\tau_T}{S_{23} - \eta^T \sigma_n})^2 + (\frac{\tau_L}{S_{12} - \eta^L \sigma_n})^2 + (\frac{\langle \sigma_n \rangle^+}{Y_T})^2, \tag{4.1}$$

   where

$$\sigma_n(\alpha) = \frac{\sigma_2 + \sigma_3}{2} + \frac{\sigma_2 - \sigma_3}{2} \cos 2\alpha + \tau_{23} \sin 2\alpha, \tag{4.2}$$

$$\tau_T = \frac{\sigma_3 - \sigma_2}{2} \sin 2\alpha + \tau_{23} \cos 2\alpha \tag{4.3}$$

   and

$$\tau_L = \tau_{12} \cos \alpha + \tau_{13} \sin \alpha. \tag{4.4}$$

   .

   Equation 4.1 is meant to be used for both tension and compression, with $\langle \sigma_n \rangle^+$ equal to 0 in the latter case (when $\sigma_n < 0$). As with Puck, there is a basis on the Mohr-Coulomb hypothesis, that fracture is only affected by stresses on the fracture plane. A value of $FI_M$ higher than 1 indicates failure. It depends on $\sigma_n$, $\tau_T$ and $\tau_L$, which are the stresses on the fracture plane - normal, transverse shear and longitudinal shear, respectively. Figure 4.1 illustrates the meaning of this fracture plane on a lamina.

   Those stresses depend on fracture angle $\alpha$, which is found in an iterative way such that $FI_M$ is maximized. Angles should be tested between 0° and 180°. For pure compression, fracture angle $\alpha_0$ can be obtained experimentally, and it has been found usually to be between 51° and 55 °[94].

   Friction coefficients $\eta^T$ and $\eta^L$ serve to adjust the shear strength to the existing pressure, increasing it in the case of compressive normal traction and decreasing for the tensile case. They are usually obtained as presented in [97]:

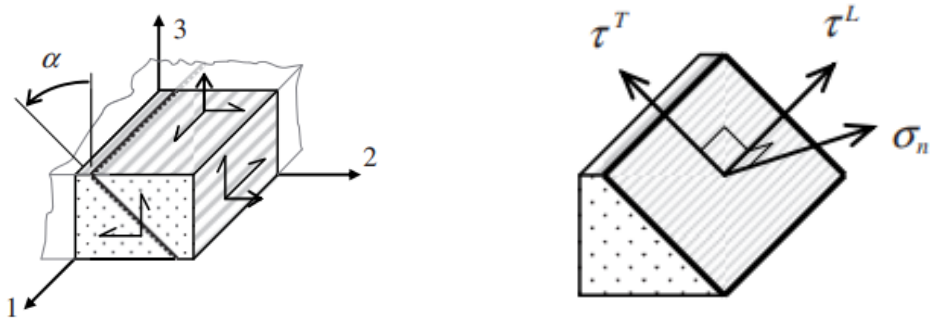


**Figure 4.1:** Fracture angle illustration [94].

$$\eta_T = -\frac{1}{\tan(2\alpha_0)} \tag{4.5}$$

and

$$\eta_L = -\frac{S_{12}\cos(2\alpha_0)}{Y_C\cos(\alpha_0)^2}. \tag{4.6}$$

.

Finally, $S_{23}$ is a difficult parameter to measure experimentally, and can be calculated [97] as

$$S_{23} = Y_C\cos(\alpha_0)(\sin(\alpha_0) - \eta^T\cos(\alpha_0)). \tag{4.7}$$

2. Fiber Kinking and Splitting

   The assumption is made that fiber kinking and splitting originate from shear-dominated ”localised matrix failure next to misaligned fibres” [94]. In the case of fiber kinking, longitudinal compression then leads to the formation of kink bands and fiber fracture, whereas splitting happens when this compression is less significant. Since these modes are not expected to be very significant in the case studies of section 5, for which the loading is uniaxial tension, the process of calculating this failure index is described in appendix B.

3. Fiber Tension

   The fiber tension criteria is simply

$$FI_{FT} = \frac{\langle\sigma_1^m\rangle^+}{X_T}. \tag{4.8}$$

### 4.1.2. Material Degradation Model

The model uses bilinear softening as a gradual MDM, proposed in [95]. The full compliance matrix is defined as

$$C = \begin{bmatrix} \frac{1}{(1-d_f)E_1} & -\frac{\nu_{21}}{E_2} & -\frac{\nu_{31}}{E_3} & & & \\ -\frac{\nu_{21}}{E_2} & \frac{1}{(1-d_m)E_2} & -\frac{\nu_{23}}{E_2} & & & \\ -\frac{\nu_{31}}{E_3} & -\frac{\nu_{23}}{E_2} & \frac{1}{(1-d_m)E_3} & & & \\ & & & \frac{1}{(1-d_m)G_{23}} & & \\ & & & & \frac{1}{(1-d_m)G_{12}} & \\ & & & & & \frac{1}{(1-d_m)EG_{13}} \end{bmatrix}. \tag{4.9}$$

Damage variables $d_f$ and $d_m$ represent fiber and matrix damage respectively and are 0 while correspondent failure indices are smaller than 1. They are obtained by defining a slope between the onset of damage and failure. To define this slope, equivalent stresses and strains are calculated for each failure mode, with expressions from [98]:

$$\epsilon_{eq} = \begin{cases} \sqrt{(\langle\epsilon_1\rangle^+)^2 + \gamma_{12}^2 + \gamma_{13}^2} & \text{for FFT} \\ \langle -\epsilon_1\rangle^+ & \text{for FFC} \\ \sqrt{(\langle\epsilon_2\rangle^+)^2 + \gamma_{12}^2 + \gamma_{23}^2} & \text{for MFT} \\ \sqrt{(\langle -\epsilon_1\rangle^+)^2 + \gamma_{12}^2} & \text{for MFC} \end{cases} \tag{4.10}$$

$$\sigma_{eq} = \begin{cases} \frac{\langle\sigma_1\rangle^+\langle\epsilon_1\rangle^+ + \tau_{12}\gamma 12 + \tau_{13}\gamma_{13}}{\epsilon_e q} & \text{for FFT} \\ \frac{\langle -\sigma_1\rangle^+\langle -\epsilon_1\rangle^+}{\epsilon_e q} & \text{for FFC} \\ \frac{\langle\sigma_2\rangle^+\langle\epsilon_2\rangle^+ + \tau_{12}\gamma 12 + \tau_{23}\gamma_{23}}{\epsilon_e q} & \text{for MFT} \\ \frac{\langle -\sigma_2\rangle^+\langle -\epsilon_2\rangle^+ + \tau 12\gamma 12}{\epsilon_e q} & \text{for MFC} \end{cases} \tag{4.11}$$

.

The onset equivalent strain and stress $\epsilon_{eq,0}$ and $\sigma_{eq,0}$ are the values calculated with equations 4.10 and 4.11 when the failure indices become 1. Because most likely the failure index will be higher than 1 in the 1st iteration where damage is predicted, the value can be adjusted by dividing it by the square root of the failure index (scaling function). At failure completion (maximum damage), the equivalent strain is obtained with the crack band method developed in [99]:

$$\epsilon_{eq,f} = 2\frac{G_c}{\sigma_{eq,0}L}. \tag{4.12}$$

In equation 4.12, $G_c$ is the mode-specific fracture toughness, which can be determined experimentally. $L$ is the characteristic length of the element, calculated independently of the crack direction, for solid elements, as

$$L = \sqrt{\frac{V}{t}}, \tag{4.13}$$

where V is the volume of the element and t the thickness of the ply. For 2D elements, L is simply $\sqrt{A}$. The characteristic length serves to remove some of the mesh refinement dependency of damage propagation. Finally, each damage variable at a given iteration where the equivalent strain is $\epsilon_e q$ is

$$d = \frac{\epsilon_{eq,f}}{\epsilon_{eq}} \frac{\epsilon_{eq} - \epsilon_{eq,0}}{\epsilon_{eq,f} - \epsilon_{eq,0}}. \tag{4.14}$$

Each integration point has a maximum degradation of 1 and its damage is irreversible, meaning d is always at its maximum value in the simulation so far.

### 4.1.3. Other considerations

**Non-linearity**

The analysis must be non-linear to account for both degradation and material behaviour. Degradation is addressed with the MDM, while the material behaviour is addressed by adjusting the in-plane shear relation. The Han-Tsai fit of that experimental stress-strain curve

$$\gamma_{12} = \frac{1}{G_{12}}\tau_{12} + \beta\tau_{12}^3 \tag{4.15}$$

is adopted, through which the shear non-linearity parameter $\beta$ is obtained with the least squares method.

In the context of the established constitutive model, $\tau_{12}$, which is normally obtained (omitting the degradation for simplicity) with

$$\tau_{12,i+1} = \tau_{12,i} + G_{12}\Delta\gamma_{12}, \tag{4.16}$$

becomes

$$\tau_{12} = \tau_{12,i} + \frac{1}{\frac{1}{G_{12}} + 3\beta\tau_{12,i}^2}\Delta\gamma_{12}. \tag{4.17}$$

**Element Type**

The constitutive model and criteria presented in the previous sections can be applied to any element type. Solid elements are required to obtain the through-thickness stresses, which are used to predict delaminations. This failure is mode is, however, not addressed in the current CDM. For the case studies that will be presented in section 5, conventional shell elements are more adequate, since they significantly reduce the computational cost - reducing the duration of each simulation is key since the SFEM involves running hundreds at a time.

Specifically, the Abaqus S4 element type, a 4-node, linear, full integration quadrilateral element represented in figure 3.1, is chosen. Each of the 4 integration points will have different material properties in the stochastic simulations, and their formulation can easily be combined with the KL implementations of section 3. Since the test cases will only feature in-plane loading, only 1 layer of integration points through-thickness is required.

To use solid elements, such as C3D8, a simple correlation can be made with the Q4 element random field discretization, by considering only in-plane material property variation - integration points with the same in-plane coordinates have the same properties.

**Step size**

To maximize the efficiency of the simulations, two maximum step increment sizes are used in different stages of the analysis. Until damage initiation, a relatively high value can be used, since the only nonlinear effect is that of the in-plane shear, which affects the predicted stresses. After damage initiation, small increments must be made, since the properties of elements are degraded at each step.

**In-situ strengths**

In-situ shear and transverse tensile strengths are used as they have been reported to improve the accuracy of matrix crack growth prediction. The model, developed by Camanho et al. [100], distinguishes between embedded and outer plies, as well as thick and thin plies. The thick ply values, which are lower, serve as a lower bound to the others, so their intersection marks when the transition should be made.

The in-situ shear strength is given by

$$S_{12,IS} = \sqrt{\frac{\sqrt{1+\beta\phi G_{12}^2}-1}{3\beta G_{12}}}, \tag{4.18}$$

with

$$\phi = \begin{cases} 12\frac{S_{12}^2}{G_{12}} + 18\beta S_{12}^4 & \text{for thick embedded plies,} \\ \frac{48G_{IIc}}{\pi t} & \text{for thin embedded plies} \\ \frac{24G_{IIc}}{\pi t} & \text{for outer plies.} \end{cases} \tag{4.19}$$

The in-situ transverse tensile strength is given by

$$Y_{T,IS} = \begin{cases} 1.12\sqrt{2}Y_T & \text{for thick embedded plies,} \\ \sqrt{\frac{8G_{IC}}{\pi t \Delta_{22}^0}} & \text{for thin embedded plies} \\ 1.79\sqrt{\frac{G_{IC}}{\pi t \Delta_{22}^0}} & \text{for outer plies,} \end{cases} \tag{4.20}$$

with

$$\Delta_{22}^0 = 2(\frac{1}{E_2} - \frac{\nu_{21}^2}{E_1}). \tag{4.21}$$

## 4.2. Input properties and parameters

The SFEM inputs are summarized in table 4.1, which specifies how they may be obtained. These inputs are for the general 3D case, and some will not be used with 2D element modelling. Transversely isotropic assumptions mean $\nu_{13}$, $G_{13}$, $G_{23}$ and $E_3$ are omitted. However, they are independent random fields as well, meaning although they have the same stochastic parameters as in the other transverse direction, the value in a simulation will be different.

Each random property's mean and standard deviation, which will be the same at every integration point, is obtained by testing several coupons and assuming a normal distribution fitted to the obtained values. For some test cases, experimental data may not always be available. Nevertheless, for the variables referenced with ASTM standard and DIC testing, the latter marks the possibility of informing the correlation parameters $b_{cX}$ and $b_{cY}$ through DIC data. If not, the correlation can be inferred from similar cases. Deterministic variables correspond to the material but not necessarily the specimen being modelled - note that the fracture energies are usually obtained through compact tension and compression specimen. Otherwise, if no such data is available, they can also be assumed based on other materials or convergence of the model to the experimental results.

Finally, $\alpha_0$ is assumed as $53°$, which is common practice in literature [101], and $\beta$ is calculated through the Han-Tsai fit of the experimental shear stress-strain curve, with the process of determining the remaining inputs being described in section 4.3.

## 4.3. Summary of methodology

The diagram in figure 4.2 describes the workflow of the proposed stochastic method. The steps can be summarized as follows:

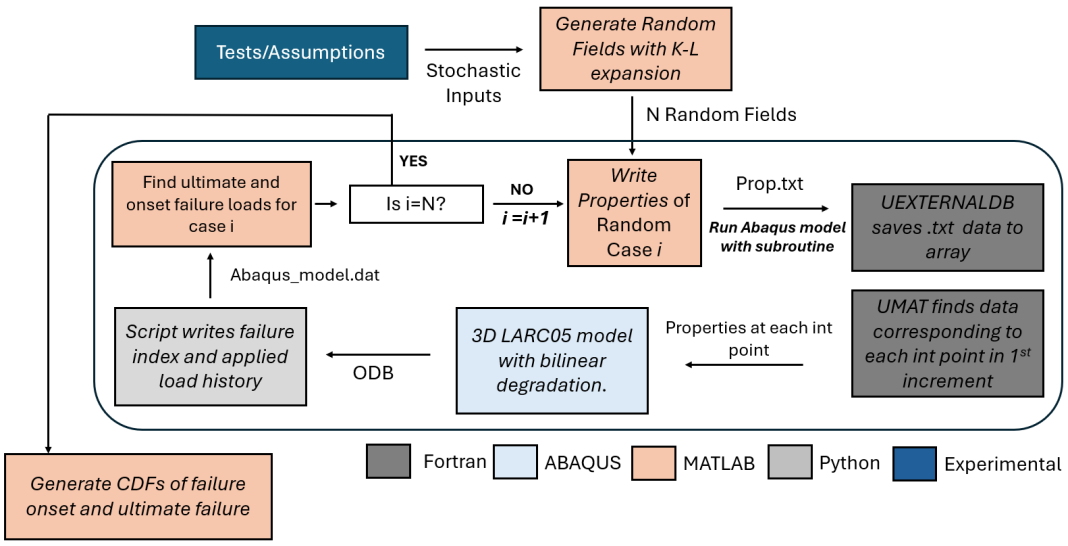


**Figure 4.2:** Workflow diagram

**Table 4.1:** Input variables of the FE model.

| Input | Random Field ($\mu$ + $\sigma$) | Constant |
|---|---|---|
| $E_1$ | Experimental (DIC + ASTM) | |
| $E_2$ | Experimental (DIC + ASTM) | |
| $\nu_{12}$ | Experimental (DIC + ASTM) | |
| $\nu_{23}$ | Experimental (ASTM) | |
| $G_{12}$ | Experimental (DIC + ASTM) | |
| $X_T$ | Experimental (ASTM) | |
| $X_C$ | Experimental (ASTM) | |
| $Y_T$ | Experimental (ASTM) | |
| $Y_C$ | Experimental (ASTM) | |
| $S_{12}$ | Experimental (ASTM) | |
| $\alpha_0$ | | Literature ($53°$) |
| $G_{FFT}$ | | Experimental (ASTM) |
| $G_{FFC}$ | | Experimental (ASTM) |
| $G_{MFT}$ | | Experimental (ASTM) |
| $G_{MFC}$ | | Experimental (ASTM) |
| $\beta$ | | Experimental (curve fitting) |
| $b_{cX}$ | | DIC |
| $b_{cY}$ | | DIC |
| $M$ | | KL error parameters |
| $N_\theta$ | | Convergence |

- **Tests/Assumptions**
  The material is characterized in terms of its properties and their variability. Tests give the mean and variance of random lamina properties. The additional stochastic inputs are the number of KL terms $M$, the correlation parameters $b_{CX}$ and $b_{CY}$ and the number of random cases $N_\theta$. M is chosen based on its effect on the local and global variance errors, $\epsilon_{M,\sigma_w^2}$ and $\bar{\epsilon}_{M,\sigma_w^2}$. The correlation parameters are chosen based on their effect on error parameter $\epsilon_{\sigma_s}$, which refers to the spatial standard deviation. To accurately calculate $\epsilon_{\sigma_s}$, $\sigma_s$ must refer to the same spatial domain as the target standard deviation, which can be obtained from DIC data. If the FE domain is different, or the mesh is not uniform, the parameters can be assumed from a similar case. $N_\theta$ must be big enough so that the results converge, so it is informed by prior simulations and increased in case convergence is not found.
- **Generate Random Fields**
  $N_\theta$ random fields, with a chosen 2D geometry, are generated, for each of the random properties, for each ply of the laminate. The Karhunen-Loève expansion is used to discretize the variables in each integration point, with either the galerkin solution or the bounding box solution. The latter is of more practical use, since it doesn't require an RF mesh, and is significantly faster to compute. The galerkin solution should be used if non-Gaussian probabilistic distributions better represent the variables, if a different covariance function is chosen, or for cases where the bounding box encompassing the geometry includes too big of a portion that is not part of the FE mesh, excessively distorting the correlation.
- **Transfer properties of a random case to Abaqus**
  For random case i, the properties are written to a file. This file is read, before the analysis starts,

through Abaqus subroutine UEXTERNALDB, which is usually used to open external files. In the first increment, the UMAT subroutine finds the properties of if each integration point by matching the coordinates with one of the points listed in the file. Only the in-plane coordinates are matched, so integration points of the same lamina have the same values through thickness. This is then saved and for the rest of the analysis the properties are read directly.

- **Run progressive failure model and write results**
  The model described in section 4.1 is run. This is a CDM which combines failure initiation ruled by the Larc05 criteria with bilinear degradation. Python/Abaqus scripting is used to write to a file the results of the analysis, when it stops converging. Those results are the values at every step of the damage index at every integration point, as well as of the applied force on the laminate.
- **Process results**
  From the results, the ultimate failure load is retrieved, as the 5% load drop value. The damage onset load for each mode and ply or integration point is the first value before ultimate failure for which the damage index is not 0. After this post-processing step, step 3 is resumed for the next random case.
- **Statistical analysis**
  When data has been obtained for all random cases, statistical post-processing is done. Outliers, most often cases of non-convergence, are removed. Then several sets of data can be fitted to a probabilistic distribution. For the ultimate failure values, this consists only of calculating their mean and standard deviation, in the Gaussian distribution case, or calculating a maximum likelihood estimate of the parameters for another type of distribution. However, for the failure relating to each mode, this is not so straightforward.

  For a given random case, damage onset occurs on a ply when the sum of the damage indexes of all its elements is no longer 0. However, due to the stochastic nature of the analysis, the same type of failure may not occur for all random cases. This is because the simulations' data goes until ultimate failure, which will precede some failure modes on some plies. To deal with this, one possibility would be to remove those cases altogether, but that would artificially increase the probability of that mode occurring, when the data tells us otherwise.

  To include the information from these random cases, their data was taken as right-censored, meaning the ultimate failure load is the damage onset value when that damage never occurs. Then a maximum likelihood estimate is done, through function *mle*, of the distribution parameters. This function minimizes the negative loglikelihood function, given by

$$-\log \prod_{x \in X} P(x|\theta), \tag{4.22}$$

  where

$$P(x|\theta) = \begin{cases} f(x) & \text{for exactly measured observations,} \\ 1 - F(x) & \text{for right-censored observations,} \end{cases} \tag{4.23}$$

  and f(x) and F(x) are the PDF and CDF, respectively. Note this calculation is not done for failure modes and plies where damage is never or almost never found, since those values would consist mostly of right censored data and not be informative.

## 4.4. Conclusions and Limitations

Section 2.1.2 described the constitutive model of the SFEM, as well as the process of calculating the Larc05 failure indices and the bilinear degradation damage variables. The UMAT that implements these equations is available for both solid and shell elements, although the present study will use the latter. Shear non-linearity and in-situ strengths are also incorporated into the model. The chosen CDM is expected to predict ultimate failure sufficiently well, but is limited in two main aspects: the matrix cracking progression it outputs is known to not match what is observed experimentally, with excessive smearing, and delaminations are not modelled. The first problem could be addressed by, for example, implementing XFEM-based MFT initation, but this was deemed to costly in the computational sense for this study. Delaminations may be addressed with the inclusion of cohesive elements/behaviour, but for

convergence and computational time reasons this was again discarded. In section 5, test cases where delaminations are not expected to be significant are chosen. Finally, section 4.2 listed 14 random variables, for which 10 means and standard deviations (in the solid element case) have to be provided as input. Additionally, 6 parameters are taken as constant for all elements, and 4 stochastic inputs are obtained based on previously defined error parameters. Section 4.3 showed how the FEM and the KL expansion are connected in a loop to create the SFEM framework, and detailed the statistical post-processing, which involves right-censored data considerations.

# 5

# Validating the Stochastic Method

In this section, the stochastic methodology is validated with three test cases. The first test case, addressed in section 5.1, is a quasi-isotropic laminated plate, made from carbon fiber UD prepreg, in uniaxial tension. This specific case is based on an experimental campaign from [5], where a SFEM was already developed and gave good predictions of the ultimate and progressive failure PDFs. DIC and mechanical test data is available for these specimens, and the probabilistic results are compared not only with experimental curves but also with variations of sampling methods: KL+LHS+Hashin and Random MC discretization.

In section 5.2, the more complex case of CFRP specimen in open hole tension, from [96], is modelled. Stochastic inputs are assumed and results are compared with experiments and the same sampling method variations. The goal is to check if the method provides acceptable reliability predictions, as well as acceptable probabilistic predictions of damage initiation and progression around the hole.

In section 5.3, another open-hole tension test is modelled, from [102]. With a lack of data regarding the variation of material properties in the loaded specimen, the example serves to study the effect of the correlation and standard deviation stochastic inputs on the results, as well as to understand how the results may differ from the case of section 5.2 (or confirm the previous conclusions).

For all test cases, a convergence/error analysis of the stochastic parameters (point-wise variance, spatial variance, KL terms and number of random cases) is performed. The deterministic model and results are then presented, followed by the stochastic ones, and all results are discussed. Finally, section 5.4 covers the main conclusions and points of the present chapter.

## 5.1. Plate in uniaxial tension - Nastos et. Al

Several quasi-isotropic specimen, manufactured from UD carbon fiber prepreg Hexply F6376C-HTS(12K)-5%-35% with Autoclave curing, were tested in quasi-static uniaxial tension until failure by Nastos et al. [5]. Before, lamina properties were obtained through 3 ASTM standard material characterization tests ($0°$, $90°$ and $45°$ laminates in tension), for elastic and shear moduli, on all in-plane directions, as well as tensile and shear strengths and poisson's ratio. DIC was used to quantify the variability of the elastic properties within each specimen. This experimental campaign is detailed in [5].

The quasi-static tensile testing was conducted with 9 rectangular plates with lamination $[(0/90/\pm 45)_s]_2$ and dimensions 250x25x2mm$^3$. The loading was displacement controlled, with a loading rate of 1mm/min. Figure 5.1 shows a specimen after tensile breakage, which is the ultimate or last-ply-failure (LPF) mode.

### 5.1.1. Applying the methodology

**Tests/Assumptions**

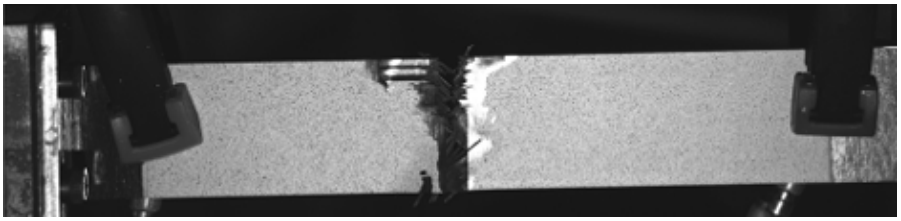

**Figure 5.1:** Quasi-static tensile testing specimen at failure [5].

The material properties for the FE model are taken from these tests [5], [103] and [104], or assumed. They are listed in table 5.1.

**Table 5.1:** Material properties of Hexply F6376C-HTS(12K)-5%-35%

| Property | Mean (standard deviation) |
|---|---|
| $E_1$ [GPa] | 143.7 (18.4) |
| $E_2$ [GPa] | 9.2(2) |
| $\nu_{12}$ | 0.37(0.14) |
| $\nu_{23}$ | 0.3 (0.1) |
| $G_{12}$ [GPa] | 5.14 (0.69) |
| $X_T$ [MPa] | 2274 (146.9) |
| $X_C$ [MPa] | 1849 (140.2) |
| $Y_T$ [MPa] | 107.6 (9.1) |
| $Y_C$ [MPa] | 255 (8.85) |
| $S_{12}$ [MPa] | 96.3 (0.8) |
| $\alpha_0$ [°] | 53 |
| $G_{FFT}$ [N/mm] | 67.1 |
| $G_{FFC}$ [N/mm] | 103.1 |
| $G_{MFT}$ [N/mm] | 0.25 |
| $G_{MFC}$ [N/mm] | 0.8 |
| $\beta$ [$\times 10^{-8}$MPa$^{-3}$] | 3 |
| $G_{Ic}$ [N/mm] | 0.25 |
| $G_{IIc}$ [N/mm] | 1 |

The bounding box solution of the KL expansion is used to generate the RFs with $d_r = 0$, since for this case the analytical solution exists for the exact FE domain. The correlation parameters are decided based on the DIC data. The measured $E_1$ distributions (figure 5.6) are used to inform those parameters. They were calculated by obtaining the strains and averaging the calculated values in the 25% to 75% range.

From averaging the standard deviations at all measured $E_1$ fields, the variable's target spatial standard deviation $\sigma_s$ is set as 3.5% of the mean, approximately 5GPa. The correlation parameters $b_{cx}$ and $b_{cy}$ are set as equal, and are varied within a range to find the value that minimizes the error $\epsilon_{\sigma_s}$, with $N_\theta$ set as 500. A minimum is found at $b = 7.35$, as is shown in figure D.1, in appendix D. Note that all values tested used 40 KL terms ($M = 40$), which is enough that the global error variance $\bar{\epsilon}_{M,\sigma_w^2}$ has converged to under 5% for all values of b.

Figure 5.2 shows that with M=40 and $b = 7.35$ the error is less than 1%. The local error variance $\epsilon_{M,\sigma_w^2}$, represented in 5.3, is very small even at the peaks, so 40 KL terms will be used in the expansion.

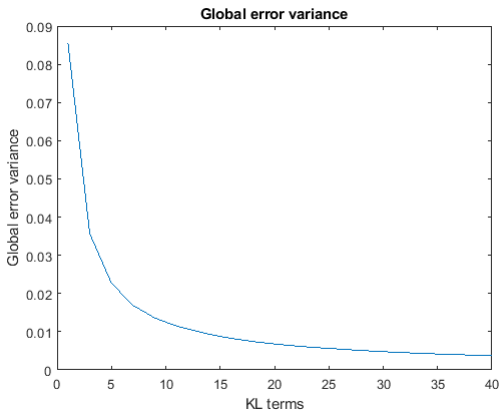


**Figure 5.2:** Global error variance $\bar{\epsilon}_{M,\sigma_w^2}$ for different values of M.

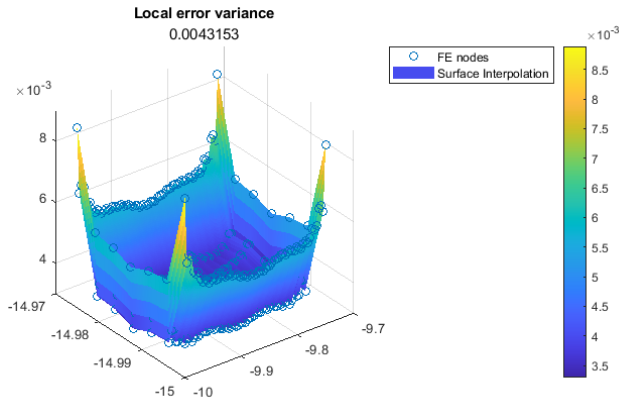


**Figure 5.3:** Local error variance $\epsilon_{M,\sigma_w^2}$ for M=40.

Figure 5.4 shows the convergence of the mean and standard deviation $\sigma_w$ at an arbitrary point and 5.5 shows the convergence of $\sigma_s$, all in relation to $E_1$. For $N_\theta = 300$, all statistical moments are stable, and even for values from around 200, the error is smaller than 2%. A convergence study of the results will be presented, but $N_\theta = 200$ should be enough to represent the variability of the fields accurately.

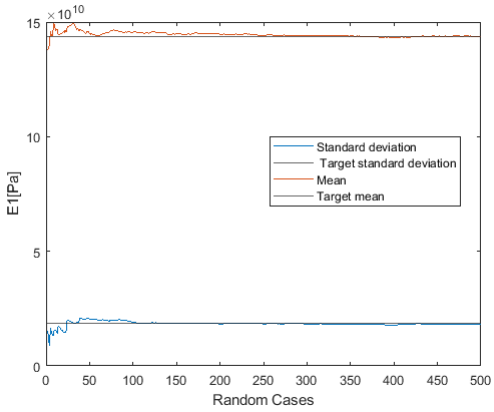


**Figure 5.4:** Convergence of the $E_1$ mean [Pa] and standard deviation [Pa] at an arbitrary point with increase of $N_\theta$.

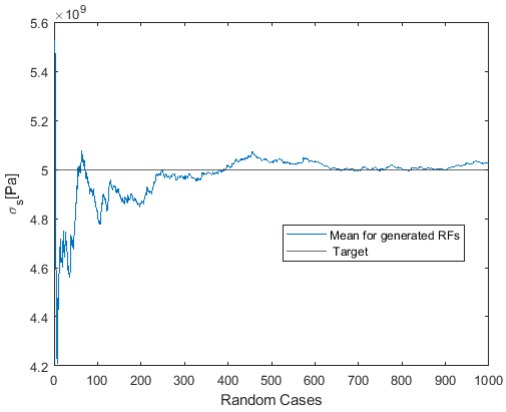


**Figure 5.5:** Convergence of the $E_1$ $\sigma_s$ [Pa] with increase of $N_\theta$.

### Generate Random Fields

Now that all stochastic and deterministic inputs are defined, step 2 of the methodology can be carried out. 200x10x16 ($N_\theta$ X Number of Random Variables X Number of Plies) random fields are generated, with values at every integration point of the FE mesh. Figure 5.6 shows 4 arbitrarily chosen $E_1$ RFs, generated with the KL expansion, and 4 distributions obtained with DIC.

### FE model

The model described in section 4.1 is run with a mesh of 63 by 6 S4 (conventional) shell elements. The left side is clamped and displacement loading is applied on the right, with the Y and Z rigid body motions constrained. The boundary condition representation on Abaqus can be found in appendix D.

The deterministic model is first run, predicting ultimate failure at 41.22kN. First-ply-failure (FPF) is matrix cracking of the 90° plies (MFT), followed slightly after by tensile fiber failure (FFT) of the $0°$ plies, which corresponds to ultimate failure.

In figure 5.7, the FFT index at the elements of a 0 ° ply, before failure, is represented. Evidently, the ply will fail simultaneously, as the stress is uniform. Figure 5.8 is obtained after running one of the 200

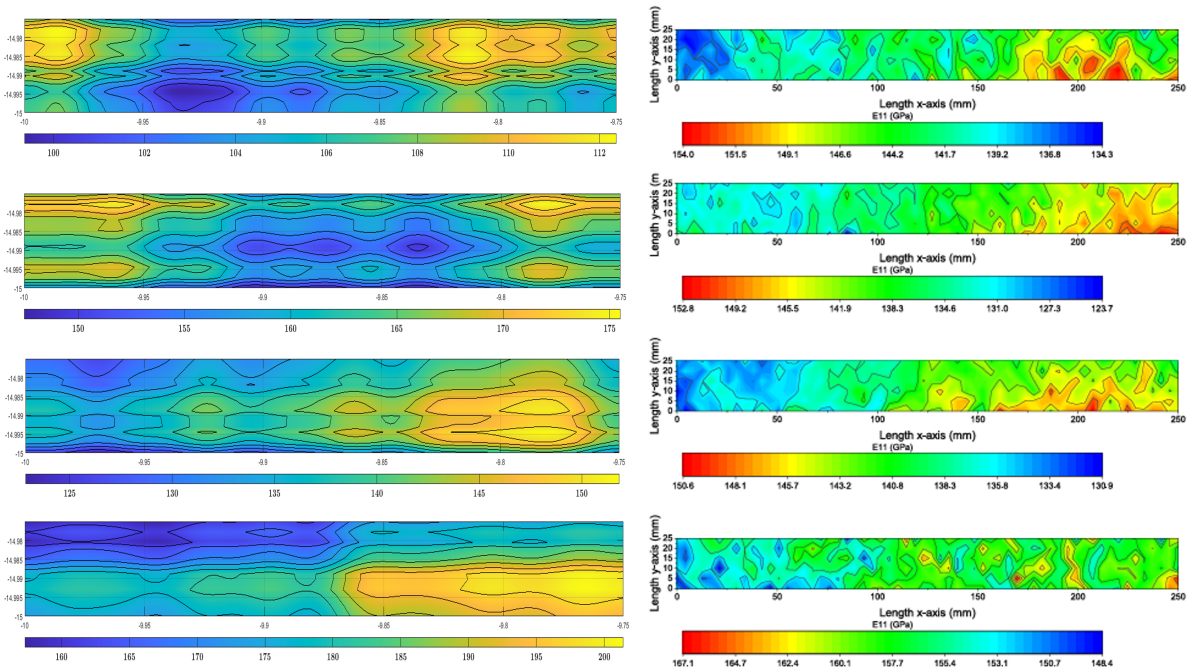


**Figure 5.6:** Examples of $E_1$[GPa] distributions obtained with DIC (right) and generated with the KL expansion (left).

stochastic simulations, chosen arbitrarily. As expected, it contrasts with figure 5.7, in the sense that the index is higher in some parts of the lamina, which will fail first. The $E_1$ distribution of figure 5.9, for the same ply and random case, closely matches the index distribution, showing the relation in the stochastic model between the spatial variability of a property and failure.

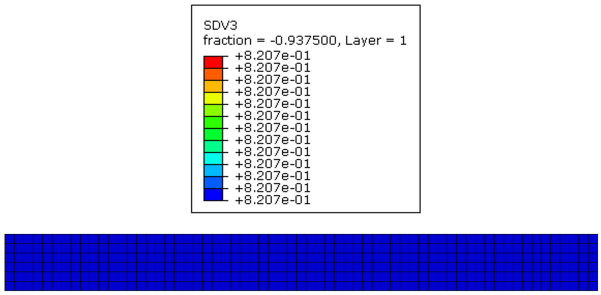


**Figure 5.7:** Failure index for fiber tension failure in deterministic model, $0°$ ply.

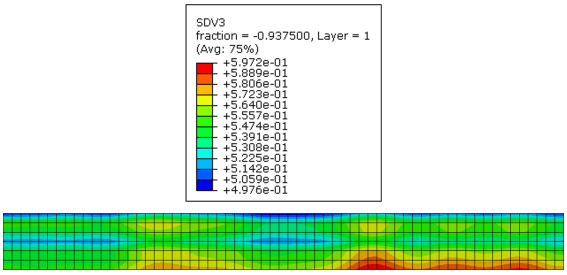


**Figure 5.8:** Failure index for fiber tension failure in stochastic model, arbitrary case and step, $0°$ ply.

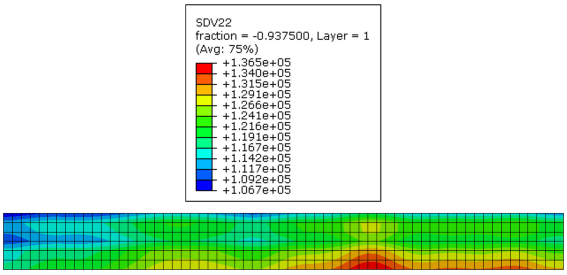


**Figure 5.9:** $E_1$ [MPa] distribution, arbitrary case and step, $0°$ ply.

### 5.1.2. Results and Discussion

Different distributions were fitted to the model's ultimate failure results, as well as to the experimental failure data, and are compared in figures 5.10 and 5.11 with the empirical CDF.

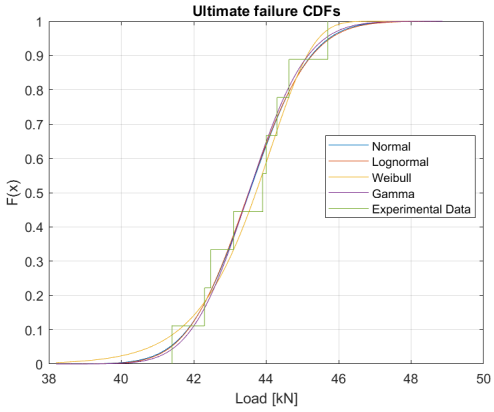


**Figure 5.10:** Empirical, Normal, Lognormal, Weibull and Gamma distributions fitted to experimental failure data.

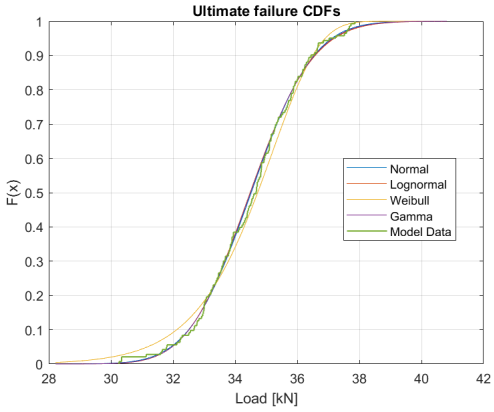


**Figure 5.11:** Empirical, Normal, Lognormal, Weibull and Gamma distributions fitted to the SFEM's failure data.

The empirical CDF is defined as for the Kolmogorov–Smirnov test, which, in the 1-sample case, is used to test if a sample (a set of data) came from a given distribution [105]. It is given by

$$F_n(x) = \frac{1}{n}\sum_{i=1}^{n} 1_{]-\infty,x]}(X_i), \tag{5.1}$$

meaning that the probability of failure at a given load is the number of failures measured at equal or lower loads divided by the total number of measurements. The Kolmogorov-Smirnov test was then used, employing MATLAB's *kstest* function, to compare the empirical distribution with the others.

For the experimental distribution, the hypothesis could not be rejected at a 5% significance level with any of the distributions. Furthermore, the p-value, which evaluates the probability of a sample as or more extreme than the measured one coming from the distributions, was higher than 0.92 for all cases. Given the small ammount of experimental measurements, it is clear there is not much difference between fitted distributions, and the gaussian hypothesis is assumed.

For the model's ultimate failure results, the hypothesis could again not be rejected for any of the distributions. However, the p-value for weibull (around 0.6) was lower than for the other distributions. Despite the difference still being small, the normal distribution is, again, assumed. The complete results of the Kolmogorv-Smirnov test are presented in table D.1.

Figure 5.12 shows three normal CDFs fitted to the ultimate failure values obtained with three different stochastic models. For all models, the number of samples was one that guaranteed convergence of the mean and standard deviation of the dataset.

The proposed method is compared to an identical one that used Hashin failure criteria instead of Larc05 (KL+LHS+Hashin), and to another that, instead of using the KL expansion, generates uncorrelated RFs without considering a covariance function, independently at each integration point (Random MC + Larc05). The latter is relevant for its frequent use in literature [23]. The Hashin criteria failure modes and index expressions are detailed in appendix B. Finally, all methods are compared with the CDF of a normal distribution fitted to ultimate failure values obtained in the aforementioned experimental campaign. It is important to note here that this last plot has limited significance, the curve having been fitted from only 8 values, although the 95% confidence intervals of the statistical moments will be more useful for comparisons.

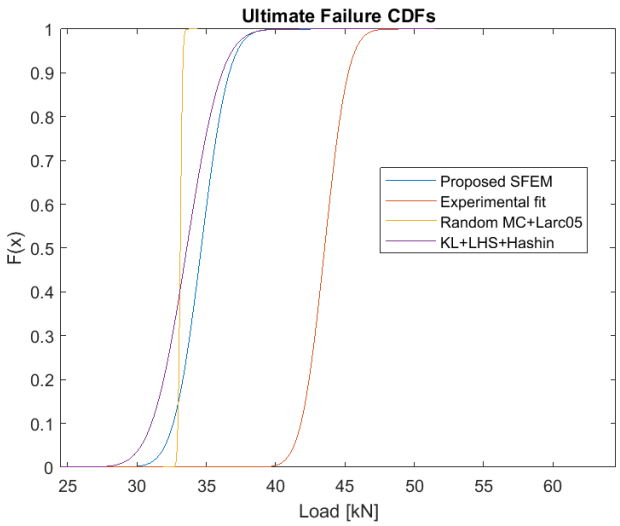


**Figure 5.12:** Ultimate failure CDFs - normal distributions fitted to the results of proposed method, KL+LHS+Hashin and Random MC + Larc05 variations, as well as experimental values.

First, the results with the Larc05 (proposed method) and Hashin are similar. This is likely because the model predicts FFT dominated ultimate failure, slightly preceded by matrix cracking, and the FFT criterion is similar for both criteria. The difference that is found is caused by variations in MFT initiation, which have limited impact in ultimate failure values.

The difference between the Random MC discretization method and the KL methods is notable. Because each point is attributed a value independently, the variation between random cases is much smaller, as within each RF the range is always similar. This causes the standard deviation to be very small as well. Figure 5.13 shows an example of an RF generated with this method. It should be added that convergence problems were much more common when using this type of RF.

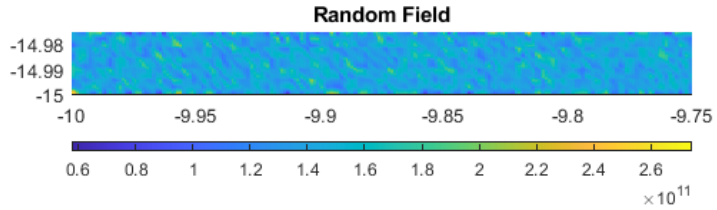


**Figure 5.13:** RF of $E_1$[Pa] generated with random independent values at each point (Random MC method).

Table 5.2 summarizes the ultimate failure results. It also includes the load values that correspond to a FPF and LPF reliability of 0.9999 (failure probability of $10^{-4}$), calculated by inverting the CDFs. This reliability value has often been used as a target for aerospace structures [43] [106].

The experimental fit mean is quite different from all models results, being off by around 9kN. Most of this difference comes from the offset between the deterministic and stochastic means of the model (6.6kN, or 16%). A possible explanation for the magnitude of this effect is that, since the RFs always have weak areas, the laminate will fail when those areas of (one of) the $0^\circ$ plies fail. Because failure in this case is so dominated by those plies, and consequently their $E_1$ and $X_T$ distributions, a "weaker than average" area will always exist, lowering the mean when compared with the deterministic model.

This effect was also reported in [23]. It would likely be smaller if cases where failure is more localized or more progressive, in the sense that multiple plies and modes contribute significantly to it. The discrepancy makes the stochastic models overly conservative, though at the same time it shows how not considering material uncertainties can be unconservative.

The KL methods offer good predictions of the standard deviation, within the 95% confidence interval, and again being slightly conservative. The Random MC method under-predicts it significantly. Between these two discretization methods, the first one seems to better represent the stochastic nature of composite failure, by using more realistic property distributions that take into account spatial correlation. On the other hand,the difference between the stochastic predictions of the Hashin and Larc05 criteria is not significant enough to conclude about their comparable accuracy, as both give similar variance results.

Regarding the loads corresponding to a reliability of 0.9999, a simple comparison can be made with the safety factor design approach, assuming it targets the same reliability value. With a safety factor of 1.5, the deterministic model predicts the structure to be safe until 27.48kN, which is overly conservative when compared to the proposed SFEM prediction. All approaches are conservative when compared with the experimental value, which is calculated with the lower and upper limit of the 95% confidence intervals of the mean and standard deviation, respectively.

**Table 5.2:** SFEM results - Nastos et. Al case study. Values in parenthesis represent the 95% confidence intervals.

| Model | Mean [kN] | Standard Deviation [kN] | Load($R_{FPF}$=0.9999) [kN] | Load($R_{LPF}$=0.9999) [kN] |
|---|---|---|---|---|
| Deterministic model | 41.22 | - | - | - |
| Proposed SFEM | 34.62 | 1.57 | 22.80 | 28.77 |
| KL + LHS + Hashin | 33.56 | 1.99 | 23.35 | 26.21 |
| Random MC + Larc05 | 33.13 | 0.14 | 22.75 | 32.62 |
| Experimental fit | 43.53 (42.5-44.56) | 1.33 (0.9-2.55) | - | 38.57 (35.92-41.23) |

The change in mean and standard deviation of the failure values, obtained with the proposed SFEM, with increase of $N_\theta$ is plotted in figures 5.14 and 5.15.

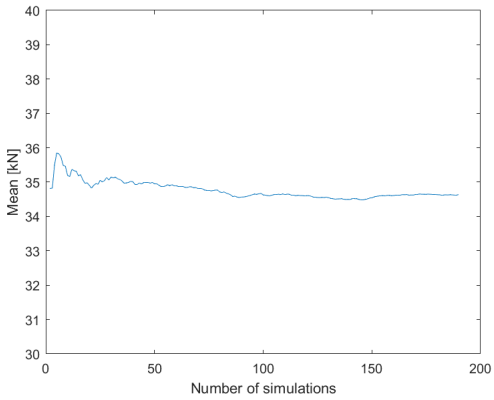


**Figure 5.14:** Change in mean [kN] of ultimate failure probabilistic distributions with increase of the number of simulations.

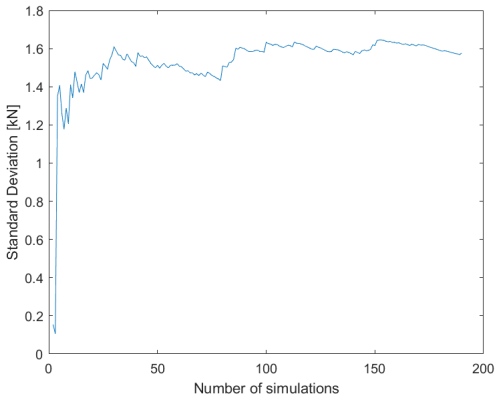


**Figure 5.15:** Change in standard deviation [kN] of ultimate failure probabilistic distributions with increase of the number of simulations.

At $N_\theta \approx 200$, all parameters have changed less than 2% in the past 50 or so iterations, and can be considered converged - in fact, the results are very stable after 100 simulations.

The CDFs of damage initiation for the predicted failure modes are shown in figure 5.16. For a given random case, a failure mode has occurred on a ply when there is that damage on at least one element. In this case, the probability is calculated of damage onset in any ply with a certain fiber orientation.

The same failure modes as the deterministic model are identified. As expected, the $90^\circ$ ply matrix cracking slightly precedes ultimate failure, and there is a lot of overlap between the two CDFs. This means that in some cases the failure may be predicted to be only FFT, while in others there may be extensive MFT damage propagation before LPF - this is not necessarily true however, as there is still some gap between the two curves, which may mean that in all simulations there was $90^\circ$ failure which soon after led to ultimate failure.

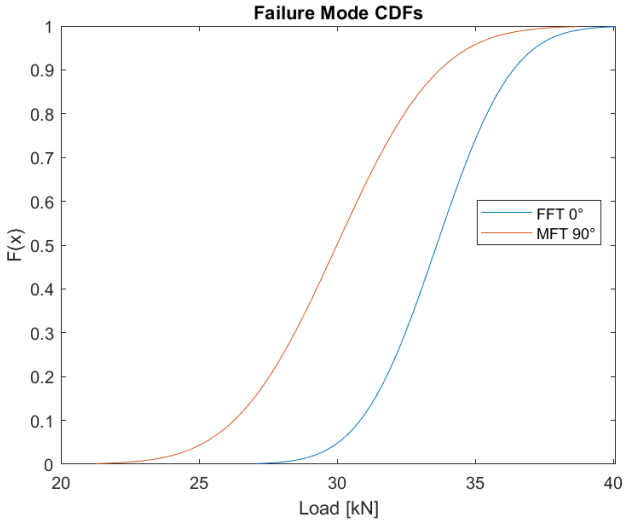


**Figure 5.16:** Damage initiation CDFs - normal distributions fitted to the Larc05 damage mode initiation loads. There is MFT in the 90° plies and FFT in the 0° plies.

The same damage initiation can be predicted on an element by element basis, as was explained in section 4.3. Then, for a chosen failure mode and ply, a 3D plot of the probability throughout the spatial domain of the specimen can be presented. Figure 5.17 shows this distribution for tensile matrix failure of the 90° plies.

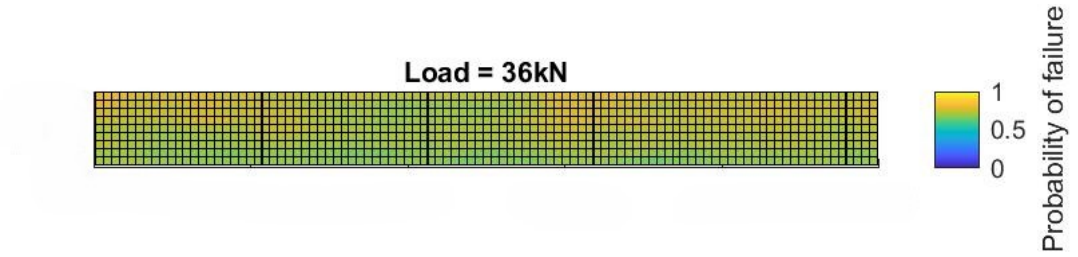


**Figure 5.17:** Probability of MFT damage in any $90^\circ$ ply at 36kN applied load, throughout the specimen.

The distribution of the probability is close to uniform, averaging around 60%. Compared with the damage onset probability at 36kN, from figure 5.16, it is much lower, since only the weakest parts of the lamina will fail in each case. Despite this, the plot is almost uniform, since no particular area should be statistically more prone to MFT, and with enough simulations the elements converge to the same results. This represents another advantage of the KL+LHS method: accurate local probabilistic results are not obtained with the Random MC distributions, at least not without an unreasonable number of simulations.

## 5.2. Open hole tension - van Dongen et al.

Notched CFRP specimen, made from autoclave curing of AS4/8552 UD prepreg, were tested until failure in quasi-static tension by van Dongen et al. [96]. Their quasi-isotropic lay-up was $[45/-45/0/90]_{2s}$ and dimensions 250x25x2.72mm$^3$. The hole had a nominal diameter of 6.35mm and the displacement rate was 1mm/min.

### 5.2.1. Applying the methodology

**Tests/Assumptions**

The material property means for the FE model are taken from [96] or assumed based on results. No

information exists on the variance of these parameters from specimen to specimen. Due to material, manufacturing process and specimen geometry similarities, the coefficients of variation (COVs, or ratios of standard deviation to mean) of the first test case, presented in section 5.1, are assumed. These inputs are listed in table 5.3.

**Table 5.3:** Material properties of AS4/8552

| Property | Mean (standard deviation) |
|---|---|
| $E_1$ [GPa] | 135 (17.3) |
| $E_2$ [GPa] | 9.5(2.13) |
| $\nu_{12}$ | 0.32(0.12) |
| $\nu_{23}$ | 0.45 (0.15) |
| $G_{12}$ [GPa] | 4.9 (0.66) |
| $X_T$ [MPa] | 2207 (168.5) |
| $X_C$ [MPa] | 1531 (116.1) |
| $Y_{T,embedded}$ [MPa] | 82 (6.95) |
| $Y_{T,outer}$ [MPa] | 96 (8.14) |
| $Y_C$ [MPa] | 255 (8.85) |
| $S_{12,embedded}$ [MPa] | 111 (0.88) |
| $S_{12,outer}$ [MPa] | 111 (0.88) |
| $\alpha_0$ [°] | 53 |
| $G_{FFT}$ [N/mm] | 36.8 |
| $G_{FFC}$ [N/mm] | 80 |
| $G_{MFT}$ [N/mm] | 0.1 |
| $G_{MFC}$ [N/mm] | 0.4 |
| $\beta$ [$\times 10^{-8}$MPa$^{-3}$] | 3 |

The remaining stochastic inputs are also kept the same as the previous case study - $b_{cx} = b_{cy} = 7.35$, $M = 40$ and $N_\theta \approx 200$ (or a smaller number than leads to convergence). The RFs are generated with the bounding box solution, which due to the specimen width and length will give equal analytical distributions to those obtained in section 5.1, now discretized in a different mesh.

**FE model**

The model from section 4.1 is run with a mesh of 1691 S4 shell elements for each lamina. The element size is smaller near the hole, though even away from the stress concentration it should be limited to account for the material variations. The model and its boundary conditions are represented in figure 5.18.

The deterministic model is first run, predicting ultimate failure at 27.25kN. The effect of the mesh density on this value is detailed in table D.2. Matrix cracking in tension first occurs in the $90°$ plies, followed by the embedded $\pm 45°$ degree plies, which have lower in-situ strentghs, and then the $45°$ outer plies. Then there is FFT damage initiation in the $0°$ plies, which will lead to ultimate failure after several elements have failed along the net section. Close to that ultimate failure there are a few elements in the $\pm 45°$ plies with FFT damage as well.

The damage pattern of the matrix cracking in the $90°$ plies is shown in figure 5.19. Evidently, this pattern is constant for every ply with that orientation. It contrasts with the patterns in figures 5.20a and 5.20b, obtained for two different (inner and outer) $90°$ laminae in one of the 200 stochastic simulations. It is observable that the general failure mechanism is the same, but its extent and specific location

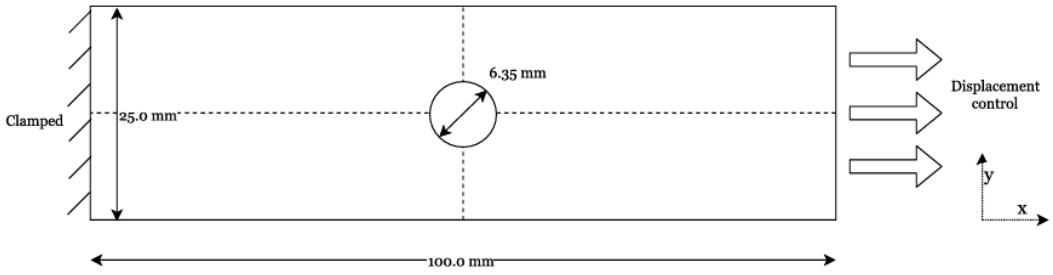


**Figure 5.18:** Model and boundary conditions for van Dongen et al. case study [96].

varies with each simulation and lamina - for the outer $90^\circ$ ply, damage has extended beyond that of the deterministic model, while less elements are damaged in the inner one, mostly in the net section.

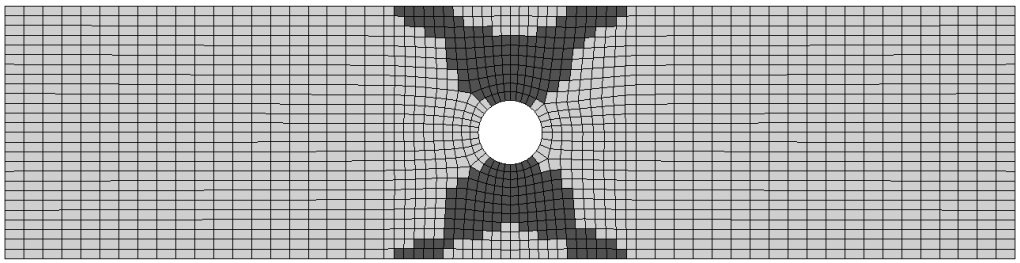

**Figure 5.19:** Progression of matrix tensile failure in $90^\circ$ plies - applied load 27kN, in deterministic model.

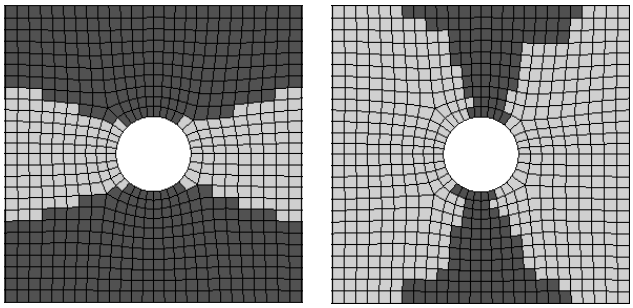

**(a)** Outer $90^\circ$ ply. **(b)** Inner $90^\circ$ ply.

**Figure 5.20:** Progression of matrix tensile failure in $90^\circ$ plies - applied load 27kN, in stochastic model, arbitrarily chosen random case.

## 5.2.2. Results and Discussion

Based on the Kolmogorov-Smirnov tests of section 5.1, gaussian distributions are assumed for all probabilistic results. In figure 5.21, the converged CDFs of normal distributions fitted to the ultimate failure values, obtained with the stochastic model and experimentally, are plotted. Only 6 values comprised the experimental dataset, so this curve has, again, limited significance (although the 95% confidence intervals are of interest).

There is a very slight decrease of the mean of the stochastic distributions when compared to the deterministic prediction (for the proposed SFEM around 1%). This difference is much smaller than for the case study of section 5.1. A possible explanation is that failure in this case is much more localized, meaning low strength areas far away from the hole do not cause failure. This localized failure also results in a much lower variance of the results (when compared with the unnotched case), which is also seen in the experimental values.

Table 5.4 lists the ultimate failure results and the load values that correspond to a FPF and LPF reliability of 0.9999. The standard deviations predicted by the KL methods are within the 95% confidence interval

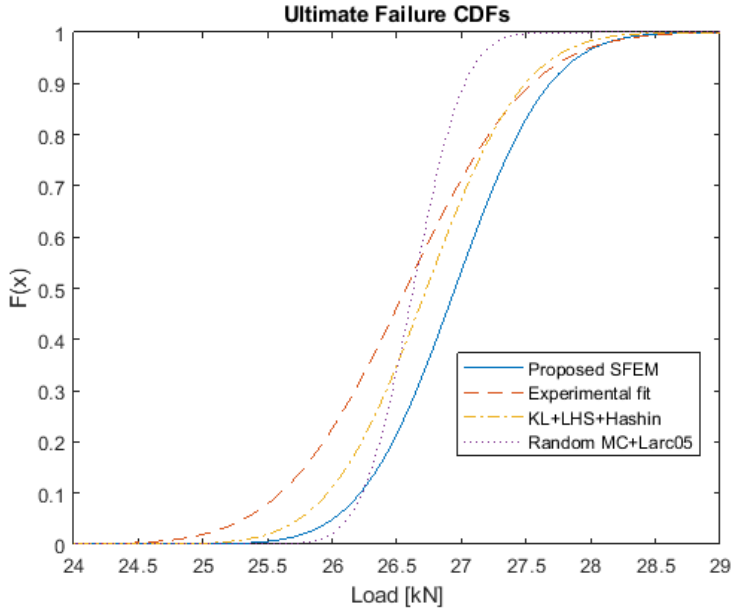


**Figure 5.21:** Ultimate failure CDFs - normal distributions fitted to the results of proposed method, KL+LHS+Hashin and Random MC + Larc05 variations, as well as experimental values.

and overall those results match well with the experimental dataset. The Random MC + Larc05 model, however, again under-predicts the variance, being outside of the interval. The different failure criteria, Hashin (KL+LHS+Hashin) and Larc05 (proposed SFEM), as seen for the previous case study, give similar results, including in terms of the predicted variance.

Regarding the maximum loads that the structure can see, based on the target reliability of 0.9999, a similar calculation as in the previous test case can be done. If it is assumed that a safety factor of 1.5 has the same reliability target, the maximum load that can be seen based on the deterministic analysis is 18.17kN, a value for which the probability of failure would be far smaller than the intended one. On the other hand, the stochastic methods may be slightly unconservative in this case.

**Table 5.4:** SFEM results - van Dongen et. Al case study. Values in parenthesis represent the 95% confidence intervals.

| Model | Mean [kN] | Standard Deviation [kN] | Load($R_{FPF}$=0.9999) [kN] | Load($R_{LPF}$=0.9999) [kN] |
|---|---|---|---|---|
| Deterministic model | 27.25 | - | - | 18.17 |
| Proposed SFEM | 27.00 | 0.55 | 6.08 | 24.94 |
| KL + LHS + Hashin | 26.72 | 0.60 | 6.47 | 24.51 |
| Random MC + Larc05 | 26.63 | 0.31 | 6.10 | 25.47 |
| Experimental fit | 26.57 (25.77-27.37) | 0.76 (0.47-1.86) | - | 23.74 (21.81 - 25.70) |

Figures 5.22 and 5.23 plot the convergence of the mean and standard deviation of the ultimate failure probabilistic distribution, obtained with the proposed SFEM method. Convergence is much faster for this case, with both statistical moments stabilizing after only 40 simulations. Likely, the model variance being smaller leads to faster convergence.

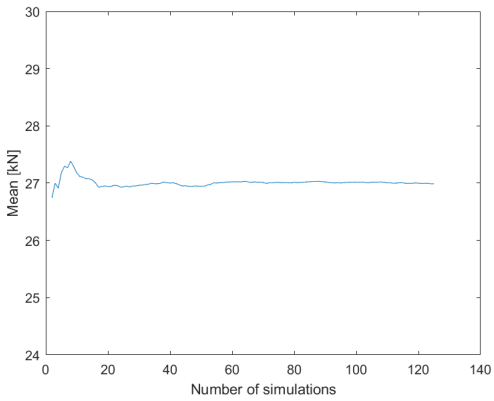


**Figure 5.22:** Change in mean [kN] of ultimate failure probabilistic distributions with increase of the number of simulations.

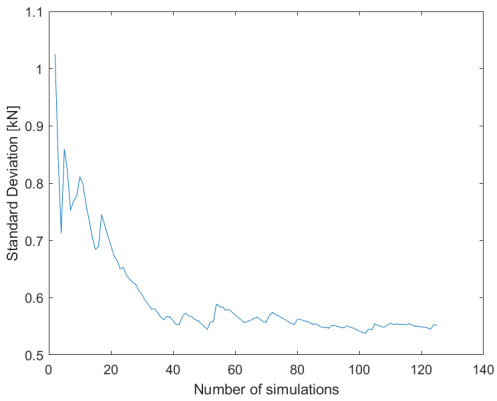


**Figure 5.23:** Change in standard deviation [kN] of ultimate failure probabilistic distributions with increase of the number of simulations.

The CDFs of damage initiation for the predicted failure modes are shown in figure 5.24. In this case, the probabilities refer to damage initiation in only one of the (outer) plies with each orientation, instead of any ply with that fiber angle.

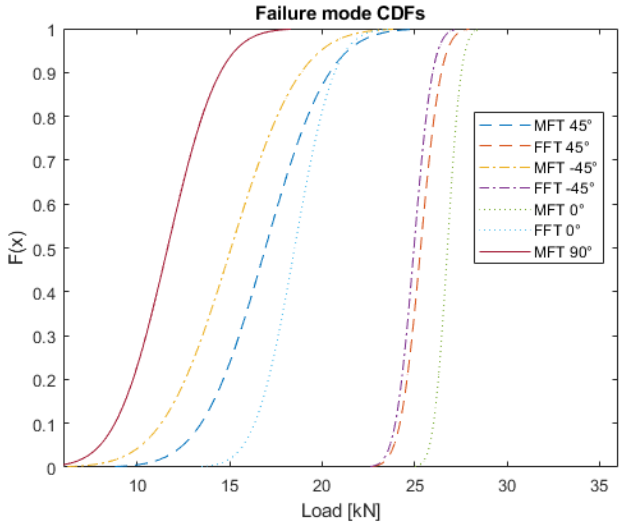


**Figure 5.24:** Damage initiation CDFs - normal distributions fitted to the Larc05 damage mode initiation loads. There is MFT in all plies, as well as FFT in the $0°$ and $\pm 45°$ plies.

The failure modes are the same as those predicted by the deterministic model, with the exception of matrix cracking in the $0°$ ply. MFT damage in that ply occurred in only a few elements and a minority of the simulations, but this is another interesting result that shows how stochastic analysis can differ from deterministic analysis and better capture the variability of damage modes and initiation values in CFRP specimen that is also seen in experiments. The curves generally follow the same pattern as the deterministic model: first $90°$ transverse matrix cracking, then MFT in the $-45°$ embedded ply and damage in the $45°$ outer ply. Ultimate failure is dictated by the $0°$ ply, though damage initiates there, on average, at 60% of the failure load. At higher loads there is longitudinal fiber failure in the $\pm 45$ degree plies, followed by MFT damage in the $0°$ ply, which almost coincides with ultimate failure.

Finally, integration-point-level probabilistic results are shown in figure 5.25, regarding matrix cracking in $90°$ plies. MFT is chosen for the plot as the pattern of this failure mode is of most interest, and the results for the other plies are shown in appendix D (figures D.3 and D.4).

The points where failure is most likely follow the pattern of figure 5.19. Despite the different possible

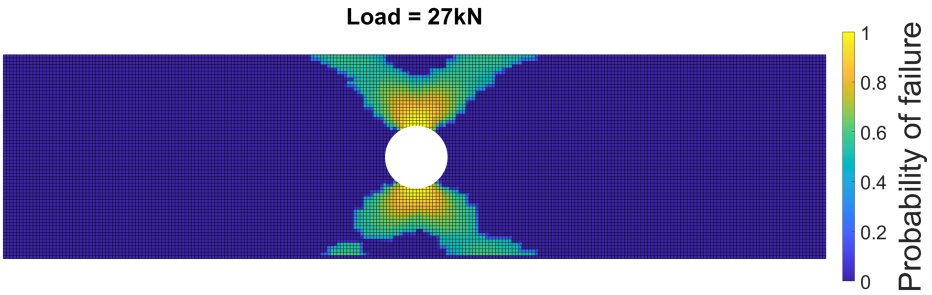


**Figure 5.25:** Probability of MFT in a $90°$ ply with 27kN applied load, throughout the specimen.

responses, like those shown in figures 5.20a and 5.20b, the average of probabilistic results converges to the pattern obtained with the deterministic model. The SFEM, however, shows the possibility of failure beyond or short of what is predicted in the deterministic analysis, with the non-zero probability area extending past the propagation seen in figure 5.19 and the damage likelihood increasing with the decrease of the distance to the hole.

The pattern predicted by the CDM-based FEM, as expected, does not accurately match the matrix cracking observed in experiments. Instead of a discrete crack, damage propagates in many directions, including through the fibers. This damage smearing is a known disadvantage of CDMs [96][107][108]. Nevertheless, the local failure results show the potential of the proposed SFEM for predicting in a probalistic way the propagation of damage in a laminate, which with other types of modelling may be used to obtain accurate predictions of crack growth/size, or even the extent and location of delaminations.

## 5.3. Open hole tension - Nixon-Pearson et al.

Open hole tensile tests were conducted by Nixon-Pearson et al. on quasi-isotropic CFRP specimen, with centrally located circular holes. UD carbon fiber-epoxy prepreg system IM7/8552 (Hexcel) was autoclave-cured, and the nominal cured thickness of the plies is 0.125mm. A first campaign was covered in [102], where different geometries and types of scaling were tested. Then, in [109], a new campaign was addressed, which included re-testing some of the previous configurations until failure.

The case study for the SFEM will be the sublaminate-level scaled lay-up $[45/90/-45/0]_{2s}$, for which the ultimate failure mode was found to be fiber pull-out (hence avoiding the modelling of delaminations). The specimen's dimensions were 64x16x2$mm^3$, and the hole diameter 3.175mm. Three batches were manufactured, with significant variability between the test results of the first batch and the subsequent ones. No data exists on the specimen to specimen, or batch to batch, material property variation. Therefore, this example serves to study the effect of different COVs, and correlation parameters, on the predicted mean and variance of ultimate failure. Additionally, it is used to understand how the probabilistic curves of each failure mode and the damage progression will change from the case of section 5.2, which differs in terms of material, lay-up and width to hole diameter ratio.

### 5.3.1. Applying the methodology

**Tests/Assumptions**

The material property means are taken from [96] or assumed based on results. As mentioned, no data exists on the variance of each input. Three different sets of standard deviations will be tested: $\text{COV}_2$, which corresponds to the same coefficients of variations that were used in sections 5.1 and 5.2, $\text{COV}_1$, which halves every COV by 2, and $\text{COV}_3$, which doubles every COV. An exception is made for the in-plane and transverse poisson's ratios, for which the COV is kept constant. The reason for the change is that they have little effect on the output of the model, and further increasing their already significantly high COV led to convergence issues. The inputs of the FE model are listed in table 5.5.

The bounding box solution is again used, due to the computational time advantage. Different correlation parameters will also be tested, with the standard deviations of $\text{COV}_2$. Since previous sections have used $b_{cx} = b_{cy} = 7.35$, the two other values chosen are $b = 0.735$ and $b = 0.0735$. Note that the $\text{COV}_1$

**Table 5.5:** Material properties of IM7/8552

| Property | Mean | $COV_1$[%] | $COV_2$[%] | $COV_3$[%] |
|---|---|---|---|---|
| $E_1$ [GPa] | 171 | 6.4 | 12.8 | 25.6 |
| $E_2$ [GPa] | 9.1 | 11.25 | 22.5 | 45 |
| $\nu_{12}$ | 0.33 | 37.5 | 37.5 | 37.5 |
| $\nu_{23}$ | 0.4 | 33.0 | 33.0 | 33.0 |
| $G_{12}$ [GPa] | 5.3 | 1.25 | 2.5 | 5 |
| $X_T$ [MPa] | 2324 | 3.8 | 7.6 | 15.2 |
| $X_C$ [MPa] | 1200 | 3.8 | 7.6 | 15.2 |
| $Y_{T,embedded}$ [MPa] | 160 | 4.25 | 8.5 | 17 |
| $Y_{T,outer}$ [MPa] | 101 | 4.25 | 8.5 | 17 |
| $Y_C$ [MPa] | 200 | 5.13 | 10.25 | 20.5 |
| $S_{12,embedded}$ [MPa] | 130 | 0.4 | 0.8 | 1.6 |
| $S_{12,outer}$ [MPa] | 107 | 0.4 | 0.8 | 1.6 |
| $\alpha_0$ [°] | 53 | | - | |
| $G_{FFT}$ [N/mm] | 24 | | - | |
| $G_{FFC}$ [N/mm] | 80 | | - | |
| $G_{MFT}$ [N/mm] | 0.1 | | - | |
| $G_{MFC}$ [N/mm] | 0.3 | | - | |
| $\beta$ [$\times 10^{-8}$MPa$^{-3}$] | 2.98 | | - | |

and $COV_3$ models will use the original values.

As for the other stochastic inputs, M must be defined so that error parameters $\bar{\epsilon}_{M,\sigma_w^2}$ and $\epsilon_{M,\sigma_w^2}$ are small enough in all models. Since the bounding box solution is used, and the analytical domain differs from the FE domain, the global error is calculated with equation 3.41. The number of KL terms input is limited by the $COV_3$ and $b = 0.0735$ case, which maximizes the error for a given M. Figure 5.26 shows that, even with $M = 180$, the local error in most of the field is higher than 10%, with $\bar{\epsilon}_{M,\sigma_w^2}$ = 10.2%. The peaks at the edges are of around 22%. The number of KL terms needed to further reduce these errors is unreasonable, so M is taken as 180 for the limit case, and as smaller values when the correlation is higher.

$N_\theta$ will be varied to assure convergence for each model, since it is expected that different COVs and correlation parameters will affect the number of simulations required. Convergence of the mean and standard deviation of $E_1$, at an arbitrary point and for the original inputs, and of $\sigma_s$, for all input variations, is plotted in figures D.5 and D.6.

**Generate Random Fields**

For each combination of COV and $b$, $N_\theta \times$ X 10 X 16 RFs are generated with the bounding box solution of the KL method. Figure 5.27 shows an example of an $E_1$ RF for each variation. The values to which $\sigma_s$ converges with each set of inputs are also given, to understand how both the correlation and the COVs affect the variation within a given lamina.

As expected, increased correlation leads to smaller variation within each specimen. This is evidently also observed when the point-wise standard deviations decrease.

**FE model**

The model from section 4.1 is run with a mesh of 2878 S4 shell elements for each lamina, again with

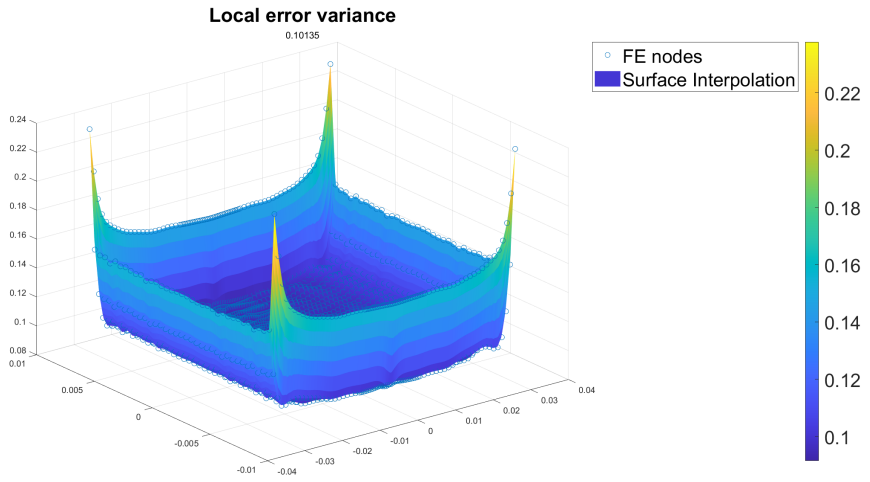


**Figure 5.26:** Local error variance $\epsilon_{M,\sigma_w^2}$ for M=180.

**Figure 5.27:** Examples of E1[GPa] distributions obtained with with the KL expansion and different correlation parameters and COVs.

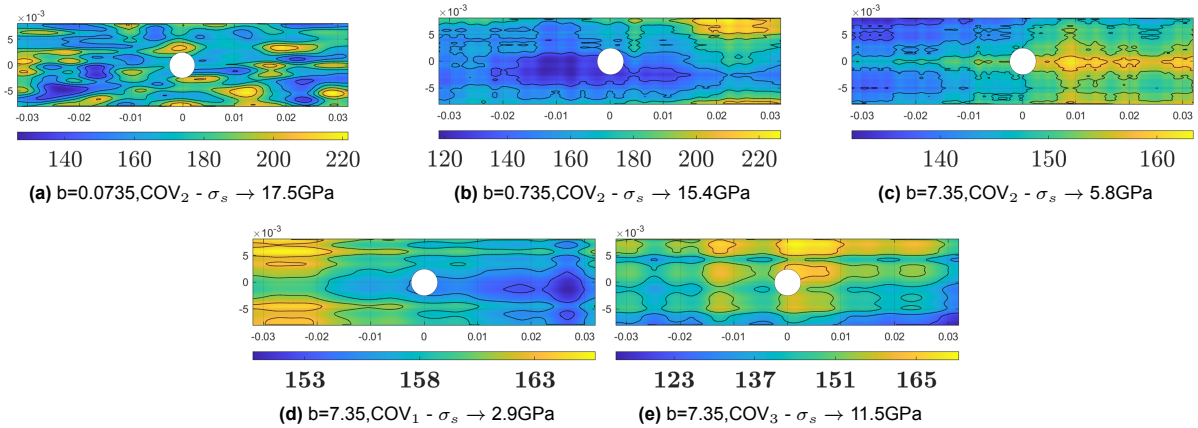


**(a)** b=0.0735,COV$_2$ - $\sigma_s \rightarrow$ 17.5GPa **(b)** b=0.735,COV$_2$ - $\sigma_s \rightarrow$ 15.4GPa **(c)** b=7.35,COV$_2$ - $\sigma_s \rightarrow$ 5.8GPa

**(d)** b=7.35,COV$_1$ - $\sigma_s \rightarrow$ 2.9GPa **(e)** b=7.35,COV$_3$ - $\sigma_s \rightarrow$ 11.5GPa

a much higher density near the hole, where failure is expected to occur. The model and boundary conditions are represented in figure 5.28.

The deterministic model predicts ultimate failure at 20.475kN. The effect of the mesh density on this value is detailed in table D.3. Initially there is MFT in the $90°$ plies, followed by FFT in the $0°$ plies. Then MFT in the outer plies ($45°$) and the remaining $\pm 45°$ ones soon after. Finally, closer to LPF there is simultaneous tensile fiber damage onset in the $\pm 45°$ plies. This damage progression is similar to the one from section 5.2, with the exception that $0°$ ply FFT precedes matrix tensile damage in the $\pm 45°$ laminae.

The damage pattern of the matrix cracking in the $-45°$ plies is shown in figure 5.29. Figures 5.30a and 5.30b were obtained for two different (inner and outer) $-45°$ laminae in one of the 200 stochastic simulations. Similar conclusions to those of section 5.2 can be made. The damage progression is similar in all cases: a general tendency for crack growth in the transverse direction to the fibers, with smearing instead of a discrete crack being formed. Again, it is the extent and specific location of failure that varies with each simulation and lamina - for the outer $90°$ ply, MFT has extended beyond that of the deterministic model, while less elements are damaged in the inner one.

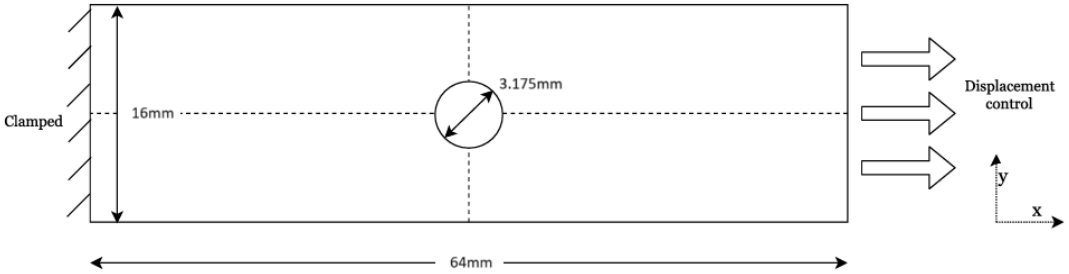


**Figure 5.28:** Model and boundary conditions for Nixon-Pearson et al. case study (adapted from [96]).

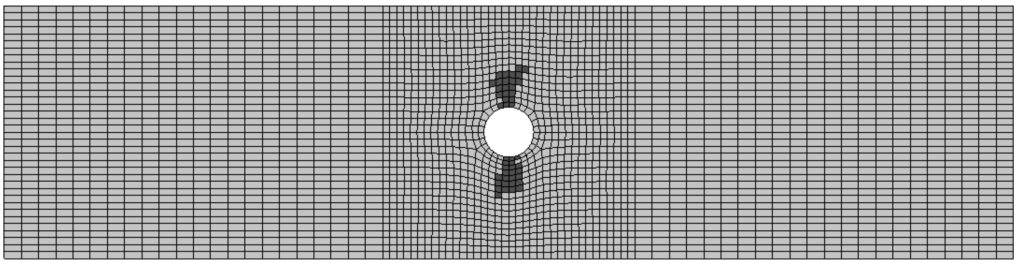

**Figure 5.29:** Progression of matrix tensile failure in $-45^\circ$ plies - applied load 20kN, in deterministic model.

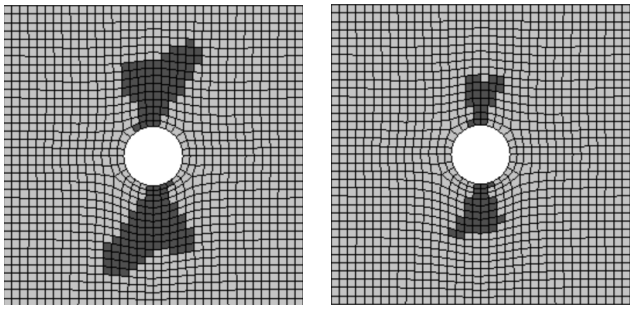

**(a)** Outer $-45^\circ$ ply. **(b)** Inner $-45^\circ$ ply.

**Figure 5.30:** Progression of matrix tensile failure in -45° plies - applied load 20kN, in stochastic model, arbitrarily chosen random case.

## 5.3.2. Results and Discussion

All results were assumed to follow gaussian distributions (based on the results of section 5.1). First, the failure mode CDFs, obtained with the same COVs and b ($COV_2$, b=7.35) as the first two test cases, are shown in figure 5.31.

The same observations can be made regarding this graph as in section 5.2 - the probabilistic curves of the damage modes follow the same order as the deterministic results. Another aspect of the plots that is of interest is the variance of the values for each type of failure. The MFT curves, more influenced by variables $E_2$ and $Y_T$, have the highest standard deviations, which should be expected, since these material properties have a higher input COV than $E_1$ and $X_T$, which influence FFT. The agreeance of this aspect of the results with the inputs further validates the proposed SFEM and shows its reliability in propagating material uncertainties.

For the same stochastic inputs, the spatial distribution of the probability of MFT in a -45° ply, with 20kN of applied load, is plotted in figure 5.32. The equivalent plots for the other plies are shown in appendix D (figures D.7 and D.8).

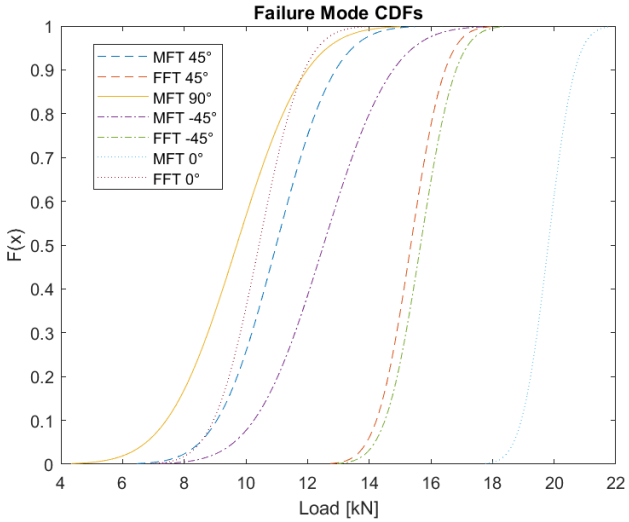


**Figure 5.31:** Damage initiation CDFs - normal distributions fitted to the Larc05 damage mode initiation loads, obtained with b=7.35 and $COV_2$. There is MFT in all plies, as well as FFT in the 0° and $\pm 45°$ plies.

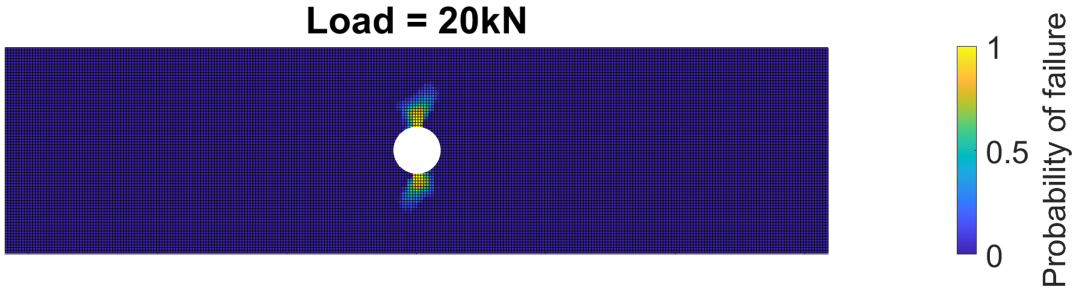


**Figure 5.32:** Probability of MFT in a -45° ply with 20kN applied load, throughout the specimen.

Comparing this plot to figure 5.25, the elements with higher probabilities of failure are more concentrated in one direction. The smearing of the damage also seems to be less extensive than in the examples shown in figure 5.30, showing that the CDM on average predicts matrix cracking to happen from the hole and symmetrically, despite different pattern variations in every simulation. The predicted pattern seems, again, unrealistic, as cracks have been observed experimentally to grow along the fibers [8].

In figure 5.33, the CDFs of normal distributions, fitted to ultimate failure loads obtained with the three different sets of COVs, are plotted.

First, as expected, the increase of input standard deviations results in a higher variance of the ultimate failure results. More interesting is the change of the mean with this same increase. As in sections 5.1 and 5.2, the average of the stochastic model values is lower than the deterministic results. A higher input variance increases that offset, with the $COV_3$ plot shifting the most to the left. A possible explanation is that a higher standard deviation exacerbates the effect of low strength areas causing failure.

In figure 5.34, the CDFs of normal distributions, fitted to ultimate failure loads obtained with the three different correlation parameter values, are plotted.

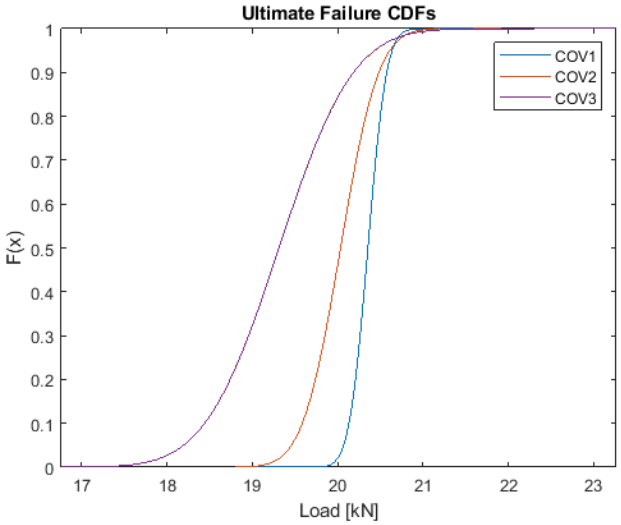


**Figure 5.33:** Ultimate failure CDFs - normal distributions fitted to the results of proposed method, obtained with three different sets of COV inputs (listed in table 5.5).

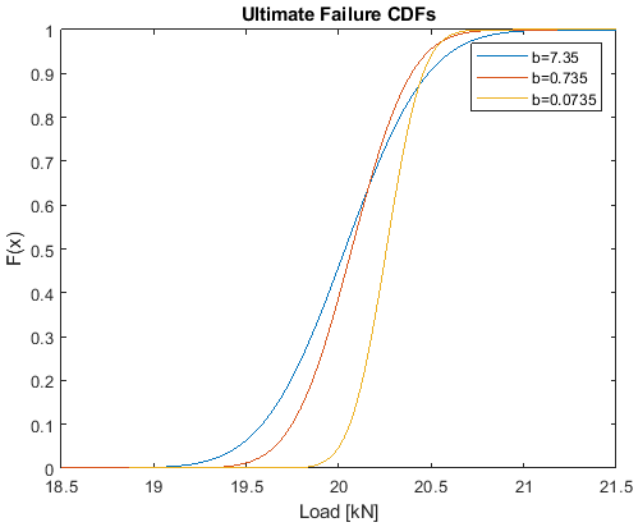


**Figure 5.34:** Ultimate failure CDFs - normal distributions fitted to the results of proposed method, obtained with three different correlation parameter inputs (listed in table 5.5).

It can be observed that an increase in correlation leads to an increase in the variance of the results, as well as a decrease of the mean. The increased variance could have been predicted, since this is the same effect found in sections 5.1 and 5.2: the random MC fields, which can be thought of as the ”limit case” of lowering the correlation in the KL expansion (every point is completely uncorrelated), led to the lowest standard deviation of ultimate failure results in both cases.

Table 5.6 summarizes the ultimate failure results. The change in output standard deviation for each COV input is almost linear, doubling each time the COVs are doubled. The means, however, decrease in a less predictable way: -0.6%, -2.17% and -5.16% for $COV_1$, $COV_2$ and $COV_3$, respectively. The sensitivity to the correlation parameter is much smaller, with a 100x difference decreasing the standard deviation by only 58%. The experimental values are also presented. While the variance between all batches is higher than every option presented, which may have been caused by inadvertent changes in the setups of both experimental campaigns, the one for each batch is quite similar and includes the $COV_2$ and $COV_3$ results in its confidence interval. This suggests that, with data on material property uncertainty, it could be possible to approximate the uncertainty of failure values with relative accuracy,

using the proposed SFEM.

**Table 5.6:** SFEM results - Nixon-Pearson et. Al case study. Values in parenthesis represent the 95% confidence intervals.

| Model | Mean [kN] | Standard Deviation [kN] |
|---|---|---|
| Deterministic model | 20.475 | - |
| Proposed SFEM ($COV_1$,b=7.35) | 20.36 | 0.17 |
| Proposed SFEM ($COV_2$,b=7.35) | 20.03 | 0.35 |
| Proposed SFEM ($COV_3$,b=7.35) | 19.31 | 0.68 |
| Proposed SFEM ($COV_2$,b=0.735) | 20.07 | 0.25 |
| Proposed SFEM ($COV_3$,b=0.0735) | 20.26 | 0.15 |
| Experimental fit (all batches) | 17.22 (16.48-17.96) | 1.34 (0.98-2.12) |
| Experimental fit (1st batch) | 15.98 (15.37-15.69) | 0.58 (0.36-1.42) |
| Experimental fit (2nd batch) | 18.77 (18.05-19.50) | 0.58 (0.35-1.67) |
| Experimental fit (3rd batch) | 17.14 (16.27-18.01) | 0.55 (0.31-2.05) |

Figures 5.35 and 5.36 plot the convergence of the mean and standard deviation of the ultimate failure CDFs, obtained with each set of COVs. Convergence seems to be slower for higher input variances. However, even for the $COV_3$ results, the standard deviation has converged for around 130 simulations.

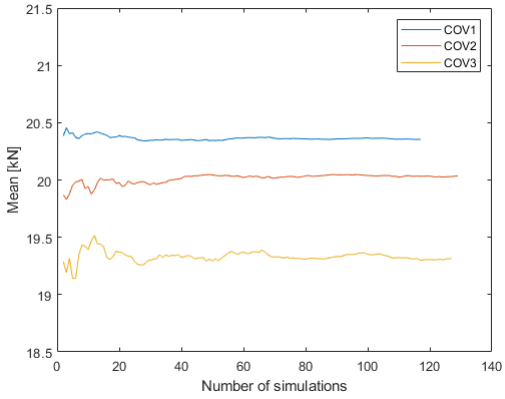


**Figure 5.35:** Change in mean [kN] of ultimate failure probabilistic distributions with increase of the number of simulations.

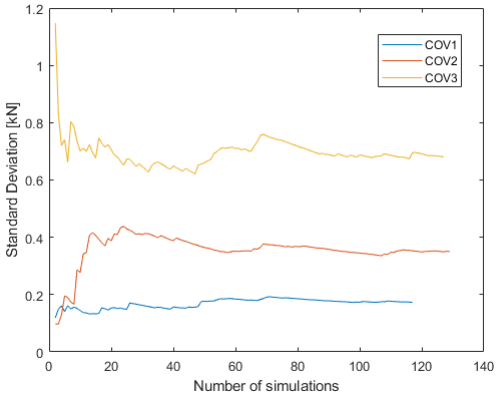


**Figure 5.36:** Change in standard deviation [kN] of ultimate failure probabilistic distributions with increase of the number of simulations.

## 5.4. Conclusions

In section 4.3, a summary of the steps involved in the proposed SFEM was presented. The two main parts of that methodology are described in detail in sections 3 and 4.1, with the summary further describing how they are connected in a loop to generate the stochastic results. The steps of this methodology were then put into practice with three examples of applications.

In the test case of section 5.1, the sets of ultimate failure results, both experimental and from the proposed SFEM, were fitted with different probabilistic distributions. It was found that all of them provide acceptable approximations, with only Weibull having a lower p-level in one of the cases, which means assuming a Normal distribution is possible and supported by data. The ultimate failure CDFs indicated that using the KL expansion results in a higher output variance than when correlation is not considered, which better represents the variance in experimental values. No significant difference existed between

the Hashin and Larc05 criteria and all stochastic model curves had significantly lower means than the deterministic model prediction. Finally, convergence was achieved after about 100 simulations, with the 2D distributions of failure probability converging to an average value, constant in the domain.

In the Van Dongen et al. test case (section 5.2), the Random MC method, where a value is sampled at each integration point, with no spatial correlation, resulted again in an underestimation of the variance, unlike the KL expansion methods. On the other hand, Larc05 and Hashin initiation criteria did not affect the curves significantly. The difference between the mean of the CDFs and the deterministic prediction was, in this case, smaller. Finally, after only 50 simulations, the results converged, with the spatial distribution of failure probability converging to the deterministic pattern. Regarding the failure mode CDFs, the stochastic progression of failure followed the same order as in the deterministic model, with some added probability of matrix cracking in the $0^\circ$ plies. The failure mode CDFs with the highest variance were for MFT, since the transverse material properties had the highest input variance.

The last test case helped understand the sensitivity of results to the stochastic inputs. It was found that increasing the input COVs results in a higher output variance, as well as a lower average failure load. Increasing the correlation parameters led to a higher output variance, and seemed to also slightly decrease the mean, although to a lesser extent.

Overall, the proposed methodology resulted in acceptable reliability predictions, which were positively validated by admittedly limited experimental results. This is especially true regarding the standard deviation of the fitted CDFs, while the decrease of the mean in the 1st test case suggests the method may lead to overly conservative results. It is also true, however, that using the KL expansion to generate the RFs led to results that much better match the variability that was found in the experimental campaigns that when correlation was ignored. The damage patterns and progressive failure captured by the stochastic model matched the inputs and the deterministic models. This again suggests the proposed methodology is able to capture specimen variability, while still converging, within just a few hundred simulations, to the average or deterministic results. So despite the CDM predicting damage patterns that cannot validated by experiments, the stochastic methodology is further validated by the sound relation between the deterministic and probabilistic results.

# 6

# Conclusions and Recommendations

The present study aimed to develop an improved SFEM framework for composite reliability analysis. The purpose of adding a stochastic nature to FEM failure predictions is to better represent the scatter commonly observed in experimental results. Model uncertainties are incorporated so that failure is represented not as a single value, but as a probabilistic curve that could explain the aforementioned scatter. After the literature study, the framework was defined further: the proposed method was to incorporate RFs of material properties, generated with the KL expansion, and LHS, with FEM simulations being run in Abaqus to generate failure statistics. The KL expansion was expected to improve current generally applicable methods in the sense that the representation of uncertainties would be more realistic, generating RFs that obey a certain covariance function. Additionally, LHS was expected to result in better efficiency than MC sampling methods. Such a methodology had not before been applied to complex cases, such as OHT.

In section 3, the RF discretization methodology was explored, with two solutions of the KL expansion being compared. It was found that, although most literature focuses on the galerkin discretization method, the simpler approach of taking an analytical solution around the FE mesh can achieve similar results. Although it may not be ideal for all geometries, this approach seems to work as well as the alternatives for cases such as a notched laminate, and has the added benefit of simplicity and computational efficiency. However, if different covariance functions are to be implemented, which may be necessary to model a property with a non-gaussian distribution, the galerkin methodology should be used. Finally, results showed the faster convergence of sampled values that is obtained when using LHS instead of MC.

In section 4, the different steps of the SFEM methodology were explained. A CDM approach (implemented through a UMAT subroutine) was chosen, as other, more complicated, modelling techniques would be too costly in the computational sense. The main limitations of the approach were listed: it has been found to predict the growth of matrix cracks in an unrealistic way, not respecting fiber-matrix heterogeneity; it does not model delaminations, which are a significant failure mode in many cases. In the context of the present study, the CDM was considered a good compromise that would allow sufficient validation of the stochastic methodology. This validation, was, however, limited to test cases were delaminations were not found to be significant.

In section 5, the methodology was tested with three case studies. Different probabilistic distributions were fitted to the ultimate failure loads (experimental and predicted), and it was found that three out of four distributions (normal, lognormal and gamma) provided equally good approximations. Normal distributions were then assumed for all test cases. The CDFs resulting from the proposed methodology were compared with others: the experimental CDF, one obtained with the same methodology but RFs generated with Random MC sampling at each integration point, and another resulting from the same methodology but Hashin failure criteria instead of Larc05. It was found that the methods that used the KL expansion resulted in distributions that were the most similar to the empirical ones. The Random MC method under-predicted the variance for both cases, while the other CDFs had standard deviations

within the 95% confidence interval. The Random MC variance was over 10x smaller for a simple plate in uni-axial tension, and about half of the KL variance for the OHT test case. Despite this, the mean of the stochastic failure loads was lower than the deterministic prediction, which in the first test case made the probabilistic predictions overly conservative. Both failure criteria that were tested resulted in acceptable and similar (within 6% of difference) predictions. Maximum loads, based on a target reliability of 0.9999, were calculated by inverting each CDF. The maximum load calculated with a safety factor of 1.5 was shown to be significantly more conservative than the others.

The 3D failure probability plots showed that the stochastic results respond to the inputs in a predictable way, converging to the same patterns and progression of damage as the deterministic prediction, but in probabilistic form - the proposed methodology can reliably use a deterministic damage model to provide probabilistic progressive failure predictions.

Different correlation parameters and COVs were tested for a single model, with the following conclusions: an increase in COV leads to a reduction in the average of the stochastic failure loads, while evidently increasing their standard deviation; an increase in correlation leads to an increase in standard deviation, and small decrease of the mean. Possible explanations for all these observations were given. First, when the variance within each RF is high due to less correlation, the variance between different RFs and random cases is smaller. Additionally, the mean of stochastic datasets is always smaller than the deterministic prediction, since spatial variation causes each lamina to fail at a weaker-than-average region. This effect is, as should be expected, more significant when failure is less localized (plate in uni-axial tension test case) and when the variance is higher. Finally, results obtained with the proposed methodology converge relatively fast (for the test cased within 200 simulations), the speed increasing with the decrease of the standard deviation.

All these observations showed the very significant impact of material property uncertainty on the reliability of the structure, with the input standard deviation having a direct relation with the standard deviation of the failure CDF. The correlation of the fields was also shown to have a significant impact, especially on the variance of the stochastic failure loads, which shows the importance of adequately determining these parameters.

## 6.1. Answering the Research Questions

The research questions defined in section 2 are now answered directly. First, three sub-questions were listed that will contribute to answering the main one:

What strategies for generating random fields and obtaining the response can be used to make a general-purpose SFEM as computationally efficient and reliable as possible?

General-purpose SFEM implementations, as identified in the Literature Review, are limited to sampling MC procedures, either random at each point or with random field discretization procedures such as the KL expansion. The latter option considers spatial correlation of material properties, and this was shown to have a very significant impact in the results, with up to 13x difference in the output variance of both methods. The variance predicted with RFs generated with the KL expansion was found to be closer to the experimental observations, so this strategy can be considered to make the SFEM more reliable and accurate.

Additionally, LHS was found to be a more efficient sampling strategy than MCS, since the mean and variance of the sampled random properties at each point converge to their targets faster when LHS is used. This reduces the number of simulations that the SFEM requires for its results to converge.

What failure criteria give the most accurate results with the SFEM?

Only 2 criteria were tested, Hashin and Larc05, and both gave similar results, within the confidence intervals of experimental values. Therefore, this question cannot be confidently answered based on the present work. However, results suggest the stochastic inputs and methodology have a larger effect on the SFEM output than the failure criterion itself, which may mean the latter can be chosen based on deterministic FEM considerations.

How do the experimental results compare with the SFEM predictions?

Even with often limited information on the stochastic inputs, SFEM results generally compared well with experiments, especially in terms of the standard deviation, which was found in most cases to be within the 95% confidence interval of the experimental value. The deterministic FEM, which was not the focus of the project, also gave good approximations of the average of ultimate failure values, although it was often unconservative. The mean of the SFEM results is always smaller than the deterministic output, which in one of the cases led to overly conservative predictions. Both the correlation parameters and input variance were found to have significant impact in the mean of stochastic results.

So, finally:

**To what extent can the SFEM be used to predict the reliability and probabilistic damage evolution of composite laminates with geometric details and spatially varying properties?**

The proposed stochastic methodology shows great potential for reliability analysis of composite structures, including applications of complex analysis such as the OHT case. First, its ultimate failure and reliability results more often than not agreed well with experiments, capturing the experimental variability with good accuracy. Secondly, the SFEM was shown to be able to predict maximum loads based on a target reliability, for both FPF and LPF, with these loads being less conservative than those obtained with a safety factor design strategy. Thirdly, it showed better accuracy and efficiency than other existing implementations, with convergence requiring less than 100 simulations in some cases, depending on the specimen and input COVs. In fourth place, its non-intrusive nature and generic formulations makes it very practical and user-friendly, with the deterministic FEM component being interchangeable with any software or alternative modelling strategies.

Finally, results suggest a methodology such as the one presented can reliably be used to predict element-by-element and ply-by-ply damage evolution in a progressive way, based on a deterministic damage model. This means that, depending on the accuracy of the deterministic model, the SFEM could be used to understand how different mechanisms, such as matrix cracking or delaminations, occur throughout a specimen in a stochastic way.

However, some limitations still exist. Depending on the application, the results may still be too conservative, and so adjustments, for example to the correlation parameter calculations, may be necessary to guarantee this does not occur. Additionally, the deterministic FEM component as presented in this study leads to unrealistic damage patterns and often unconservative predictions, so validation of the methodology with improved strategies is suggested.

## 6.2. Recommendations for future work

The following lines of research are recommend for future work on this topic:

- **Further validation of proposed SFEM methodology**: the framework was tested with only two different types of laminate, so other, more complex quasi-static load cases and 2D geometries could be assessed; a more extensive experimental campaign, to obtain both the stochastic inputs and failure CDFs with high degrees of certainty, is needed for true validation; other types of uncertainty modelling should be tested, including different probabilistic distributions, different random variables related to geometry and loading, and epistemic uncertainty considerations.
- **Extending framework to other types of loading**: besides quasi-static, other types of analysis could be performed, such as fatigue or dynamic.
- **Extending framework to 3D geometries**: currently the method and code implementation are only applicable to 2D geometries, but several cases of interest for reliability analysis require an extension of the KL implementation, such as stiffened panels.
- **Developing a surrogate model**: the proposed methodology will likely by unfeasible for meshes with a very large number of elements, or for a laminate with a large number number of plies, due to the excessive computational time; a surrogate model that can replace the FEM solver after only a few simulations would solve this issue, although it could be complex to integrate it with a progressive damage model.

# References


[1] Jens Bachmann, Carme Hidalgo, and Stéphanie Bricout. “Environmental analysis of innovative sustainable composites with potential use in aviation sector—A life cycle assessment review”. In: *Science China Technological Sciences* 60 (Aug. 2017). DOI: 10.1007/s11431-016-9094-y.

[2] Yingjie Xu et al. “A review on the design of laminated composite structures: constant and variable stiffness design and topology optimization”. In: *Advanced Composites and Hybrid Materials* 1 (Sept. 2018). DOI: 10.1007/s42114-018-0032-7.

[3] Om Kumar. “A Review on Composites: Selection and its Applications”. In: Aug. 2023.

[4] R. O’Higgins et al. “Experimental and Numerical Study of the Open-Hole Tensile Strength of Carbon/Epoxy Composites”. In: *Mechanics of Composite Materials* 40 (July 2004), pp. 269–278. DOI: 10.1023/B:MOCM.0000039744.98869.0d.

[5] Christos Nastos and Dimitrios Zarouchas. “Probabilistic failure analysis of quasi-isotropic CFRP structures utilizing the stochastic finite element and the Karhunen–Loève expansion methods”. In: *Composites Part B: Engineering* 235 (Apr. 2022), p. 109742. ISSN: 1359-8368. DOI: 10.1016/j.compositesb.2022.109742. URL: https://www.sciencedirect.com/science/article/pii/S1359836822001251 (visited on 03/05/2024).

[6] “Review of Laminate Strength and Failure Criteria”. In: *Design and Analysis of Composite Structures*. John Wiley & Sons, Ltd, 2013. Chap. 4, pp. 55–63. ISBN: 9781118536933. DOI: https://doi.org/10.1002/9781118536933.ch4. eprint: https://onlinelibrary.wiley.com/doi/pdf/10.1002/9781118536933.ch4. URL: https://onlinelibrary.wiley.com/doi/abs/10.1002/9781118536933.ch4.

[7] Ramesh Talreja. “Multiscale failure assessment of composite laminates”. In: Dec. 2016, pp. 349–355. ISBN: 9781782422860. DOI: 10.1016/B978-1-78242-286-0.00015-7.

[8] Björn Dongen, Alexander Oostrum, and Dimitrios Zarouchas. “A blended continuum damage and fracture mechanics method for progressive damage analysis of composite structures using XFEM”. In: *Composite Structures* 184 (Oct. 2017). DOI: 10.1016/j.compstruct.2017.10.007.

[9] Robert Coenen. “A hybrid approach to implement the Digital Twin concept into a damage evolution prediction for composite structures”. en. In: (2021). URL: https://repository.tudelft.nl/islandora/object/uuid%3A27e1ac12-5cdb-4154-abcd-3358d244fab4 (visited on 03/05/2024).

[10] Xiaodong Wang et al. “An accurate and easy to implement method for predicting matrix crack and plasticity of composites with an efficient search algorithm for LaRC05 criterion”. In: *Composites Part A: Applied Science and Manufacturing* 131 (Feb. 2020), p. 105808. DOI: 10.1016/j.compositesa.2020.105808.

[11] James D. Lee. “Three dimensional finite element analysis of damage accumulation in composite laminate”. In: *Computers & Structures* 15.3 (Jan. 1982), pp. 335–350. ISSN: 0045-7949. DOI: 10.1016/0045-7949(82)90026-8. URL: https://www.sciencedirect.com/science/article/pii/0045794982900268 (visited on 04/29/2024).

[12] C. Mccarthy, Michael McCarthy, and V.P. Lawlor. “Progressive damage analysis of multi-bolt composite joints with variable bolt-hole clearance”. In: *Composites Part B: Engineering* 36 (June 2005), pp. 290–305. DOI: 10.1016/j.compositesb.2004.11.003.

[13] P. P. Camanho and F. L. Matthews. “A Progressive Damage Model for Mechanically Fastened Joints in Composite Laminates”. en. In: *Journal of Composite Materials* 33.24 (Dec. 1999). Publisher: SAGE Publications Ltd STM, pp. 2248–2280. ISSN: 0021-9983. DOI: 10.1177/002199839903302402. URL: https://doi.org/10.1177/002199839903302402 (visited on 04/29/2024).

[14] Libin Zhao et al. “3D Gradual Material Degradation Model for Progressive Damage Analyses of Unidirectional Composite Materials”. In: *Mathematical Problems in Engineering* 2015 (May 2015), pp. 1–11. DOI: 10.1155/2015/145629.

[15] Zdenek Bazant and Byung Oh. “Crack Band Theory for Fracture of Concrete”. In: *Matériaux et Constructions* 16 (May 1983), pp. 155–177. DOI: 10.1007/BF02486267.

[16] Mustafa Kulekci, Ibrahim Sevim, and Ugur Esme. “Fracture Toughness of Friction Stir-Welded Lap Joints of Aluminum Alloys”. In: *Journal of Materials Engineering and Performance - J MATER ENG PERFORM* 21 (July 2012). DOI: 10.1007/s11665-011-0017-y.

[17] M.L. Benzeggagh and M. Kenane. “Measurement of mixed-mode delamination fracture toughness of unidirectional glass/epoxy composites with mixed-mode bending apparatus”. In: *Composites Science and Technology* 56.4 (1996), pp. 439–449. ISSN: 0266-3538. DOI: https://doi.org/10.1016/0266-3538(96)00005-X. URL: https://www.sciencedirect.com/science/article/pii/026635389600005X.

[18] Edward M. Wu, Jr. Reuter, and R. C. “CRACK EXTENSION IN FIBERGLASS REINFORCED PLASTICS:” in: Fort Belvoir, VA: Defense Technical Information Center, Feb. 1965. DOI: 10.21236/AD0613576. URL: http://www.dtic.mil/docs/citations/AD0613576 (visited on 04/30/2024).

[19] Peng Zhang et al. “Modelling distinct failure mechanisms in composite materials by a combined phase field method”. In: *Composite Structures* 232 (2020), p. 111551. ISSN: 0263-8223. DOI: https://doi.org/10.1016/j.compstruct.2019.111551. URL: https://www.sciencedirect.com/science/article/pii/S0263822319323852.

[20] Lucas Amaro de Oliveira and Mauricio Donadon. “Delamination analysis using cohesive zone model: A discussion on traction-separation law and mixed-mode criteria”. In: *Engineering Fracture Mechanics* 228 (Feb. 2020), p. 106922. DOI: 10.1016/j.engfracmech.2020.106922.

[21] T. W. De Jong. *Forming of Laminates*. English. IOS Press, Jan. 2004. ISBN: 978-90-407-2506-7.

[22] M. Naderi and M.M. Khonsari. “Stochastic analysis of inter- and intra-laminar damage in notched PEEK laminates”. English. In: *Express Polymer Letters* 7.4 (2013), pp. 383–395. ISSN: 1788-618X. DOI: 10.3144/expresspolymlett.2013.35.

[23] E.J. Pitz and K.V. Pochiraju. “Quasi Monte Carlo simulations for stochastic failure analysis in composites”. English. In: 2019. ISBN: 978-1-60595-602-2. DOI: 10.12783/asc34/31406.

[24] F.H. Bhuiyan and R.S. Fertig III. “Stochastic fiber failure prediction of composite open-hole tension coupons under fatigue loading using a physics-based methodology”. English. In: 2018. ISBN: 978-1-62410-532-6. DOI: 10.2514/6.2018-0969.

[25] F.H. Bhuiyan and R.S. Fertig. “A PFA methodology to investigate UD composites in fatigue comprising a KTF-based model for matrix damage and stochastic fiber failure prediction”. English. In: *Composite Structures* 279 (2022). ISSN: 0263-8223. DOI: 10.1016/j.compstruct.2021.114724.

[26] M.L. Kirby, D.S. Riha, and M.L. Stanfield. “PROBABILISTIC SENSITIVITY STUDIES OF OPEN-HOLE TENSION COMPOSITE DAMAGE MODELS”. English. In: vol. 2022-May. 2022. ISBN: 978-1-934551-41-7.

[27] Michael Ballard et al. “An Extended Critical Failure Volume Method for Strength Prediction in 3D Woven Textile Composites”. In: Jan. 2022. DOI: 10.2514/6.2022-2597.

[28] Son Pham and Ba Nguyen. “Application of the Finite Element Method Using Cohesive Elements to Model the Effect of Temperature, Rock Mechanical Properties, Fluid Injection Rate, and Fluid Properties on the Development of Hydraulic Fracture Height”. In: *Modelling and Simulation in Engineering* 2022 (May 2022), pp. 1–19. DOI: 10.1155/2022/7413457.

[29] Jingwei Ying and Jin Guo. “Fracture Behaviour of Real Coarse Aggregate Distributed Concrete under Uniaxial Compressive Load Based on Cohesive Zone Model”. In: *Materials* 14 (Aug. 2021), p. 4314. DOI: 10.3390/ma14154314.

[30] J. Jokinen and M. Kanerva. “Simulation of Delamination Growth at CFRP-Tungsten Aerospace Laminates Using VCCT and CZM Modelling Techniques”. en. In: *Applied Composite Materials* 26.3 (June 2019), pp. 709–721. ISSN: 1573-4897. DOI: 10.1007/s10443-018-9746-5. URL: https://doi.org/10.1007/s10443-018-9746-5 (visited on 05/01/2024).

[31] Xin Lu et al. “On Cohesive Element Parameters and Delamination Modelling”. In: *Engineering Fracture Mechanics* 206 (Dec. 2018). DOI: 10.1016/j.engfracmech.2018.12.009.

[32] Ireneusz Lapczyk and Juan Hurtado. “Progressive damage modeling in fiber-reinforced materials”. In: *Composites Part A: Applied Science and Manufacturing* 38 (Nov. 2007), pp. 2333–2341. DOI: 10.1016/j.compositesa.2007.01.017.

[33] E.F. Rybicki and M.F. Kanninen. “A finite element calculation of stress intensity factors by a modified crack closure integral”. In: *Engineering Fracture Mechanics* 9.4 (1977). Cited by: 2078, pp. 931–938. DOI: 10.1016/0013-7944(77)90013-3. URL: https://www.scopus.com/inward/record.uri?eid=2-s2.0-0017561766&doi=10.1016%2f0013-7944%2877%2990013-3&partnerID=40&md5=96afbdc537213c39b0f79892b2479cbf.

[34] David A. Dillard. “13 - Improving adhesive joint design using fracture mechanics”. In: *Advances in Structural Adhesive Bonding*. Ed. by David A. Dillard. Woodhead Publishing in Materials. Woodhead Publishing, Jan. 2010, pp. 350–388. ISBN: 978-1-84569-435-7. DOI: 10.1533/9781845698058.3.350. URL: https://www.sciencedirect.com/science/article/pii/B9781845694357500134 (visited on 05/01/2024).

[35] J. A. Pascoe, R. C. Alderliesten, and R. Benedictus. “Methods for the prediction of fatigue delamination growth in composites and adhesive bonds – A critical review”. In: *Engineering Fracture Mechanics* 112-113 (Nov. 2013), pp. 72–96. ISSN: 0013-7944. DOI: 10.1016/j.engfracmech.2013.10.003. URL: https://www.sciencedirect.com/science/article/pii/S0013794413003214 (visited on 05/01/2024).

[36] M. Shahverdi, A. P. Vassilopoulos, and T. Keller. “12 - Simulating the effect of fiber bridging and asymmetry on the fracture behavior of adhesively-bonded composite joints”. In: *Fatigue and Fracture of Adhesively-Bonded Composite Joints*. Ed. by A. P. Vassilopoulos. Woodhead Publishing, Jan. 2015, pp. 345–367. ISBN: 978-0-85709-806-1. DOI: 10.1016/B978-0-85709-806-1.00012-4. URL: https://www.sciencedirect.com/science/article/pii/B9780857098061000124 (visited on 05/01/2024).

[37] R. Krueger. “1 - The virtual crack closure technique for modeling interlaminar failure and delamination in advanced composite materials”. In: *Numerical Modelling of Failure in Advanced Composite Materials*. Ed. by Pedro P. Camanho and Stephen R. Hallett. Woodhead Publishing Series in Composites Science and Engineering. Woodhead Publishing, Jan. 2015, pp. 3–53. ISBN: 978-0-08-100332-9. DOI: 10.1016/B978-0-08-100332-9.00001-3. URL: https://www.sciencedirect.com/science/article/pii/B9780081003329000013 (visited on 05/01/2024).

[38] Manuel Chiachio, Juan Chiachio, and Guillermo Rus. “Reliability in composites – A selective review and survey of current development”. In: *Composites Part B: Engineering* 43.3 (Apr. 2012), pp. 902–913. ISSN: 1359-8368. DOI: 10.1016/j.compositesb.2011.10.007. URL: https://www.sciencedirect.com/science/article/pii/S1359836811004549 (visited on 03/05/2024).

[39] José David Arregui-Mena, Lee Margetts, and Paul M. Mummery. “Practical Application of the Stochastic Finite Element Method”. en. In: *Archives of Computational Methods in Engineering* 23.1 (Mar. 2016), pp. 171–190. ISSN: 1886-1784. DOI: 10.1007/s11831-014-9139-3. URL: https://doi.org/10.1007/s11831-014-9139-3 (visited on 03/07/2024).

[40] George Stefanou. “The stochastic finite element method: Past, present and future”. In: *Computer Methods in Applied Mechanics and Engineering* 198.9 (Feb. 2009), pp. 1031–1051. ISSN: 0045-7825. DOI: 10.1016/j.cma.2008.11.007. URL: https://www.sciencedirect.com/science/article/pii/S0045782508004118 (visited on 03/08/2024).

[41] G. Van Vinckenroy and W. P. de Wilde. “The use of Monte Carlo techniques in statistical finite element methods for the determination of the structural behaviour of composite materials structural components”. In: *Composite Structures*. Eighth International Conference on Composite Structures 32.1 (Jan. 1995), pp. 247–253. ISSN: 0263-8223. DOI: 10.1016/0263-8223(95)00055-0. URL: https://www.sciencedirect.com/science/article/pii/0263822395000550 (visited on 03/13/2024).

[42] P. F. Liu and J. Y. Zheng. “Strength reliability analysis of aluminium–carbon fiber/epoxy composite laminates”. In: *Journal of Loss Prevention in the Process Industries* 23.3 (May 2010), pp. 421–427. ISSN: 0950-4230. DOI: 10.1016/j.jlp.2010.02.002. URL: https://www.sciencedirect.com/science/article/pii/S0950423010000215 (visited on 03/06/2024).

[43] D. J. Lekou and T. P. Philippidis. “Mechanical property variability in FRP laminates and its effect on failure prediction”. In: *Composites Part B: Engineering* 39.7 (Oct. 2008), pp. 1247–1256. ISSN: 1359-8368. DOI: 10.1016/j.compositesb.2008.01.004. URL: https://www.sciencedirect.com/science/article/pii/S1359836808000097 (visited on 03/06/2024).

[44] Christos Nastos, Panagiotis Komninos, and Dimitrios Zarouchas. “Non-destructive strength prediction of composite laminates utilizing deep learning and the stochastic finite element methods”. In: *Composite Structures* 311 (May 2023), p. 116815. ISSN: 0263-8223. DOI: 10.1016/j.compstruct.2023.116815. URL: https://www.sciencedirect.com/science/article/pii/S0263822323001599 (visited on 03/05/2024).

[45] Srinivas Sriramula and Marios K. Chryssanthopoulos. “Quantification of uncertainty modelling in stochastic analysis of FRP composites”. In: *Composites Part A: Applied Science and Manufacturing* 40.11 (Nov. 2009), pp. 1673–1684. ISSN: 1359-835X. DOI: 10.1016/j.compositesa.2009.08.020. URL: https://www.sciencedirect.com/science/article/pii/S1359835X09002577 (visited on 03/11/2024).

[46] J. Zhi and T.-E. Tay. “Computational structural analysis of composites with spectral-based stochastic multi-scale method”. English. In: *Multiscale and Multidisciplinary Modeling, Experiments and Design* 1.2 (2018), pp. 103–118. ISSN: 2520-8179. DOI: 10.1007/s41939-018-0009-9.

[47] P. D. Spanos and A. Kontsos. “A multiscale Monte Carlo finite element method for determining mechanical properties of polymer nanocomposites”. In: *Probabilistic Engineering Mechanics*. Dedicated to Professor Ove Ditlevsen 23.4 (Oct. 2008), pp. 456–470. ISSN: 0266-8920. DOI: 10.1016/j.probengmech.2007.09.002. URL: https://www.sciencedirect.com/science/article/pii/S0266892008000271 (visited on 03/08/2024).

[48] Vahid Yavari and Mohammad Hassan Kadivar. “Application of stochastic finite element method in estimation of elastic constants for NCF composites”. In: *Mechanics Research Communications* 40 (Mar. 2012), pp. 69–76. ISSN: 0093-6413. DOI: 10.1016/j.mechrescom.2012.01.013. URL: https://www.sciencedirect.com/science/article/pii/S0093641312000158 (visited on 03/08/2024).

[49] Domenico Asprone et al. “Statistical finite element analysis of the buckling behavior of honeycomb structures”. In: *Composite Structures* 105 (Nov. 2013), pp. 240–255. ISSN: 0263-8223. DOI: 10.1016/j.compstruct.2013.05.014. URL: https://www.sciencedirect.com/science/article/pii/S0263822313002249 (visited on 03/08/2024).

[50] S. Sakata, F. Ashida, and K. Ohsumimoto. “Stochastic homogenization analysis of a porous material with the perturbation method considering a microscopic geometrical random variation”. In: *International Journal of Mechanical Sciences* 77 (Dec. 2013), pp. 145–154. DOI: 10.1016/j.ijmecsci.2013.10.001.

[51] Jumpol Paiboon et al. “Numerical analysis of effective elastic properties of geomaterials containing voids using 3D random fields and finite elements”. In: *International Journal of Solids and Structures* 50.20 (Oct. 2013), pp. 3233–3241. ISSN: 0020-7683. DOI: 10.1016/j.ijsolstr.2013.05.031. URL: https://www.sciencedirect.com/science/article/pii/S0020768313002448 (visited on 03/08/2024).

[52] Finn E. Donaldson, James C. Coburn, and Karen Lohmann Siegel. “Total hip arthroplasty head–neck contact mechanics: A stochastic investigation of key parameters”. In: *Journal of Biomechanics* 47.7 (May 2014), pp. 1634–1641. ISSN: 0021-9290. DOI: 10.1016/j.jbiomech.2014.02.035. URL: https://www.sciencedirect.com/science/article/pii/S0021929014001493 (visited on 03/08/2024).

[53] Κωνσταντίνος Μπαχαρούδης. “Stochastic analysis of structures made of composite materials”. en. In: (July 2014). URL: http://hdl.handle.net/10889/8132 (visited on 03/11/2024).

[54] M.J. Bogdanor, C. Oskay, and S.B. Clay. “Multiscale modeling of failure in composites under model parameter uncertainty”. English. In: *Computational Mechanics* 56.3 (2015), pp. 389–404. ISSN: 0178-7675. DOI: 10.1007/s00466-015-1177-7.

[55] E. I. Saavedra Flores et al. “A computational multi-scale approach for the stochastic mechanical response of foam-filled honeycomb cores”. In: *Composite Structures* 94.5 (Apr. 2012), pp. 1861–1870. ISSN: 0263-8223. DOI: 10.1016/j.compstruct.2011.11.001. URL: https://www.sciencedirect.com/science/article/pii/S0263822311004090 (visited on 03/08/2024).

[56] Shen Shang and Gun Jin Yun. “Stochastic finite element with material uncertainties: Implementation in a general purpose simulation program”. In: *Finite Elements in Analysis and Design* 64 (Feb. 2013), pp. 65–78. ISSN: 0168-874X. DOI: 10.1016/j.finel.2012.10.001. URL: https://www.sciencedirect.com/science/article/pii/S0168874X12001837 (visited on 03/08/2024).

[57] J. Grasa et al. “The perturbation method and the extended finite element method. An application to fracture mechanics problems”. en. In: *Fatigue & Fracture of Engineering Materials & Structures* 29.8 (2006). _eprint: https://onlinelibrary.wiley.com/doi/pdf/10.1111/j.1460-2695.2006.01028.x, pp. 581–587. ISSN: 1460-2695. DOI: 10.1111/j.1460-2695.2006.01028.x. URL: https://onlinelibrary.wiley.com/doi/abs/10.1111/j.1460-2695.2006.01028.x (visited on 03/07/2024).

[58] L. F. Tenn. “Statistical Analysis of Fibrous Composite Strength Data”. en. In: (Jan. 1981). DOI: 10.1520/STP29313S. URL: https://asmedigitalcollection.asme.org/astm-ebooks/book/1369/chapter/27798617/Statistical-Analysis-of-Fibrous-Composite-Strength (visited on 04/15/2024).

[59] Srinivas Sriramula and Marios Chryssanthopoulos. “Probabilistic Models for Spatially Varying Mechanical Properties of In-Service GFRP Cladding Panels”. In: *Journal of Composites for Construction - J COMPOS CONSTR* 13 (Apr. 2009). DOI: 10.1061/(ASCE)1090-0268(2009)13:2(159).

[60] N. Manoj. “First Order Reliability Method: Concepts and Application”. In: 2016. URL: https://www.semanticscholar.org/paper/First-Order-Reliability-Method%3A-Concepts-and-Manoj/9e733a66258a41dcd34e1751be66308ec4e4610d (visited on 03/29/2024).

[61] D. Mohammed and S. Al-Zaidee. “Deflection Reliability Analysis for Composite Steel Bridges”. In: *Engineering, Technology & Applied Science Research* 12.5 (Oct. 2022), pp. 9155–9159. ISSN: 1792-8036, 2241-4487. DOI: 10.48084/etasr.5146. URL: http://www.etasr.com/index.php/ETASR/article/view/5146 (visited on 03/06/2024).

[62] Marcin Kamiński and Michał Strąkowski. “An Application of Relative Entropy in Structural Safety Analysis of Elastoplastic Beam under Fire Conditions”. In: *Energies* 16 (Dec. 2022), p. 207. DOI: 10.3390/en16010207.

[63] Roger G. Ghanem and Pol D. Spanos. *Stochastic Finite Elements: A Spectral Approach*. en. New York, NY: Springer, 1991. ISBN: 978-1-4612-7795-8. DOI: 10.1007/978-1-4612-3094-6. URL: http://link.springer.com/10.1007/978-1-4612-3094-6 (visited on 03/18/2024).

[64] Nian-Zhong Chen and C. Guedes Soares. “Spectral stochastic finite element analysis for laminated composite plates”. In: *Computer Methods in Applied Mechanics and Engineering* 197.51 (Oct. 2008), pp. 4830–4839. ISSN: 0045-7825. DOI: 10.1016/j.cma.2008.07.003. URL: https://www.sciencedirect.com/science/article/pii/S0045782508002557 (visited on 03/13/2024).

[65] M.S.M. Noori and R.M. Abbas. “Reliability Analysis of an Uncertain Single Degree of Freedom System Under Random Excitation”. English. In: *Engineering, Technology and Applied Science Research* 12.5 (2022), pp. 9252–9257. ISSN: 2241-4487. DOI: 10.48084/etasr.5193.

[66] P. A. M. Lopes, H. M. Gomes, and A. M. Awruch. “Reliability analysis of laminated composite structures using finite elements and neural networks”. In: *Composite Structures* 92.7 (June 2010), pp. 1603–1613. ISSN: 0263-8223. DOI: 10.1016/j.compstruct.2009.11.023. URL: https://www.sciencedirect.com/science/article/pii/S0263822309004929 (visited on 03/07/2024).

[67] Anders Olsson, Göran Sandberg, and O. Dahlblom. “On Latin Hypercube Sampling for structural reliability analysis”. In: *Structural Safety* 25 (Jan. 2003), pp. 47–68. DOI: 10.1016/S0167-4730(02)00039-5.

[68] F. Zhang et al. “Quantitative structural uncertainty analysis of composite honeycomb sandwich using a feedback neural network”. English. In: *Physica D: Nonlinear Phenomena* 458 (2024). ISSN: 0167-2789. DOI: 10.1016/j.physd.2023.133985.

[69] Robin Preece and Jovica Milanović. “Efficient Estimation of the Probability of Small-Disturbance Instability of Large Uncertain Power Systems”. In: *IEEE Transactions on Power Systems* 31 (Apr. 2015), pp. 1–10. DOI: 10.1109/TPWRS.2015.2417204.

[70] Robert C. Wetherhold. “Reliability Calculations for Strength of a Fibrous Composite Under Multiaxial Loading”. en. In: *Journal of Composite Materials* 15.3 (May 1981). Publisher: SAGE Publications Ltd STM, pp. 240–248. ISSN: 0021-9983. DOI: 10.1177/002199838101500304. URL: https://doi.org/10.1177/002199838101500304 (visited on 04/01/2024).

[71] T. P. Philippidis and D. J. Lekou. “A Probabilistic Approach to Failure Prediction of Frp Laminated Composites”. In: *Mechanics of Composite Materials and Structures* 5.4 (Jan. 1999). Publisher: Taylor & Francis _eprint: https://www.tandfonline.com/doi/pdf/10.1080/10759419808945907, pp. 371–382. ISSN: 1075-9417. DOI: 10.1080/10759419808945907. URL: https://www.tandfonline.com/doi/abs/10.1080/10759419808945907 (visited on 04/01/2024).

[72] Z.-K. Wang et al. “Research on seismic response of asphalt concrete core dam-overburden considering the spatial variability of material parameters”. Chinese. In: *Zhendong Gongcheng Xuebao/Journal of Vibration Engineering* 35.5 (2022), pp. 1188–1199. ISSN: 1004-4523. DOI: 10.16385/j.cnki.issn.1004-4523.2022.05.017.

[73] M. Kleiber and T.D. Hien. “The stochastic finite element method (basic perturbation technique and computer implementation)”. en. In: *Applied Stochastic Models and Data Analysis* 10.4 (1994). _eprint: https://onlinelibrary.wiley.com/doi/pdf/10.1002/asm.3150100412, pp. 297–297. ISSN: 1099-0747. DOI: 10.1002/asm.3150100412. URL: https://onlinelibrary.wiley.com/doi/abs/10.1002/asm.3150100412 (visited on 04/02/2024).

[74] Wing Kam Liu, Ted Belytschko, and A. Mani. “Probabilistic finite elements for nonlinear structural dynamics”. In: *Computer Methods in Applied Mechanics and Engineering* 56.1 (May 1986), pp. 61–81. ISSN: 0045-7825. DOI: 10.1016/0045-7825(86)90136-2. URL: https://www.sciencedirect.com/science/article/pii/0045782586901362 (visited on 04/02/2024).

[75] S. Rahman and B. N. Rao. “A perturbation method for stochastic meshless analysis in elastostatics”. en. In: *International Journal for Numerical Methods in Engineering* 50.8 (2001). _eprint: https://onlinelibrary.wiley.com/doi/pdf/10.1002/nme.106, pp. 1969–1991. ISSN: 1097-0207. DOI: 10.1002/nme.106. URL: https://onlinelibrary.wiley.com/doi/abs/10.1002/nme.106 (visited on 03/07/2024).

[76] Cho Wing To. “Finite Element Methods for Structures with Large Stochastic Variations by I. Elishakoff and Y.J. Ren”. In: *Journal of Sound and Vibration* 270 (Mar. 2004), pp. 1092–1094. DOI: 10.1016/j.jsv.2003.12.004.

[77] Marcin Kamiński. “Uncertainty analysis in solid mechanics with uniform and triangular distributions using stochastic perturbation-based Finite Element Method”. In: *Finite Elements in Analysis and Design* 200 (Mar. 2022), p. 103648. ISSN: 0168-874X. DOI: 10.1016/j.finel.2021.103648. URL: https://www.sciencedirect.com/science/article/pii/S0168874X2100130X (visited on 04/02/2024).

[78] Roger Ghanem. “Stochastic Finite Element Expansion for Random Media”. In: *Journal of Engineering Mechanics-asce - J ENG MECH-ASCE* 115 (May 1989). DOI: 10.1061/(ASCE)0733-9399(1989)115:5(1035).

[79] M. F. Ngah and A. Young. “Application of the spectral stochastic finite element method for performance prediction of composite structures”. In: *Composite Structures* 78.3 (May 2007), pp. 447–456. ISSN: 0263-8223. DOI: 10.1016/j.compstruct.2005.11.009. URL: https://www.sciencedirect.com/science/article/pii/S0263822305003259 (visited on 03/13/2024).

[80] K. Sepahvand. “Spectral stochastic finite element vibration analysis of fiber-reinforced composites with random fiber orientation”. In: *Composite Structures* 145 (June 2016), pp. 119–128. ISSN: 0263-8223. DOI: 10.1016/j.compstruct.2016.02.069. URL: https://www.sciencedirect.com/science/article/pii/S0263822316301106 (visited on 03/12/2024).

[81] Kian K. Sepahvand and Steffen Marburg. “Spectral stochastic finite element method in vibroacoustic analysis of fiber-reinforced composites”. In: *Procedia Engineering* 199 (Dec. 2017), pp. 1134–1139. DOI: 10.1016/j.proeng.2017.09.241.

[82] Mona M. Dannert et al. “Investigations on the restrictions of stochastic collocation methods for high dimensional and nonlinear engineering applications”. In: *Probabilistic Engineering Mechanics* 69 (July 2022), p. 103299. ISSN: 0266-8920. DOI: 10.1016/j.probengmech.2022.103299. URL: https://www.sciencedirect.com/science/article/pii/S0266892022000613 (visited on 03/12/2024).

[83] Z. Y. Liu and C. Y. Dong. “Automatic coupling of ABAQUS and a boundary element code for dynamic elastoplastic problems”. In: *Engineering Analysis with Boundary Elements* 65 (Apr. 2016), pp. 147–158. ISSN: 0955-7997. DOI: 10.1016/j.enganabound.2015.12.021. URL: https://www.sciencedirect.com/science/article/pii/S0955799716300029 (visited on 03/12/2024).

[84] F. Zhang, Q. Zhou, and P. Du. “Seismic Response Analysis of Cut-Off Wall of Dam Foundation Under Spatial Variability of Parameters”. Chinese. In: *Shanghai Jiaotong Daxue Xuebao/Journal of Shanghai Jiaotong University* 56.5 (2022), pp. 684–692. ISSN: 1006-2467. DOI: 10.16183/j.cnki.jsjtu.2021.242.

[85] Wolfgang Betz, Iason Papaioannou, and Daniel Straub. “Numerical methods for the discretization of random fields by means of the Karhunen-Loève expansion”. In: *Computer Methods in Applied Mechanics and Engineering* 271 (Apr. 2014). DOI: 10.1016/j.cma.2013.12.010.

[86] Ammar Basmaji et al. “Karhunen-Loève expansion based on an analytical solution over a bounding box domain”. In: *Probabilistic Engineering Mechanics* 74 (Aug. 2023), p. 103519. DOI: 10.1016/j.probengmech.2023.103519.

[87] Bruno Sudret and Armen Der Kiureghian. “Stochastic Finite Element Methods and Reliability A State-of-the-Art Report”. In: (Jan. 2000).

[88] Chun-Ching Li and A. Der Kiureghian. “Optimal Discretization of Random Fields”. EN. In: *Journal of Engineering Mechanics* 119.6 (June 1993). Publisher: American Society of Civil Engineers, pp. 1136–1154. ISSN: 0733-9399. DOI: 10.1061/(ASCE)0733-9399(1993)119:6(1136). URL: https://ascelibrary.org/doi/10.1061/%28ASCE%290733-9399%281993%29119%3A6%281136%29 (visited on 04/16/2024).

[89] Shuvajit Mukherjee et al. “Static and dynamic analysis of sandwich panel with spatially varying non-Gaussian properties”. In: *Journal of Sandwich Structures & Materials* 22 (Sept. 2018), p. 109963621879397. DOI: 10.1177/1099636218793979.

[90] Folco Casadei, Martin Larcher, and George Valsamos. *Implementation of Linear Lagrange 2D and 3D Continuum Elements for Solids in EUROPLEXUS*. Jan. 2015. DOI: 10.2788/180569.

[91] Diego Lorenzo Allaix and Vincenzo Ilario Carbone. “Discretization of 2D random fields: A genetic algorithm approach”. In: *Engineering Structures* 31.5 (May 2009), pp. 1111–1119. ISSN: 0141-0296. DOI: 10.1016/j.engstruct.2009.01.008. URL: https://www.sciencedirect.com/science/article/pii/S014102960900011X (visited on 03/19/2024).

[92] Klaas Faber. “Short Communication: On solving generalized eigenvalue problems using Matlab”. en. In: *Journal of Chemometrics* 11.1 (1997), pp. 87–91. ISSN: 1099-128X. DOI: 10.1002/(SICI)1099-128X(199701)11:1<87::AID-CEM437>3.0.CO;2-H. (Visited on 05/23/2024).

[93] S. Park et al. “Modelling non-Gaussian uncertainties and the Karhunen–Loéve expansion within the context of polynomial chaos”. In: *Annals of Nuclear Energy* 76 (Feb. 2015), pp. 146–165. ISSN: 0306-4549. DOI: 10.1016/j.anucene.2014.09.047. URL: https://www.sciencedirect.com/science/article/pii/S030645491400526X (visited on 03/18/2024).

[94] ST Pinho et al. “Material and structural response of polymer-matrix fibre-reinforced composites”. en. In: *Journal of Composite Materials* 46.19-20 (Sept. 2012). Publisher: SAGE Publications Ltd STM, pp. 2313–2341. ISSN: 0021-9983. DOI: 10.1177/0021998312454478. URL: https://doi.org/10.1177/0021998312454478 (visited on 08/22/2024).

[95] Ireneusz Lapczyk and Juan Hurtado. “Progressive damage modeling in fiber-reinforced materials”. In: *Composites Part A: Applied Science and Manufacturing* 38 (Nov. 2007), pp. 2333–2341. DOI: 10.1016/j.compositesa.2007.01.017.

[96] B.R. van Dongen. “Progressive damage modelling of FRPs using a blended stress-strain and fracture mechanics approach in FEM”. Available at https://example.com/thesis.pdf. Master’s thesis. Example City, CA: University of Example, June 2017.

[97] Carlos Dávila, Pedro Camanho, and Cheryl Rose. “Failure Criteria for FRP Laminates”. In: *Journal of Composite Materials* 39 (Feb. 2005). DOI: 10.1177/0021998305046452.

[98] Ireneusz Lapczyk and Juan Hurtado. “Progressive damage modeling in fiber-reinforced materials”. In: *Composites Part A: Applied Science and Manufacturing* 38 (Nov. 2007), pp. 2333–2341. DOI: 10.1016/j.compositesa.2007.01.017.

[99] Zdenek Bazant and Byung Oh. “Crack Band Theory for Fracture of Concrete”. In: *Matériaux et Constructions* 16 (May 1983), pp. 155–177. DOI: 10.1007/BF02486267.

[100] Pedro P. Camanho et al. “Prediction of in situ strengths and matrix cracking in composites under transverse tension and in-plane shear”. In: *Composites Part A: Applied Science and Manufacturing* 37.2 (2006). CompTest 2004, pp. 165–176. ISSN: 1359-835X. DOI: https://doi.org/10.1016/j.compositesa.2005.04.023. URL: https://www.sciencedirect.com/science/article/pii/S1359835X05002526.

[101] Xiaodong Wang et al. “An accurate and easy to implement method for predicting matrix crack and plasticity of composites with an efficient search algorithm for LaRC05 criterion”. In: *Composites Part A: Applied Science and Manufacturing* 131 (Feb. 2020), p. 105808. DOI: 10.1016/j.compositesa.2020.105808.

[102] B.G. Green, M.R. Wisnom, and Stephen Hallett. “An experimental investigation into the tensile strength scaling of notched composites”. In: *Composites Part A: Applied Science and Manufacturing* 38 (Mar. 2007), pp. 867–878. DOI: 10.1016/j.compositesa.2006.07.008.

[103] Thomas Bru et al. “Characterisation of the mechanical and fracture properties of a uni-weave carbon fibre/epoxy non-crimp fabric composite”. In: *Data in Brief* 6 (Mar. 2016), pp. 680–695. ISSN: 2352-3409. DOI: 10.1016/j.dib.2016.01.010. URL: https://www.sciencedirect.com/science/article/pii/S2352340916000160 (visited on 09/05/2024).

[104] J. Kupski et al. “Composite layup effect on the failure mechanism of single lap bonded joints”. In: *Composite Structures* 217 (June 2019), pp. 14–26. ISSN: 0263-8223. DOI: 10.1016/j.compstruct.2019.02.093. URL: https://www.sciencedirect.com/science/article/pii/S0263822318347160 (visited on 09/05/2024).

[105] Elias Tzavalis and Leonidas Rompolis. “Recovering Risk Neutral Densities from Option Prices: A New Approach”. In: *Journal of Financial and Quantitative Analysis* 43 (Dec. 2008), pp. 1037–1053. DOI: 10.1017/S0022109000014435.

[106] T.-L. Zhu. “A reliability-based safety factor for aircraft composite structures”. In: *Computers & Structures* 48.4 (1993), pp. 745–748. ISSN: 0045-7949. DOI: https://doi.org/10.1016/0045-7949(93)90269-J. URL: https://www.sciencedirect.com/science/article/pii/004579499390269J.

[107] Stephen Hallett et al. “Damage development in open hole composite specimens in fatigue. Part 1: Experimental Investigation”. In: *Composite Structures* 106 (Dec. 2013), pp. 890–898. DOI: 10.1016/j.compstruct.2013.05.033.

[108] O. Nixon-Pearson and Stephen Hallett. “An investigation into the damage development and residual strengths of open-hole specimens in fatigue”. In: *Composites Part A: Applied Science and Manufacturing* 69 (Feb. 2015). DOI: 10.1016/j.compositesa.2014.11.013.

[109] O. Nixon-Pearson and Stephen Hallett. “An investigation into the damage development and residual strengths of open-hole specimens in fatigue”. In: *Composites Part A: Applied Science and Manufacturing* 69 (Feb. 2015). DOI: 10.1016/j.compositesa.2014.11.013.

[110] Amin Farrokhabadi, Hossein Hosseini-Toudeshky, and Bijan Mohammadi. “Development of a Damage Analysis Method in Laminated Composites Using Finite Fracture Toughness of Single Lamina”. In: *Mechanics of Advanced Materials and Structures - MECH ADV MATER STRUCT* 20 (Jan. 2012). DOI: 10.1080/15376494.2011.584144.

[111] Z. Hashin. “Failure Criteria for Unidirectional Fiber Composites”. In: *Journal of Applied Mechanics* 47.2 (June 1980), pp. 329–334. ISSN: 0021-8936. DOI: 10.1115/1.3153664. URL: https://doi.org/10.1115/1.3153664 (visited on 09/24/2024).

# A

# Constitutive Models

The most widely used 3D constitutive model for composite laminates is presented below, where a single ply (unidirectional or fabric) is modelled as an orthotropic material (two planes of symmetry) [6].

$$\begin{bmatrix} \epsilon_1 \\ \epsilon_2 \\ \epsilon_3 \\ \gamma_{23} \\ \gamma_{13} \\ \gamma_{12} \end{bmatrix} = \begin{bmatrix} \frac{1}{E_1} & \frac{-\nu_{21}}{E_2} & \frac{-\nu_{31}}{E_3} & & & \\ \frac{-\nu 12}{E_1} & \frac{1}{E_2} & \frac{-\nu_{32}}{E_3} & & & \\ \frac{-\nu_{13}}{E_1} & \frac{-\nu_{23}}{E_2} & \frac{1}{E_3} & & & \\ & & & \frac{1}{G_{23}} & & \\ & & & & \frac{1}{G_{13}} & \\ & & & & & \frac{1}{G_{12}} \end{bmatrix} \begin{bmatrix} \sigma_1 \\ \sigma_2 \\ \sigma_3 \\ \tau_{23} \\ \tau_{13} \\ \tau_{12} \end{bmatrix} \tag{A.1}$$

The model is better understood with the diagram presented in figure A.1, where direction 1 is always aligned with the fiber reinforcement direction, since this is the local reference system.

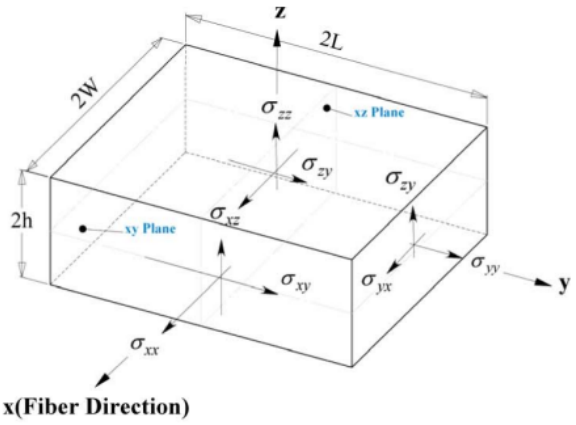


**Figure A.1:** Stresses on orthotropic lamina, adapted from [110].

The model has 9 independent material properties: Young's Modulus in 3 directions ($E_1$, $E_2$, $E_3$), Shear Modulus ($G_{23}$, $G_{13}$, $G_{12}$) and Poisson's ratios ($\nu_{12}$, $\nu_{13}$, $\nu_{23}$). These are often reduced to five under transversely isotropic assumptions (properties are the same in y and z directions). Under those assumptions, $E_3 = E_2$, $\nu_{13} = \nu_{12}$, $G_{13} = G_{12}$ and $G_{23} = E_3/(2(1 + \nu_{23}))$.

For structures where out-of-plane stresses are not significant, usually for thin plates, where one dimension is much smaller than the others, the model is commonly reduced to

$$\begin{bmatrix} \epsilon_1 \\ \epsilon_2 \\ \gamma_{12} \end{bmatrix} = \begin{bmatrix} \frac{1}{E_1} & \frac{-\nu_{21}}{E_2} & \\ \frac{1}{E_1} & \frac{-\nu_{21}}{E_2} & \\ & & \frac{1}{G_{12}} \end{bmatrix} \begin{bmatrix} \sigma_1 \\ \sigma_2 \\ \tau_{12} \end{bmatrix}. \tag{A.2}$$

This simplified model is significantly less computationally expensive, and therefore is frequently used, for example in CLT.

# B

# Failure criteria

## B.1. Larc05

The Fiber Kinking and Splitting failure index is presented below [94], while other failure modes are addressed in section 4.1.

**Fiber Kinking and Splitting**

The same expression is used for both compressive failure modes, with the distinction coming from the magnitude of $\sigma_1$:

$$FI_{Split} = FI_{Kink} = (\frac{\tau_{23}^m}{S_{23} - \eta^T \sigma_2^m})^2 + (\frac{\tau_{12}^m}{S_{12} - \eta^L \sigma_2^m})^2 + (\frac{\langle \sigma_2^m \rangle^+}{Y_T})^2, \tag{B.1}$$

indicating fibre kinking for $\sigma_1 \leq -X_C/2$ and fibre splitting for $\sigma_1 > X_C/2$. Similarly to the matrix criterion, the stresses in the expression $\tau_{23}^m$, $\tau_{12}^m$ and $\langle \sigma_2^m \rangle^+$ refer to the transverse shear, in-plane shear and transverse in-plane normal stresses in the misalignment frame. This frame is always found in the kink band plane, as is illustrated in figure B.1.

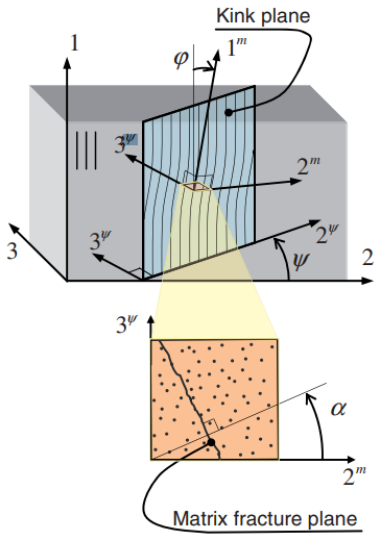


**Figure B.1:** Physical model for kink-band formation [94].

The stresses in the kink plane are given by

$$\sigma_2^{\Psi} = \cos(\Psi)^2\sigma_2 + \sin(\Psi)^2\sigma_3 + 2\sin(\Psi)\cos(\Psi)\tau_{23}, \tag{B.2}$$

$$\tau_{12}^{\Psi} = \tau_{12}\cos(\psi) + \tau_{31}\sin(\Psi), \tag{B.3}$$

$$\tau_{31}^{\Psi} = \tau_{31}\cos(\psi) - \tau_{12}\sin(\Psi) \tag{B.4}$$

and

$$\tau_{23}^{\Psi} = \sin(\psi)\cos(\psi)(\sigma_3 - \sigma_2) + (\cos(\psi)^2) - \sin(\psi^2))\tau_{23}. \tag{B.5}$$

The stresses in the misalignment frame are given by

$$\sigma_2^m = \sin(\varphi)^2\sigma_1 + \cos(\varphi)^2\sigma_2^{\Psi} - 2\sin(\varphi)\cos(\varphi)\tau_{12}^{\Psi}, \tag{B.6}$$

$$\tau_{12}^m = -\sin(\varphi)\cos(\varphi)\sigma_1 + \sin(\varphi)\cos(\varphi)\sigma_2^{\Psi} + (\cos(\varphi)^2 - \sin(\varphi)^2)\tau_{12}^{\Psi} \tag{B.7}$$

and

$$\tau_{23}^m = \tau_{23}^{\Psi}\cos(\varphi) - \tau_{31}^{\Psi}\sin(\varphi). \tag{B.8}$$

The kink plane rotation angle $\Psi$ is the one that maximizes the failure index. The misalignment angle $\varphi$ is calculated with

$$\varphi = sgn(\tau_{12}^{\Psi})\varphi_0 + \gamma_{m^0}, \tag{B.9}$$

where $\gamma_{m^0}$ is the shear strain given by

$$\gamma_{m^0} = \tau_0^m / G_{12}. \tag{B.10}$$

In the above expression, $\tau_0^m$ is the shear stress calculated with equation B.7 and the initial misalignment angle $\varphi_0$. The initial misalignment angle can be calculated with equation

$$\varphi_0 = \frac{\tau_{12} + (G_{12} - X_C)\varphi_C}{G_{12} + \sigma_1 - \sigma_2}, \tag{B.11}$$

where

$$\varphi_C = \arctan\left(\frac{1 - \sqrt{1 - 4(S_{12}/X_C + \eta_L)(S_{12}/X_C)}}{2(S_{12}X_C + \eta_L}\right). \tag{B.12}$$

## B.2. Hashin

The failure indices of the Hashin criteria are calculated as follows [111]:

**MFT**

$$FI_{MFT} = \frac{(\sigma_2 + \sigma_3)^2}{Y_T^2} + \frac{\tau_{12}^2 + \tau_{13}^2}{S_{12}^2} + \frac{\tau_{23}^2 - \sigma_2\sigma_3}{S_{23}^2} \tag{B.13}$$

**MFC**

$$FI_{MFC} = \frac{1}{Y_C}[(\frac{Y_C}{2S_{23}})^2 - 1](\sigma_2 + \sigma_3) + \frac{1}{4S_{23}^2}(\sigma_2 + \sigma_3)^2 + \frac{1}{S_{23}^2}(\tau_{23}^2 - \sigma_2\sigma_3) + \frac{1}{S_{12}^2}(\tau_{12}^2 + \tau_{13}^2) \quad \text{(B.14)}$$

**FFT**

$$FI_{FFT} = (\frac{\sigma_1}{X_T})^2 + \frac{1}{S_{12}^2}(\tau_{12}^2 + \tau_{13}^2) \quad \text{(B.15)}$$

**FFC**

$$FI_{FFC} = |\sigma_1| - X_C \quad \text{(B.16)}$$

# C

# UMAT subroutine

Figure C.1 shows an overview of the working steps of the UMAT subroutine. Note that viscous regularization is not applicable to models that apply the bilinear degradation MDM.

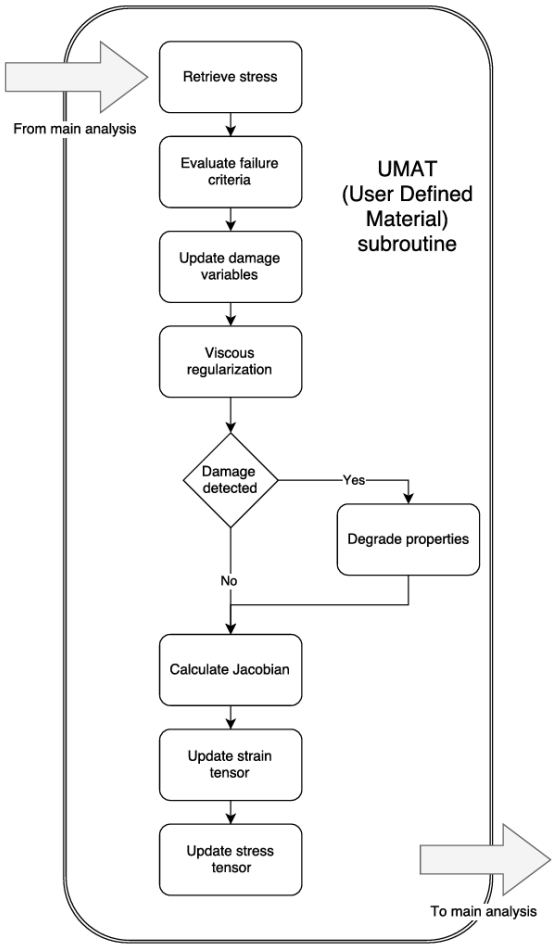


**Figure C.1:** UMAT overview [96]

# D

# Additional figures/tables from case studies

This appendix includes figures and tables that are referenced/explained but not presented in the main part of the report.

## D.1. Plate in uniaxial tension - Nastos et al.

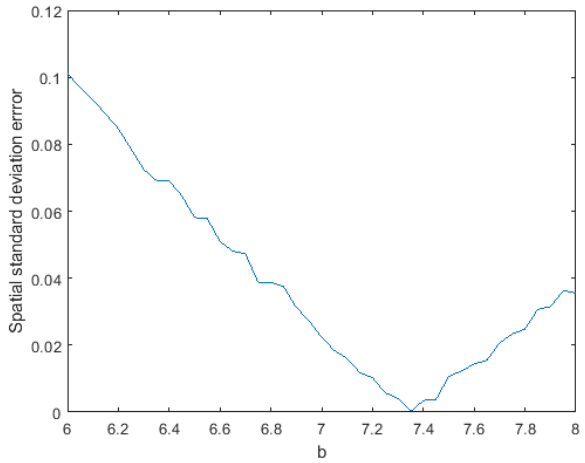


**Figure D.1:** Error parameter $\epsilon_{\sigma_s}$ for different values of $b_{cx} = b_{cy}$, with target value of 5GPa.

**Figure D.2:** FE model with boundary conditions.

**Table D.1:** Kolmogorv-Smirnov test results - Test=1 means the hypothesis that the dataset came from a given distribution is not rejected at that significance level.

| | Experimental set | | Model results | |
|---|---|---|---|---|
| | Test (5% significance) | p-level | Test (5% significance) | p-level |
| Normal | 1 | 0.94 | 1 | 0.99 |
| Lognormal | 1 | 0.93 | 1 | 0.92 |
| Weibull | 1 | 0.99 | 1 | 0.60 |
| Gamma | 1 | 0.99 | 1 | 0.96 |

## D.2. Open-hole tension - van Dongen et al.

**Table D.2:** Effect of mesh size on deterministic model predictions (384, 1691 and 4832 elements).

| | Predicted [kN] | Discrepancy to previous [%] |
|---|---|---|
| rough mesh | 24.57 | - |
| fine mesh | 27.25 | 10.9% |
| very fine mesh | 27.81 | 2.0% |

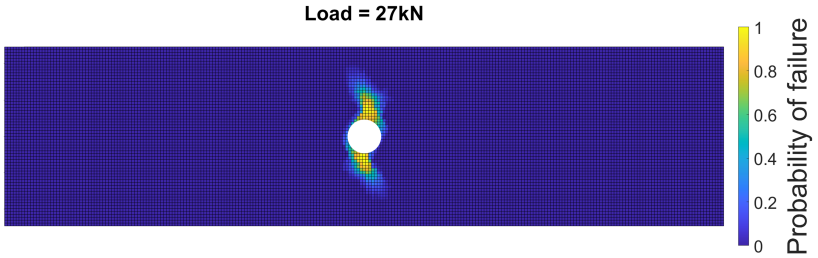


**Figure D.3:** Probability of MFT in a 45° ply with 27kN applied load, throughout the specimen.

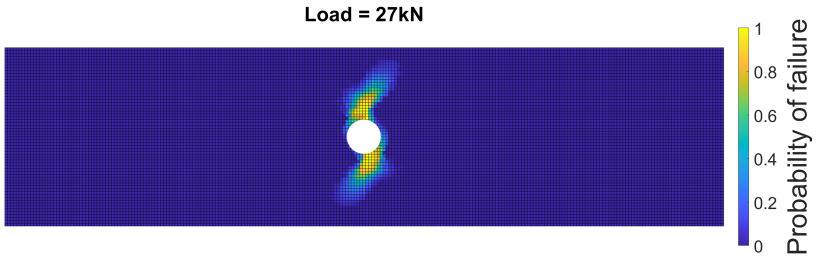


**Figure D.4:** Probability of MFT in a -45° ply with 27kN applied load, throughout the specimen.

# D.3. Open-hole tension - Nixon-Pearson et al.

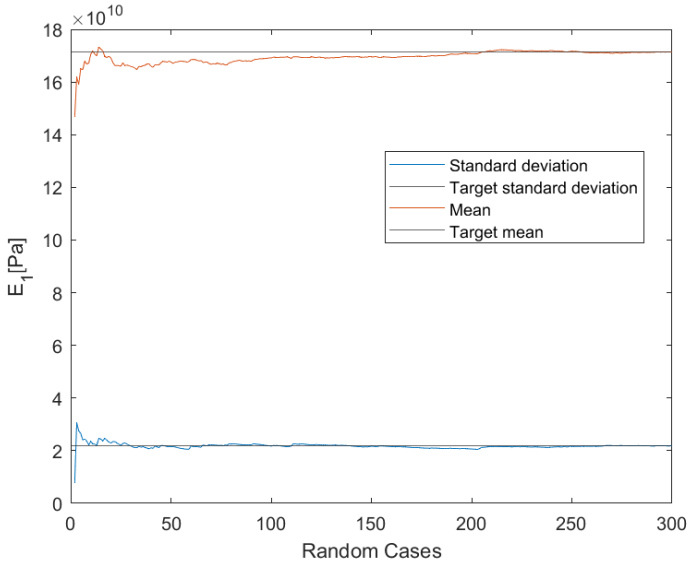


**Figure D.5:** Convergence of the $E_1$ mean [Pa] and standard deviation [Pa] at an arbitrary point with increase of $N_\theta$.

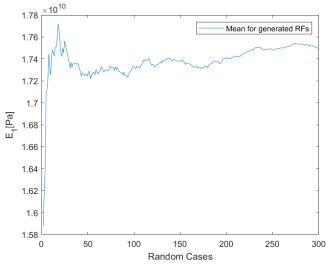


**(a)** b=0.0735,COV$_2$ - $\sigma_s \rightarrow$ 17.5GPa

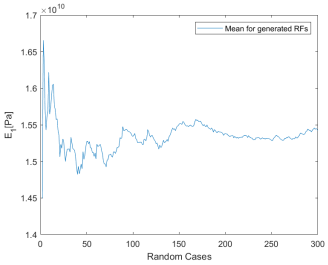


**(b)** b=0.735,COV$_2$ - $\sigma_s \rightarrow$ 15.4GPa

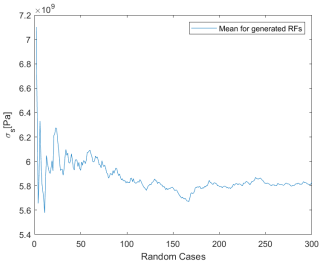


**(c)** b=7.35,COV$_2$ - $\sigma_s \rightarrow$ 5.8GPa

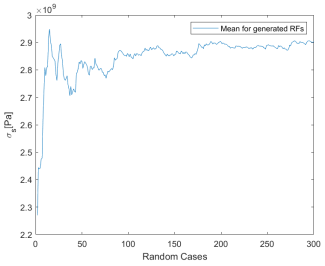


**(d)** b=7.35,COV$_1$ - $\sigma_s \rightarrow$ 2.9GPa

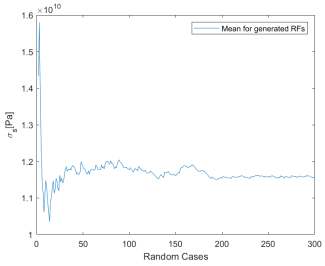


**(e)** b=7.35,COV$_3$ - $\sigma_s \rightarrow$ 11.5GPa

**Figure D.6:** Convergence of the $E_1$ $\sigma_s$ [Pa] with increase of $N_\theta$, with different correlation parameters and COVs.

**Table D.3:** Effect of mesh size on deterministic model predictions (648, 2878 and 4724 elements).

| | Predicted [kN] | Discrepancy to previous [%] |
|---|---|---|
| rough mesh | 16.53 | - |
| fine mesh | 20.475 | 19.2% |
| very fine mesh | 21.24 | 3.73% |

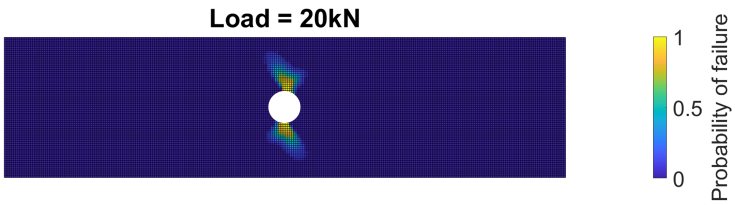


**Figure D.7:** Probability of MFT in a 45° ply with 20kN applied load, throughout the specimen.

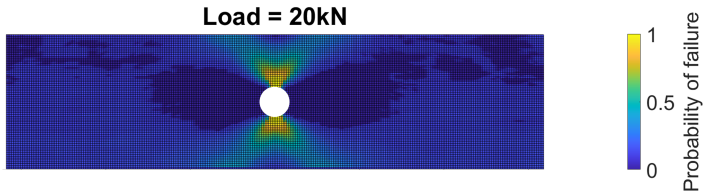


**Figure D.8:** Probability of MFT in a 90° ply with 20kN applied load, throughout the specimen.